Polymers in scale free spaces

Author:

Yosi Hammer

Supervisor:

Prof. Yacov Kantor

A thesis submitted to the senate of Tel Aviv University

in fulfilment of the requirements

for the degree of Doctor of Philosophy

in the

School of Physics and Astronomy

Raymond and Beverly Sackler Faculty of Exact Sciences

August 2016

This work was done under the supervision of Prof. Yacov Kantor

to Naomi,

"*His majesty's ministers, finding that Gulliver's stature exceeded theirs in the proportion of twelve to one, concluded from the similarity of their bodies that his must contain at least 1728 (or 12^3) of theirs, and must be rationed accordingly.*"

Gulliver's Travels, Jonathan Swift, 1726

Abstract

This Thesis studies long flexible polymers in the presence of scale-free (SF) repulsive surfaces. A SF surface is one that has no characteristic length scale (e.g., an infinite cone). When such self-similar boundaries are combined with long polymers, the system exhibit critical features that depend on the geometry of the surface, but are independent of the microscopic details of the molecule. This situation can be realized for example when a long molecule is anchored to an atomic force microscope with a conic tip [1].

In Chapter 2, we present analytical results for ideal polymers, where monomers are allowed to occupy the same volume in space (no steric repulsion). In experiments, ideal polymer statistics are observed in Θ-solvents, where the interaction with the solvent molecules cancels the repulsion between the monomers in the polymer. Using the analogy between an ideal polymer and a diffusing particle, we show that the problem of an ideal polymer anchored near a SF object can be mapped to an electrostatic problem, where a point charge is placed at the position where the polymer is anchored, near a conducting object of the same shape. This analogy explains some interesting results that were derived in the polymer system. For example, the pressure that the polymer exerts on the surface diverges near sharp corners (like the apex of a cone), similarly to the divergence of electric fields near corners of conductors.

While ideal polymers are susceptible to analytical treatment using the diffusion equation, polymers in good solvent (or self-avoiding polymers) are often studied numerically using self-avoiding walks (SAWs) on a lattice as a model. In Chapter 3, we show that when a local physical property like the pressure exerted on a boundary surface is studied in a lattice model, the results can be inconsistent with a continuous description of the system. We propose a correction to the common definition of entropic pressure in a lattice model so that it will be equal to the total force acting on the surface upon integration, and will be consistent with the definition of pressure in a continuous system. Interestingly, this corrected definition takes into account long range correlations between contact points of the polymer and the surface. In other words, on a lattice, the 'local' pressure is non-local.

In Chapter 4 we present simulation results for random walks (RWs) and SAWs on square and qubic lattices. We study the critical exponents in the presence of the surface, the end point-distribution and the average size of the walk. Using a recent implementation of the pivot algorithm [2], we were able to simulate polymers near surfaces of sizes that were not previously available in

simulations. For SAWs on the square lattice, we compare the results to theoretical predictions from conformal field theory and find some deviations from the theory. We discuss the details and possible reasons for this result.

The winding angle φ of a polymer around a point (in dimension $d = 2$) or a bar (in $d = 3$) is studied numerically in Chapter 5. We confirm theoretical results for RWs and SAWs in $d = 2$, and improve upon existing numerical studies of SAWs in $d = 3$. The ratio $\langle\varphi^4\rangle/\langle\varphi^2\rangle^2$ for a polymer winding around a bar exhibits non-monotonic behavior as a function of the number of steps in the walk. We discuss possible reasons for this surprising result. The behavior of the winding angle of SAWs in $d = 2$ can be explained using a simple scaling argument. We demonstrate that such an argument cannot be applied to SAWs in $d = 3$, most likely because in $d = 3$, the SAW can return to the vicinity of the excluded center around which the walk rotates, whereas in $d = 2$ the walk cannot return to the origin without intersecting with itself.

Acknowledgements

I am thankful to my advisor, Yacov Kantor, for his guidance and support. I have learned many things from Yacov. Along with his vast knowledge in various fields of physics, Yacov has a determination to get to the bottom of every problem we consider, and put together all the details in our disposal into a coherent physical image. Whenever I would come to Yacov to present results or discuss the right way to approach a problem, I would come out with a better understanding (sometimes opposite to the one I started with..) of the problem. His attention to details and careful approach was invaluable in the work we present in this Thesis.

I am also grateful to Mehran Kardar for reading the manuscripts of the work presented here prior to its publication and contributing valuable comments, and to Thomas A. Witten for useful discussions on the subject of the winding angle of long polymers.

I thank my family, and especially my parents, for their love, support and many schnitzels throughout my undergraduate and graduate studies. I follow their example in always learning new things and gaining new experiences.

Finally, I thank my wife, Anna Frishman, best friend and the love of my life, for her support, spirited discussions on statistical physics, and making me very happy.

Contents

List of Figures

List of Tables

Symbols and Abbreviations

AFM	atomic force microscope
RW	random walk
SAW	self-avoiding walk
SF	scale-free
IP	ideal polymer
R	root mean square end-to-end distance
$\mathcal{N}_N$	number of N-step walks on a lattice
ν, γ, η	critical exponents
Z	survival probability of a random walker (Chapter 2)
G	Green's function or propagator of a random walker (Chapter 2)
α	opening angle of a cone or wedge
φ	winding angle (Chapter 5)

Chapter 1

Introduction

1.1 Large molecules in confined spaces

In many experimental setups and biological systems, large polymers are confined by one or more macroscopic objects. For example, when polymers are attached to colloidal particles their steric interaction can be used to stabilize a solution (e.g., when producing paint [3]) and when polymers are end-grafted to an interface [4], they can modify its mechanical, chemical and electrical properties (e.g., to create anti-bacterial coating [5]).

In this Thesis, we focus on systems with long flexible homogeneous polymers near repulsive surfaces, where the entropy dominates the free energy of the system. The main role of the surface is to reduce the number of conformations for the polymer, and the force and pressure exerted by the polymer on the surface are called *entropic*.

In the last three decades, there has been great improvement in the field of single-molecule manipulation techniques [1, 6]. It is now possible to study in detail the mechanical properties of a single polymer in a specifically determined geometry. The main methods include atomic force microscopy (AFM) [7, 8], micro-needles [9, 10], magnetic [11] and optical [12] tweezers. In a typical experiment, the polymer is attached at one end to a planar substrate, and at the other end to a macroscopic object like an AFM tip or a spherical colloid (see Figure. 1.1). The object is used to stretch the polymer and measure force *vs.* distance curves. Sometimes, not only the total force exerted by the polymer on the surface is important, but also its distribution on the surface (i.e., the local pressure). This is the case when the polymer is attached to a flexible membrane that can change its shape as a result of the polymer's pressure [13, 14, 15].

In most cases, the purpose of single molecule experiments is to study the properties of a specific molecule like DNA [16, 17]. However, it was shown that when the polymer is large and the surface is repulsive and has no characteristic length scale, some properties of the system are independent

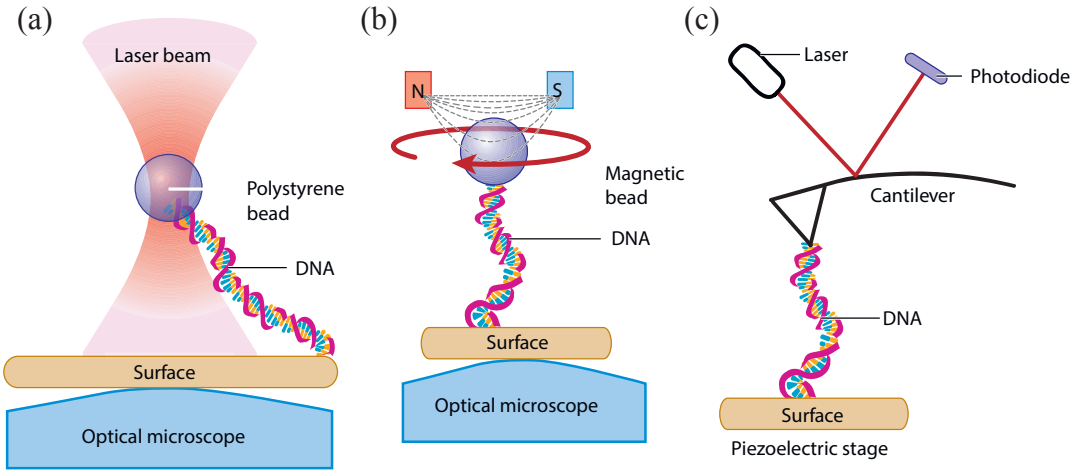

FIGURE 1.1: Illustrations of single molecule experiments (from [1]). (a) Optical tweezers. (b) Magnetic tweezers. (c) Atomic force microscope.

of microscopic details and depend only on a small number of parameters like the dimensionality of the system and the geometry of the surface [18, 19]. These properties are called *universal* and they can be used to calibrate devices or check fundamental features of a model for the polymer, that are independent of the details of the molecule. In this work, we focus on such universal features. Mainly, we study the entropic force, entropic pressure, monomer density and end-point distribution of long polymers near such surfaces.

1.2 Universality in polymer systems

Universality is a well known phenomena in statistical physics [20]. Usually a system displays universal features in the vicinity of a continuous phase transition, where the absence of a typical length-scale leads to power law behaviors and to the existence of critical exponents. The most common example is a magnetic system close to the paramagnetic-ferromagnetic transition. The susceptibility χ, diverges near the critical point as [21]

$$\chi \propto |T - T_C|^{-\gamma}, \tag{1.1}$$

where T is the temperature and T_C is the critical temperature. The correlation length, ξ, diverges as

$$\xi \propto |T - T_C|^{-\nu}. \tag{1.2}$$

The exponents γ and ν are called universal exponents, and are independent of microscopic details like the type of lattice involved, but depend on a small number of parameters such as the dimensionality of the system and of the individual spins. For our purpose it is convenient to use another critical exponent, η, which determines the decay of the spin correlation function near the critical point, i.e., when $\xi \to \infty$,

$$\langle \mathbf{s_0} \cdot \mathbf{s_r} \rangle \propto r^{-d+2-\eta}, \tag{1.3}$$

where d is the dimension of the system. The three exponents are related to each other by the Fisher scaling relation, [21]

$$\gamma = \nu(2 - \eta). \tag{1.4}$$

One of the great advancements in polymer physics was the realization that for a long polymer, there is a wide range of scales in which it also has no typical length scale [22] (see Figure 1.2). The polymer then has universal features that can be related to magnetic systems. Consider the $O(n)$ model, where n-component spins are placed on a lattice with short range interaction between them. The Hamiltonian

$$\mathcal{H} = -\sum_{\mathbf{r}} \mathbf{H} \cdot \mathbf{s_r} - J \sum_{\text{n.n}} \mathbf{s_r} \cdot \mathbf{s_{r'}}, \tag{1.5}$$

where $\mathbf{s_r}$ is the spin at the site $\mathbf{r}$, $\mathbf{H}$ is the magnetic field, J is the (positive) coupling parameter and n.n denotes a summation over nearest neighbor pairs. It was shown that in the limit $n \to 0$, the correlation between the spins $\mathbf{s_r}$ and $\mathbf{s_{r'}}$ is related to the number $\mathcal{N}_N(\mathbf{r}, \mathbf{r'})$, of self-avoiding walks (SAWs) on the lattice starting at $\mathbf{r}$ and ending at $\mathbf{r'}$ with N steps [22]. Specifically,

$$\langle \mathbf{s_r} \mathbf{s_{r'}} \rangle = \sum_N \mathcal{N}_N(\mathbf{r}, \mathbf{r'}) \left[\frac{J}{k_B T} \right]^N, \tag{1.6}$$

where k_B is the Boltzmann constant. In other words, the spin correlation function in the canonical ensemble is mapped to the partition function of SAWs in the *grand-canonical* ensemble, where N is not fixed but the fugacity $z = J/k_B T$ (note that T is the temperature in the *spin* system). The critical point is approached by taking $T \to T_C$, or alternatively, $z \to z_C$, where the mean number of steps in the walk, $\langle N \rangle \to \infty$.

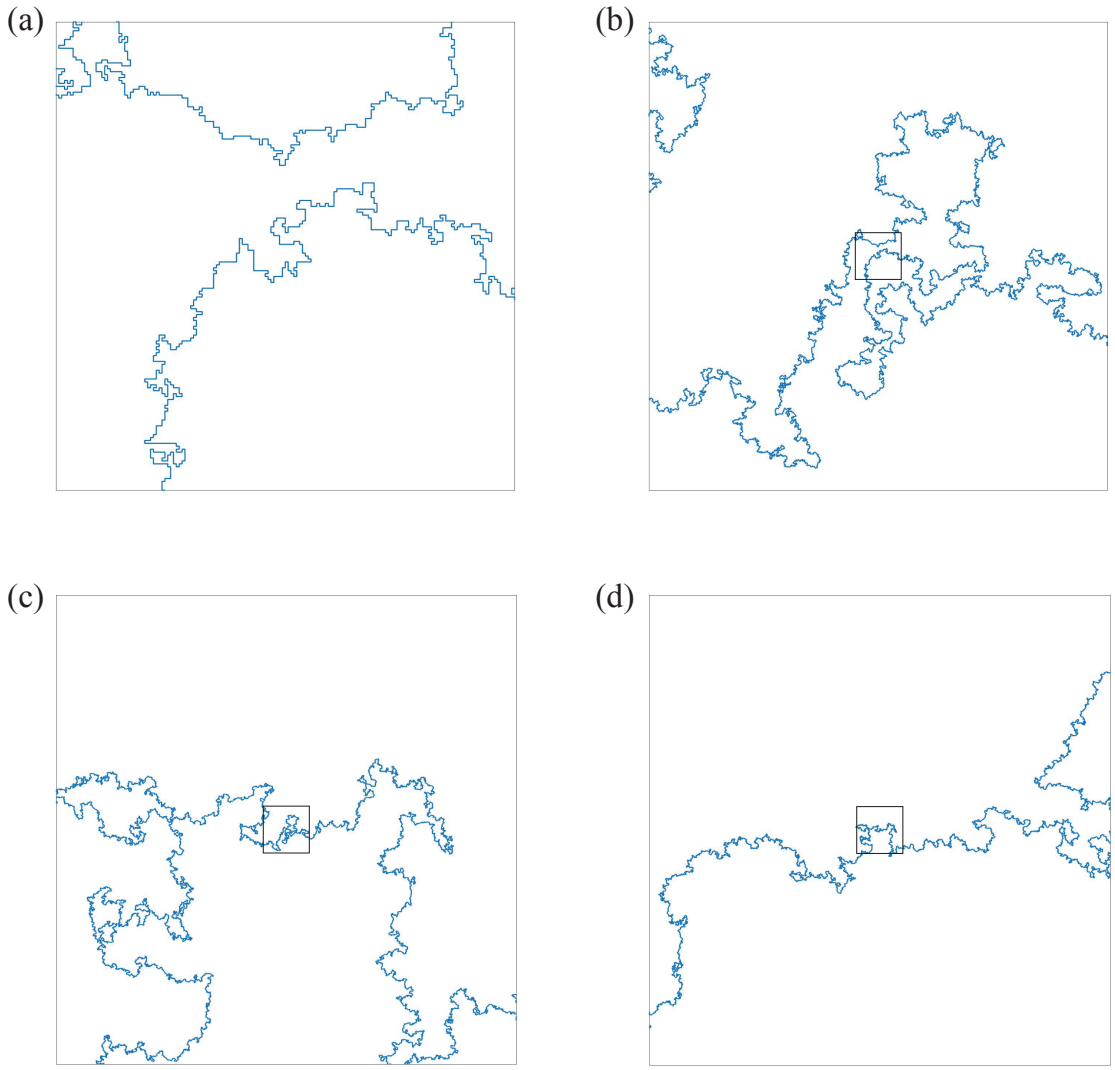

FIGURE 1.2: A SAW on a square lattice with 10^7 steps, shown in different magnifications. In (b), (c) and (d), the black square indicates the region plotted in higher magnification.

	RW	2d SAW	3d SAW
$\gamma_{\rm f}$	1	43/32	1.1575(6) [25]
$\nu_{\rm f}$	1/2	3/4	0.587597(7) [26]

TABLE 1.1: Values of the critical exponents for polymers in free space.

Since SAWs are used to model polymers in good solvent [22], from Eq. (1.6), the critical exponents defined in Eqs. (1.1) and (1.2) are given meaning in the polymer system as well. The total number of N-step walks on the lattice, $\mathcal{N}_N$, scales as

$$\mathcal{N}_N \propto \mu^N N^\gamma, \tag{1.7}$$

where μ is a non-universal effective coordination number of the lattice, and γ is the critical exponent, which is independent of the type of lattice for example. Similarly, the mean square end-to-end distance R^2 of the walk varies with the number of steps as

$$R^2 = a^2 N^{2\nu}, \tag{1.8}$$

where a is a microscopic length scale (monomer size or persistence length). These exponents have been studied analyticity and numerically for decades [23]. In this work we deal with two main universality classes for polymers: ideal polymers (IPs), where monomers are allowed to occupy the same volume in space, and polymers in good solvent, where steric interaction between the monomers is included. Note that up to logarithmic corrections to Eqs. (1.7) and (1.8), IP statistics are observed in experiments in Θ-solvents in $d = 3$, where the interaction with the solvent molecules cancels the repulsive interaction between monomers [24]. IPs can be modeled as random walks (RWs) on a lattice while polymers in good solvent are modeled as SAWs. The known analytical and best numerical values for the critical exponents γ and ν for polymers in free space (no boundaries) are given in Table 1.1.

The presence of boundaries can introduce new length scales. However, there is a group of surfaces, called *scale-free* (SF), such that the geometry has no characteristic length scale, i.e., they remain invariant under the coordinate transformation $\mathbf{r} \to \lambda\mathbf{r}$, as exemplified in Figure 1.3. When a long polymer is attached to a SF repulsive surface like an infinite cone or plane, the system retains its self-similar features since the surface and the polymer are both SF. Universal properties like critical exponents become dependent on the dimensionless features of the surface, such as the opening angle

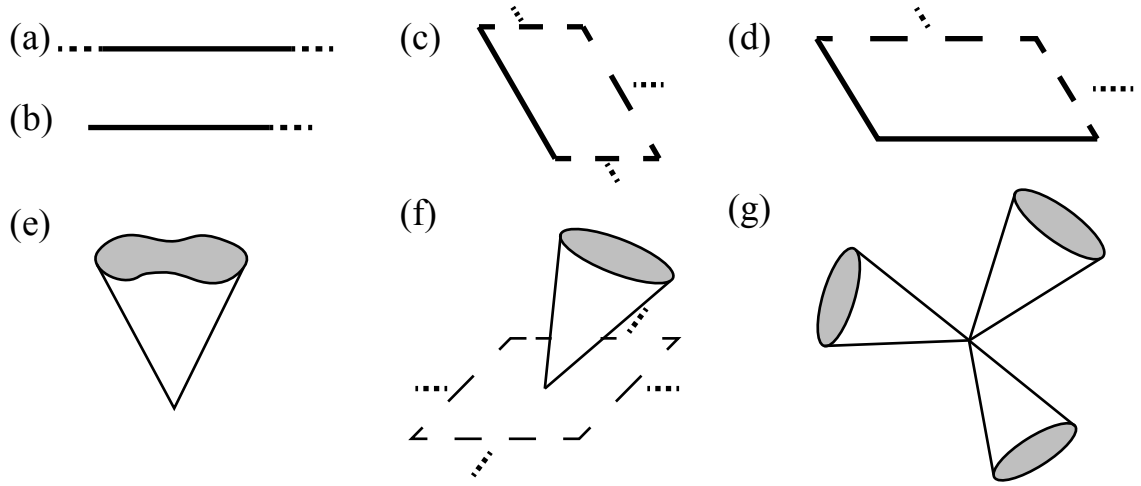

FIGURE 1.3: Scale-free surfaces. All surfaces extend to infinity as indicated by the dashed lines. Grey areas indicate truncation surfaces for graphical representation, while dashed lines represent similarly truncated surfaces. Dots indicate directions in which the infinite objects are extended. (a) Infinite, and (b) semi-infinite lines in $d = 2$ or 3. Semi-infinite (c) half-plane and (d) quarter-plane in $d = 3$. (e) Cone with convoluted cross section. Complex shapes created by (f) attaching apex of a cone to a plane, or (g) by joining apices of several cones.

of the cone [27]. In what follows, we study this geometry dependence of critical properties of long polymers near SF surfaces. Apart from the relevance to single molecule experiments, the goal is to improve our understanding of critical systems in various geometries.

1.3 Case in point – entropic force on a cone tip

Consider a setup in which a polymer is attached to the tip of an AFM designed in a conic shape (Figure 1.4). The cone is placed so that its tip is at a distance h from a planar substrate. The polymer exhibits self-similar properties at length scales greater than the persistence length a, and smaller than its end-to-end distance R. Thus, assuming that the AFM cone and the planar substrate are both greater than R, at separations $a \ll h \ll R$, the only relevant length scale in the system is h. For a long polymer ($R \to \infty$), the only relevant energy scale in the system is k_BT. Thus, on dimensional grounds, the force between the cone and the plane

$$F = \mathcal{A}\frac{k_BT}{h}. \tag{1.9}$$

It was shown in [18] that the dimensionless amplitude $\mathcal{A}$ can be related to the universal polymer exponents, that depend on the shape of the cone, i.e., on its opening angle, and if tilted, on the tilt

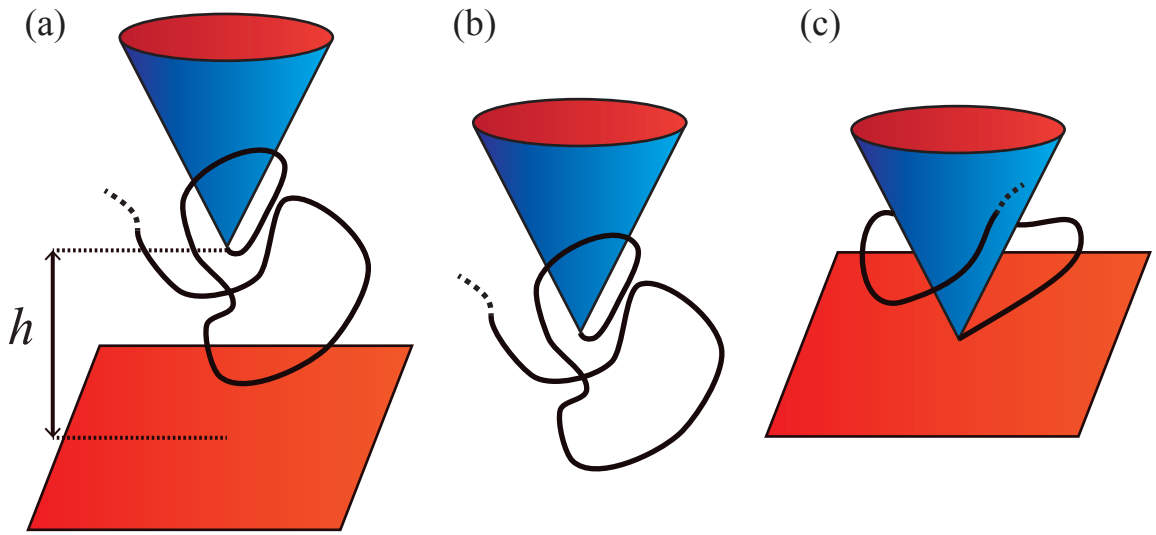

FIGURE 1.4: The setup considered in [18]. A polymer with persistence length a and end-to-end distance R is attached to a solid cone held at a separation h from a plane. Three cases are shown: (a) $a \ll h \ll R$, (b) $h \gg R$ and (c) $h = 0$.

angle. Let us briefly review their argument– consider the two limiting cases: (a) when $h \gg R$, the cone is far from the plane and the plane does not effect the conformations of the polymer [Figure 1.4(b)], and (b) when $h = 0$, the tip of the cone touches the plane [Figure 1.4(c)]. In both cases there is no characteristic length scale in the system and we expect to see universal behavior. The number of conformations available to the polymer, $\mathcal{N}$, will vary with the number of monomers N as in Eq. (1.7), with an exponent γ that will depend on the geometry of the boundary. Specifically, for the case $h \gg R$,

$$\mathcal{N}_{\text{cone}} = b\mu^N N^{\gamma_c}, \tag{1.10}$$

while for the case $h = 0$, $\mathcal{N}_{\text{cone+plane}}$ will have the same dependence as in Eq. (1.10) but with a critical exponent γ_{cp}. Note that the effective coordination number μ is lattice dependent but does not depend on the boundary and is identical for both cases [28]. The work done against the entropic force in bringing the tip of the cone from afar into contact with the plane is

$$W = \int_a^R \mathcal{A}\frac{k_B T}{h} dh = \mathcal{A}k_B T \ln\frac{R}{a} = \mathcal{A}\nu k_B T \ln N, \tag{1.11}$$

where we used Eq. (1.8). Note that unlike γ that depends on the boundary conditions, the exponent ν is the same for the confined polymer and for a polymer in free space [22]. The work can also be computed from the change in the free energy of the system between the initial and final state, due

to the change in the entropy, i.e.,

$$\Delta\mathcal{F} = -T\Delta\mathcal{S} = T\mathcal{S}_{\text{cone}} - T\mathcal{S}_{\text{cone+plane}} = k_B T(\gamma_c - \gamma_{cp}) \ln N, \tag{1.12}$$

where we used Eq. (1.10) and the entropy $\mathcal{S} = -k_B \ln \mathcal{N}$. Equating W and $\Delta\mathcal{F}$, results in

$$\mathcal{A} = \frac{\gamma_c - \gamma_{cp}}{\nu} = \eta_{cp} - \eta_c. \tag{1.13}$$

In the final equality we used Eq. (1.4).

Thus, the entropic force between a cone and a plane that is mediated by a long polymer is expressed in universal terms. Its amplitude is independent of the microscopic details of the molecule. It will depend on the geometry of the cone and on the presence of steric interaction between the monomers. This argument is not specific to the case of a plane and a cone and can be applied to any pair of SF surfaces. In fact, a point in space is also SF, and thus a polymer anchored to a point in the vicinity of a SF object will experience a similar force.

1.4 Winding statistics of polymers

Another universal property of a polymer is its winding angle φ around a point (in $d = 2$) or line (in $d = 3$) when $N \to \infty$. Note that φ is the *total accumulated angle* of the steps along the walk. (It is *not* defined modulus 2π.) This problem has been studied extensively over the last sixty years [29, 30, 31, 32, 33, 34, 35, 36, 37, 38, 39, 40, 41, 42, 43, 44, 45], and has implications in various fields of statistical physics. Apart from the conformations of polymers, it is relevant for example to flux lines in superconductors [38]. Below we review in short what is known and unknown about the winding statistics of polymers.

The first result by Spitzer [29] showed that the probability distribution for the winding angle φ of a planar Brownian path around a point for large times t is

$$\lim_{t\to\infty} p\left(x = \frac{2\varphi}{\ln t}\right) = \frac{1}{\pi}\frac{1}{1+x^2}, \tag{1.14}$$

which is rather pathological since the averages $\langle|\varphi|\rangle$ and $\langle\varphi^2\rangle$ are both infinite due to the slow $x-$decay in Eq (1.14). The non-physical behavior originates from the fact that when a segment of the Brownian path approaches a *point* center, it can wind around it an infinite amount of times.

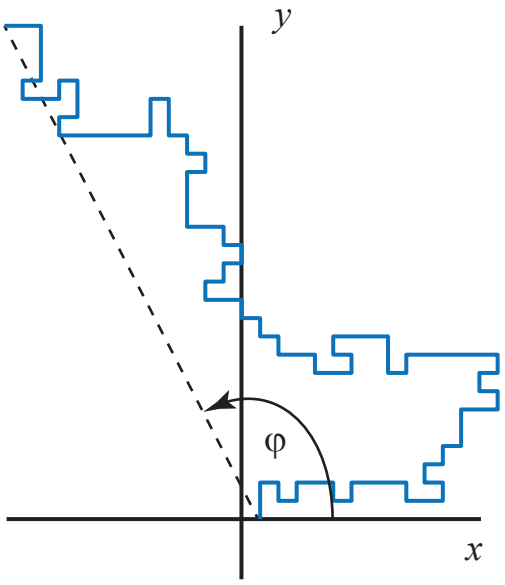

FIGURE 1.5: Winding angle of a planar SAW.

While this is true in an idealized system, in reality one expects that the polymer or Brownian particle will not be able to get infinitely close to the excluded center and a minimal distance will be imposed. For a lattice walk the cutoff distance is of the order of the lattice constant. When the minimal distance is incorporated into the model, the winding angle distribution in large t becomes [33]

$$\lim_{t\to\infty} p\left(x = \frac{2\varphi}{\ln t}\right) = \frac{\pi}{4\cosh^2(\pi x/2)}. \tag{1.15}$$

For a RW on a lattice the diffusion the diffusion time t is proportional to the number of steps N in the walk. The results in Eqs. (1.14) and (1.15) were derived and verified by several methods, e.g., solution of the diffusion equation [29, 30] and conformal mapping [38].

For planar self-avoiding walks [32, 34, 45], it was shown using conformal invariance [45] that the winding angle follows a Gaussian distribution,

$$\lim_{N\to\infty} p\left(x = \frac{\varphi}{2\sqrt{\ln N}}\right) = \frac{e^{-x^2}}{\sqrt{\pi}}. \tag{1.16}$$

In three dimensions, the winding of a RW around an infinite line is practically identical with the two dimensional case since the steps in the plane perpendicular to the line are independent of the steps in the parallel direction. Therefore, the same distribution is expected for long walks. The problem of a SAW winding around a line, however, is more complicated. Rudnick and Hu [34]

considered a self-avoiding walk in $d = 4 - \epsilon$ and found that to first order in ϵ,

$$p \propto \exp\left(-\frac{\varphi^2 \epsilon}{8 \ln N}\right). \tag{1.17}$$

Surprisingly, this result coincides with Eq. (1.16) for $\epsilon = 2$. However, no exact result is known for the distribution of a self-avoiding walk around a rod. Moreover, in recent simulations by Walter *et al.* [41], it was found that $p(\varphi)$ decreases slower than a Gaussian function, at odds with the first order ϵ-expansion results.

Due to the slow approach of the distribution to the asymptotic form (such as $\langle \varphi^2 \rangle \sim \ln N$ for planar self-avoiding walks), in order to verify the results in Eqs. (1.15), (1.16) and (1.17) in simulations, one has to use very long random and SAWs. This can be challenging since traditionally, in order to measure the winding angle of an N-step walk, one has to trace all the sites visited by the walk, which takes time of $O(N)$. Moreover, the generation of a large ensemble of long SAWs is difficult on its own, due to the need to check for intersections of the walk with itself. In Chapter 5 we improve upon known measurements of the winding angle of RWs and SAWs by using a new implementation of the pivot algorithm that was introduced by Clisby in recent years [2, 26]. In addition to verifying the theoretical predictions in Eq. (1.15) for RWs and in Eq. (1.16) for planar SAWs, we gain new intuition on the winding properties of SAW in $d = 3$.

1.5 Structure of the Thesis

In Chapter 2, we calculate analytically the force amplitude $\mathcal{A}$ for an IP anchored near a SF surface. We derive a relation between the statistics of a long IP near a SF object and the electrostatic potential of a point particle near a conducting surface with similar geometry. We also compute the entropic pressure on the surface, the monomer density and the end-point distribution.

For polymers in good solvents, it is more difficult to obtain such results numerically and lattice simulations are often used to compute universal properties of polymers. In Chapter 3 we discuss the definition of a local entropic pressure in a lattice model for a polymer. It is shown that the usual definition of the pressure must be adjusted in order to get a behavior that is consistent with the pressure in a continuous system.

In Chapter 4 we present the results of numerical simulations of RWs and SAWs on a square and cubic lattice near infinite wedges and cones. We study the critical exponents and end-point distribution of the walks. It is shown that the end-point distribution of SAWs is more complicated

than that of a RW in similar geometry. For a SAW in a wedge (dimension $d = 2$), we find that the distribution deviates from theoretical predictions and discuss this result.

In Chapter 5 we study numerically the winding angle of RWs and SAWs on the square and cubic lattice. We confirm the theoretical predictions for RWs and SAWs in $d = 2$ and find some surprising behavior for SAWs in $d = 3$. The results in $d = 3$ are then discussed using scaling arguments that are valid for the case of $d = 2$. We demonstrate that these arguments fail for SAWs in $d = 3$.

Chapter 2

Ideal Polymers in Scale-Free Spaces[1]

In this Chapter, we consider a setup where one end of a long IP is held at position $\mathbf{h}$ relative to a special point of a SF boundary such as the tip of the cone in Figure 2.1. When the point where the polymer is anchored is not along the symmetry axis of the surface, the force exerted on the anchoring point of the polymer as a result of the repulsive surface can be separated to components as is shown in the figure, where $F_{\hat{\mathbf{h}}}$ is parallel to $\mathbf{h}$ and $F_{\hat{\mathbf{s}}}$ is perpendicular to $\mathbf{h}$. This is a simplified version of the geometry that was considered in Section 1.3, where the plane is replaced by a point. We rewrite Eq. (1.9) to describe the parallel component,

$$F_{\hat{\mathbf{h}}} = \mathbf{F} \cdot \mathbf{h} = \mathcal{A}\frac{k_B T}{h}. \tag{2.1}$$

In a non-symmetric situation, as depicted in Figure 2.1, the force may have additional components in non-radial direction $\hat{\mathbf{s}} \perp \hat{\mathbf{h}}$ which is given by

$$F_{\hat{\mathbf{s}}} \equiv \mathbf{F} \cdot \hat{\mathbf{s}} = \mathcal{A}(\hat{\mathbf{h}}, \hat{\mathbf{s}})\frac{k_B T}{h}, \tag{2.2}$$

where the value of the dimensionless amplitude $\mathcal{A}(\hat{\mathbf{h}}, \hat{\mathbf{s}})$ depends both on the direction of the point where the polymer is held and on the direction of the particular force component. Using a similar argument as was given in Section 1.3, the force amplitude will be equal to the difference in the critical exponent η for a polymer attached to a cone, η_c, and a polymer in free space, η_{f}. Since for IPs $\eta_{\mathrm{f}} = 0$, Eq. (1.13) becomes

$$\mathcal{A} = \eta_c. \tag{2.3}$$

Below we derive this form of the entropic force for IPs in a different approach that the one taken in Section 1.3, and relate the force amplitude to other properties of the system like the distribution

[1] The work presented in this chapter was published in [46].

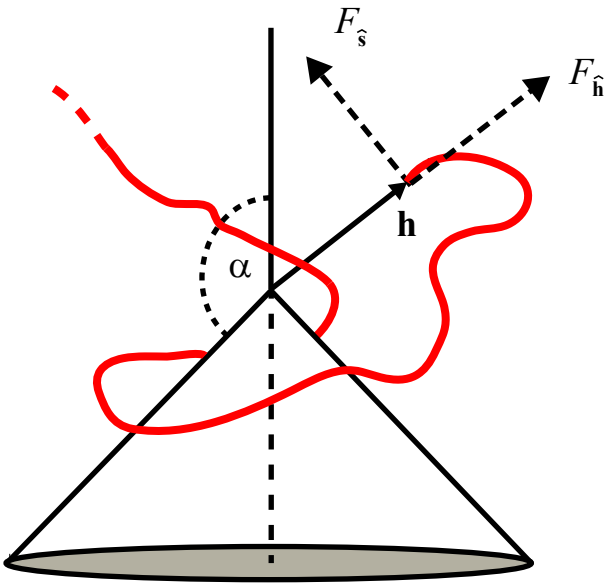

FIGURE 2.1: Polymer with one end held at position **h** from a scale-free surface. The entropic force between the polymer and the surface, which is also the force that acts on the point that holds the end of the polymer has component $F_{\hat{\mathbf{h}}}$ parallel to the vector **h**, and components $F_{\hat{\mathbf{s}}}$ perpendicular to that direction.

of the pressure on the surface.

2.1 Ideal polymers and diffusion

2.1.1 Green's function G and the survival probability Z

IP statistics are closely related to the statistics of RWs and diffusion problems [47]. An IP with $N+1$ monomers can be modeled as an N-step RW. Consider a RW starting from the point **h** on a d-dimensional hypercubic lattice. The total number of such walks is $\mathcal{N}_f(N) = (2d)^N$. In the presence of confining boundaries, we denote the total number of walks starting from **h** which *do not* cross the boundaries as $\mathcal{N}_{\rm nc}(\mathbf{h}, N)$, and the number of walks which start at **h** and end at **r** without crossing the boundaries as $\mathcal{N}_{\rm nc}(\mathbf{h}, \mathbf{r}, N)$. In order to investigate the properties of long polymers in confined spaces we focus on the following two functions: the (normalized) partition function (or random walker survival probability),

$$Z(\mathbf{h}, N) = \frac{\mathcal{N}_{\rm nc}(\mathbf{h}, N)}{\mathcal{N}_f(N)}, \tag{2.4}$$

and the Green function (or propagator),

$$G(\mathbf{h},\mathbf{r},N)=\frac{\mathcal{N}_{\rm nc}(\mathbf{h},\mathbf{r},N)}{a^d\mathcal{N}_f(N)}. \tag{2.5}$$

The division by the volume of lattice cell a^d converts the probability into probability density in the continuum description. When the relevant distances of the problem are much larger than the lattice constant a, both functions can be approximated as continuous functions which obey the diffusion equations [47],

$$\begin{aligned}&\frac{\partial Z(\mathbf{h},N)}{\partial N}=D\nabla^2_{\mathbf{h}}Z(\mathbf{h},N),\\&Z(\mathbf{h},0)=1,\end{aligned} \tag{2.6}$$

$$\begin{aligned}&\frac{\partial G(\mathbf{h},\mathbf{r},N)}{\partial N}=D\nabla^2_{\mathbf{r}}G(\mathbf{h},\mathbf{r},N),\\&G(\mathbf{h},\mathbf{r},0)=\delta^d(\mathbf{h}-\mathbf{r}),\end{aligned} \tag{2.7}$$

where the diffusion constant

$$D=\frac{a^2}{2d}, \tag{2.8}$$

while the subscripts $\mathbf{h}$ and $\mathbf{r}$ of the Laplacians indicate variables with respect to which the derivatives are taken. In order to exclude all the walks that cross the boundaries, we require that both Z and G vanish on the boundaries. In that respect, a long polymer near a *repulsive* wall corresponds to diffusion near an *absorbing* surface. In continuum, the persistence length ℓ_p replaces the lattice constant a in determination of D. Our formalism applies only to polymers significantly longer than ℓ_p and is not applicable to short (semi-flexible) polymers.

Since either end of a RW can be considered its beginning or end, the Green function satisfies the reciprocity relation [48]

$$G(\mathbf{r}_1,\mathbf{r}_2,N)=G(\mathbf{r}_2,\mathbf{r}_1,N). \tag{2.9}$$

For example, the Green function for a polymer in free space (no boundaries present), is

$$G(\mathbf{h},\mathbf{r},N)=\left(\frac{1}{4\pi DN}\right)^{d/2}\exp\left[-\frac{(\mathbf{r}-\mathbf{h})^2}{4DN}\right]. \tag{2.10}$$

The partition and Green functions are related by

$$Z(\mathbf{h}, N) = \int G(\mathbf{h}, \mathbf{r}, N) d^d\mathbf{r}. \tag{2.11}$$

From G and Z we can calculate the monomer density at a point $\mathbf{r}$ in the allowed space,

$$\rho_N(\mathbf{h}, \mathbf{r}) = \frac{\int_0^N G(\mathbf{h}, \mathbf{r}, n) Z(\mathbf{r}, N-n) dn}{Z(\mathbf{h}, N)}. \tag{2.12}$$

The integrand in Eq. (2.12) is constructed from the probability that the n'th monomer will reach the point $\mathbf{r}$ [proportional to $G(\mathbf{h}, \mathbf{r}, n)$], multiplied by the probability that the subsequent part of the chain will not touch the boundary [proportional to $Z(\mathbf{r}, N-n)$]. The integral over all the monomers is normalized by the overall survival probability of the N-step walk starting from $\mathbf{h}$, $Z(\mathbf{h}, N)$. The expression in the numerator decays with increasing N due to the absorbing boundary condition. Since $\int G(\mathbf{h}, \mathbf{r}, n) Z(\mathbf{r}, N-n) d^d\mathbf{r} = Z(\mathbf{h}, N)$ independently of the value of n, the total number of monomers is $\int \rho_N(\mathbf{h}, \mathbf{r}) d^d\mathbf{r} = N$. In most of the examples in this Chapter we will consider the monomer density for infinite polymers, and therefore the total number of monomers will be infinite. Both G and Z in the integrand of Eq. (2.12) satisfy the diffusion equations with absorbing boundaries, i.e. they both vanish at the boundaries, and approach them with finite slopes. Therefore, the density itself vanishes quadratically $\mathbf{r}$ approaches the boundary. Note that for convenience, we take $\mathbf{h}$ to be strictly *inside* the allowed space, so that the denominator in Eq. (2.12) remains finite.

2.1.2 Properties of G and Z in scale-free spaces

In the presence of a scale-free surface, neither Eqs. (2.6) and (2.7) nor the boundary surface introduce any length scale into the problem. Therefore, the partition function depends only on the dimensionless ratio $\mathbf{w} \equiv \mathbf{h}/\sqrt{DN}$, i.e. $Z(\mathbf{h}, N) = H(\mathbf{w})$, where H is a dimensionless function. In terms of the reduced variable Eq. (2.6) becomes [19]

$$\nabla^2_{\mathbf{w}} H + \frac{1}{2} \mathbf{w} \cdot \vec{\nabla}_{\mathbf{w}} H = 0. \tag{2.13}$$

When the size of the polymer is significantly larger than h, i.e., $w \ll 1$ the second term in the equation becomes negligible, and the equation reduces to

$$\nabla^2_{\mathbf{w}} H = 0. \tag{2.14}$$

In the presence of scale-free surfaces, it is useful to describe the polymer in a coordinate system that separates the radial part from all other coordinates, as is done in spherical or polar coordinates. In many of these systems [49], the Laplace operator can be written in the form

$$\nabla^2_{\mathbf{w}} = w^{1-d} \frac{\partial}{\partial w} \left(w^{d-1} \frac{\partial}{\partial w} \right) + w^{-2} \nabla^2_{S_{d-1}}, \tag{2.15}$$

where $\nabla^2_{S_{d-1}}$ is the Laplace-Beltrami operator acting on the $d-1$ non-radial coordinates [50]. Since the boundary conditions on H are independent of w, we expect that for $w \ll 1$ the solution can be expressed as a product of a power of w and an angular function $\Theta(\theta_1, \ldots, \theta_{d-1}) \equiv \Theta(\hat{\mathbf{w}})$, where $\hat{\mathbf{w}} \equiv \mathbf{w}/w$. In the limit $w \ll 1$ the large-N expression [Eq. (1.7)] becomes applicable, and it follows that $Z \sim N^{-\eta/2}$. This means that for $w \ll 1$,

$$H(\mathbf{w}) \approx w^{\eta} \Theta(\hat{\mathbf{w}}) \quad \text{or} \quad Z(\mathbf{h}) \approx (h/\sqrt{DN})^{\eta} \Theta(\hat{\mathbf{h}}) \tag{2.16}$$

By substituting this expression into Eq. (2.14) and using Eq. (2.15) we obtain an eigenvalue equation

$$\nabla^2_{S_{d-1}} \Theta = \eta(2 - d - \eta)\Theta, \tag{2.17}$$

that determines η and the corresponding eigenfunction $\Theta(\hat{\mathbf{w}})$. This equation has an infinite number of eigenvalues and eigenfunctions, but, since Z (or H) is a positive function, we are interested only in the "ground state" solution that is always positive, and corresponds to the lowest value of η. For example [19], in the case of a polymer in a wedge of opening angle 2α in $d = 2$, there is only one angular variable θ measured, say, from the symmetry axis of the wedge; in this system $\eta = \pi/2\alpha$, while $\Theta(\theta) = \cos(\pi\theta/2\alpha)$. For a $d = 3$ circular cone, of apex angle (between the symmetry axis and the surface of the cone) α, the value of η is determined [19] by finding the smallest degree η of Legendre function satisfying $P_\eta(\cos\alpha) = 0$. The corresponding $\Theta(\theta, \phi) = P_\eta(\cos\theta)$, where θ is measured from the symmetry axis, and the function is independent of ϕ due to symmetry of the problem. For a d-dimensional cone, Eq. (2.17) was solved by Ben-Naim and Krapivsky [51]. Their

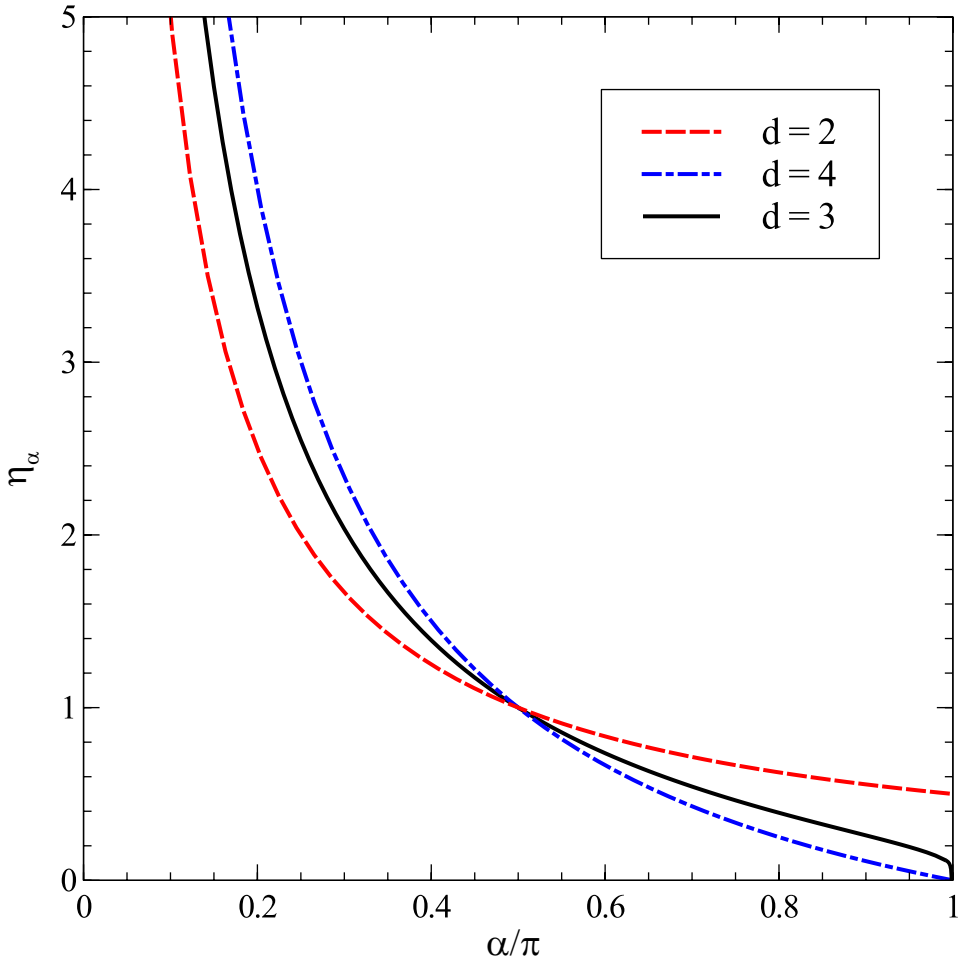

FIGURE 2.2: Force amplitude η for an infinite IP anchored near an infinite d-dimensional cone with opening angle α [51, 18], defined so that the polymer is inside the cone for $\alpha < \pi/2$ and is outside the cone for $\alpha > \pi/2$ (Figure 2.1). The values were computed using Eq. (2.17).

solution was used in [19, 18] to find the force amplitude for IPs near cones. These amplitudes are plotted in Figure 2.2 as a function of the opening angle α. Note that the amplitude increases as we compress the polymer into a smaller volume in space by decreasing α. The loss of entropy is maximal when $\alpha \to 0$ and the infinite polymer is forced to assume the shape of a semi-infinite line, thus, the force amplitude diverges in this limit. Another example for a geometry where Eq. (2.17) can be solved is a cone with elliptical cross section (see [52]).

From Eq. (2.16) the free energy of the polymer is $\mathcal{F} = -k_B T[\eta \ln h + \ln \Theta(\hat{\mathbf{h}})] + \text{const.}$, from which the force is compiled as

$$F_{\hat{\mathbf{h}}} = -\frac{\partial \mathcal{F}}{\partial r} = \eta \frac{k_B T}{h}, \tag{2.18}$$

i.e., the amplitude that was defined in Eq. (2.1), $\mathcal{A} = \eta$, is independent of the direction of $\hat{\mathbf{h}}$, as stated in Eq. (2.1). For the amplitude in one of the perpendicular directions $\hat{\mathbf{s}}$, we need to take a

similar derivative with respect to coordinate $r_{\hat{\mathbf{s}}}$ perpendicular to $\hat{\mathbf{h}}$.

$$F_{\hat{\mathbf{s}}} = -\frac{\partial \mathcal{F}}{\partial r_{\hat{\mathbf{s}}}} = \frac{\Theta^{(\hat{\mathbf{s}})}(\hat{\mathbf{h}})}{\Theta(\hat{\mathbf{h}})}\frac{k_B T}{h}, \tag{2.19}$$

where $\Theta^{(\hat{\mathbf{s}})}$ denotes a (angular) derivative of Θ on a unit sphere in the direction of $\hat{\mathbf{s}}$, such as $\partial/\partial\theta$ in the spherical coordinate system. Thus the amplitude in Eq. (2.1) is $\mathcal{A}(\hat{\mathbf{h}}, \hat{\mathbf{s}}) = \Theta^{(\hat{\mathbf{s}})}(\hat{\mathbf{h}})/\Theta(\hat{\mathbf{h}})$.

If the end of a polymer is tethered to the origin by a string of length h, but is allowed to fluctuate in non-radial direction, the function $\Theta(\hat{\mathbf{h}})$, that must be normalized, is the probability density for the orientation $\hat{\mathbf{h}}$. Since Θ is positive in the allowed space (and vanishes only on the boundaries) it will frequently have a single maximum, such as the position of the symmetry axis in the case of a wedge or a cone, although multiple maxima can be created by, say, properly shaping the cross section of a cone. This probability is independent of temperature, and therefore the fluctuations of the end-point will also be temperature independent. In simple geometries the fluctuations will be "large", i.e., occupy most of the available directions.

The Green function has dimensions [length]$^{-d}$ and satisfies Eq. (2.7). It can be written using the same dimensionless variable, $\mathbf{w}$ as well as $\mathbf{v} \equiv \mathbf{r}/\sqrt{DN}$, as

$$G(\mathbf{h}, \mathbf{r}, N) = (DN)^{-d/2} Y(\mathbf{w}, \mathbf{v}), \tag{2.20}$$

where Y is a dimensionless function. For $DN \gg h^2$ ($w \ll 1$) the system loses its detailed dependence on the initial condition, resulting in a function of $\mathbf{r}$ with $\mathbf{h}$ dependent prefactor. Thus, we attempt a solution of the form

$$\tilde{G}(\mathbf{r}, N) = C g(r, N) \Theta(\hat{\mathbf{r}}), \tag{2.21}$$

where unit vector $\hat{\mathbf{r}} \equiv \mathbf{r}/r = \{\theta_1, \ldots \theta_{d-1}\}$ describes the non radial coordinates, and C is a (dimensional) prefactor containing h and D. For $g(r, N)$ we use the expression

$$g(r, N) = r^x N^y \exp\left(-\frac{r^2}{4DN}\right). \tag{2.22}$$

Note that the exponent $\exp\left(-\frac{r^2}{4DN}\right)$ is *exactly* the same as in description of an IP in free space [Eq. (2.10)]. By using Eqs. (2.15), (2.21) and (2.22) in Eq. (2.7) we get

$$\left[\frac{r^2}{DN}\left(\frac{d}{2} + x + y\right) + x(2 - d - x)\right]\Theta = \nabla^2_{S_{d-1}}\Theta. \tag{2.23}$$

In order for Eq. (2.23) to hold for arbitrary values of r, the coefficient of r must vanish, leading to

$$\frac{d}{2} + x + y = 0. \tag{2.24}$$

The value of x is determined by the eigenvalue equation

$$\nabla^2_{S_{d-1}}\Theta = x(2-d-x)\Theta. \tag{2.25}$$

This (angular) equation coincides with Eq. (2.17), but, unlike H in Eq. (2.14), the function $\tilde{G}$ that we are seeking is *not* harmonic. Obviously, the value of x in this equation will coincide with η that was found in the calculation of H, as well as the function $\Theta(\hat{\mathbf{r}})$ will be the same as $\Theta(\hat{\mathbf{w}})$ describing H. (We seek the "ground state" value of x since the function $\tilde{G}$ must be positive.) We shall henceforth substitute η for x. It is shown below that such value of x indeed produces a correct description of the partition function.

Thus we have a solution for the diffusion equation near a scale-free surface. This solution *does not* satisfy the initial condition in Eq. (2.7) and does not properly describe the statistics of short polymers, where the size of the polymer approaches h. However, $\tilde{G}$ approaches the exact solution for the Green function of long ($\sqrt{DN} \gg h$) IPs near SF surfaces. Since the form of the Green function must be described by Eq. (2.20), we must choose the constant in Eq. (2.21) as $C = ch^\eta/D^{\eta+d/2}$, where c is a dimensionless constant (that depends on $\hat{\mathbf{h}}$), leading to

$$\tilde{G} = c\left(\frac{1}{\sqrt{DN}}\right)^d \left(\frac{h}{\sqrt{DN}}\right)^\eta \left(\frac{r}{\sqrt{DN}}\right)^\eta \mathrm{e}^{-r^2/4DN}\Theta(\hat{\mathbf{r}}). \tag{2.26}$$

Integration of this expression over the d-dimensional space confined by the surfaces, leads (up to a dimensionless prefactor) to the value of $Z(\mathbf{h}, N) = H(\mathbf{w}) \sim (h/\sqrt{DN})^\eta = w^\eta$, i.e., the correct behavior of Z, thus justifying our identification $x = \eta$.

Note that from the definition of G [Eq. (2.5)] and the boundary conditions, Θ must be a positive function that vanishes on the boundaries. In Figure 2.3 $\tilde{G}$ is plotted for the case of an ideal polymer attached to a wedge with opening angle $\alpha = 3\pi/4$.

When the geometry is complicated, and analytical solution of Eq. (2.25) cannot be obtained, the force amplitude can be evaluated numerically. This process can be simplified by considering the

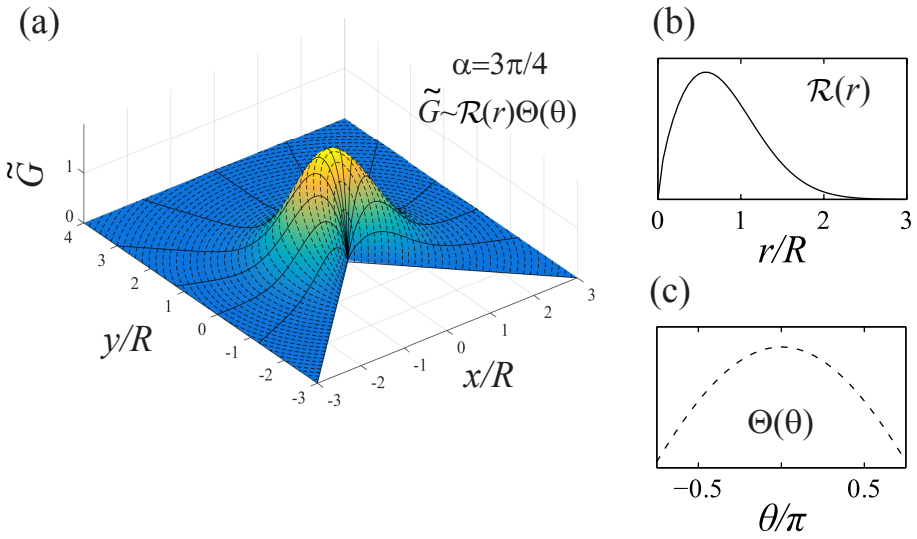

FIGURE 2.3: End-point distribution of a long two-dimensional ideal polymer (arbitrary units) attached to the corner of an excluded wedge with opening angle $\alpha = 3\pi/4$. The distance from the corner is scaled with the root mean square end-to-end distance of a polymer in free space R. The distribution is composed of a product of a radial and angular functions. The solid lines in (a) represent curves with constant θ, which all have the same form depicted in (b). Similarly curves with constant r are represented by dashed lines in (a) and their form is shown in (c).

average position of the polymer end point. Using Eq. (2.26), we find

$$\begin{aligned} R^2_{\tilde{G}} &\equiv \frac{\int r^2 \tilde{G}(\mathbf{r}, N) d^d\mathbf{r}}{\int \tilde{G}(\mathbf{r}, N) d^d\mathbf{r}} = \frac{\int r^{\eta+d+1} e^{-r^2/4DN} dr}{\int r^{\eta+d-1} e^{-r^2/4DN} dr} \\ &= 4DN \frac{\int y^{(\eta+d)/2} e^{-y} dy}{\int y^{(\eta+d-2)/2} e^{-y} dy} = 4DN \frac{\Gamma\left[\frac{\eta+d}{2}+1\right]}{\Gamma\left[\frac{\eta+d}{2}\right]} \\ &= 2DN(\eta+d), \end{aligned} \tag{2.27}$$

where Γ is the gamma function (which has the property $\Gamma[t+1]/\Gamma[t] = t$) and we used the change of variables $y = r^2/4DN$. Since $\tilde{G}$ approaches the exact solution in the limit $N \to \infty$ we can write a formula for the force amplitude,

$$\eta = \lim_{N\to\infty} \frac{R_e^2}{2DN} - d. \tag{2.28}$$

Note that in free space $\eta = 0$, and from Eqs. (2.8) and (2.27) we recover the usual mean squared end-to-end distance for an IP/RW $R^2 = a^2 N$. When we confine the polymer by holding it near the boundary the mean squared end-to-end distance grows band it is still linearly proportional to the number of monomers. Using Eq. (2.28), the force amplitude can be evaluated from numerical solution of the diffusion equation or from simulations of random walks in confined spaces [53].

2.2 Monomer density and entropic pressure on the surface

2.2.1 Entropic pressure on a plane

The problem of an IP near a repulsive plane was considered in [54, 14, 55]. In this subsection we expand the approach used in [54] to general d and set the stage for the treatment of more complicated surfaces.

In d dimensions positions in a half-space are described by $\mathbf{r} = (r_1, ..., r_d) \equiv (\mathbf{R}, r_\perp))$ with $r_\perp > 0$. For an IP with one end fixed at $\mathbf{h} = (0, \ldots, 0, h)$, the Green function can be found using the method of images [56]:

$$G(\mathbf{h}, \mathbf{r}, N) = \left(\frac{1}{4\pi DN}\right)^{d/2} \exp\left(-\frac{R^2}{4DN}\right) \times \left\{\exp\left(-\frac{(r_\perp - h)^2}{4DN}\right) - \exp\left(-\frac{(r_\perp + h)^2}{4DN}\right)\right\}. \quad (2.29)$$

The corresponding partition function can be found by integrating Eq. (2.29) over $\mathbf{r}$,

$$Z(\mathbf{h}, N) = \operatorname{erf}\left(h/\sqrt{4\pi DN}\right). \quad (2.30)$$

Using Eqs. (2.12), (2.29) and (2.30), and taking the $N \to \infty$ limit we get for $d > 2$,

$$\rho(\mathbf{h}, \mathbf{r}) = \frac{1}{4D} \frac{\Gamma\left(\frac{d}{2} - 1\right)}{\pi^{d/2}} \frac{r_\perp}{h} \left\{[R^2 + (r_\perp - h)^2]^{1-d/2} - [R^2 + (r_\perp + h)^2]^{1-d/2}\right\}.$$

(Henceforth, quantities without index N will denote infinite polymer limit.) For $d = 2$,

$$\rho(\mathbf{h}, \mathbf{r}) = \frac{1}{4\pi D} \frac{r_\perp}{h} \ln \frac{R^2 + (h + r_\perp)^2}{R^2 + (h - r_\perp)^2}. \quad (2.31)$$

When a planar surface is distorted by infinitesimal amount $\Delta(\mathbf{R})$ [by shifting it from $r_\perp = 0$ to $r_\perp = \Delta(\mathbf{R})$], the resulting change in the number of available conformations modifies the free energy of the polymer by an amount

$$\Delta\mathcal{F}_N = \int\limits_{r_\perp = 0} [P_N(\mathbf{R})\Delta(\mathbf{R})]\, d^{d-1}\mathbf{R} + O(\Delta(\mathbf{R})^2), \quad (2.32)$$

where $P_N(\mathbf{R})$ is the entropic pressure of the polymer on the surface at position $\mathbf{R}$. Thus, the pressure represents a variational derivative of the free energy. For a polymer with one end held at

h it can be written in terms of the Green function [54] as

$$P_N(\mathbf{h},\mathbf{R}) = \frac{k_B T D}{Z(\mathbf{h},N)} \int_0^N \frac{\partial G(\mathbf{r},\mathbf{h},n)}{\partial r_\perp} \frac{\partial Z(\mathbf{r},N-n)}{\partial r_\perp} dn, \tag{2.33}$$

where $\mathbf{r} = (\mathbf{R}, r_\perp)$, and the derivatives are evaluated at $r_\perp = 0$. Equation (2.12) can be used to rewrite this expression via the monomer density $\rho(\mathbf{r})$,

$$P_N(\mathbf{h},\mathbf{R}) = \frac{D k_B T}{2} \frac{\partial^2}{\partial r_\perp^2} \rho_N(\mathbf{h},\mathbf{r}). \tag{2.34}$$

From Eqs. (2.31) and (2.34) we find the polymer pressure on the plane in the limit $N \to \infty$,

$$P(R) = \frac{\Gamma(d/2)}{\pi^{d/2}} \frac{k_B T}{(R^2+h^2)^{d/2}}. \tag{2.35}$$

It should be noted that the infinite-N expressions for the density and the pressure apply to finite-N situations when $DN \gg r^2, h^2$. For smaller N these quantities cannot be expressed in such simple terms. If a polymer is confined to a finite volume and both its ends are free to move, a different approach needs to be used to calculate the pressure distribution (see, e.g., [57]).

2.2.2 Relation between the monomer density and electrostatic potentials

The calculation of the monomer density $\rho_N(\mathbf{h},\mathbf{r})$ in Eq. (2.12) requires integration of the product $G(\mathbf{h},\mathbf{r},n)Z(\mathbf{r},N-n)$ over n varying from 0 to N. In free space the Green function $G(\mathbf{h},\mathbf{r},n)$ is very small for n such that $\sqrt{Dn} \ll |\mathbf{h}-\mathbf{r}|$, because a random walk from **h** is "too short" to reach **r**. Similarly, for $\sqrt{Dn} \gg |\mathbf{h}-\mathbf{r}|$ the walk is "too long" to be at **r** with a significant probability. Thus, G in free space peaks when $\sqrt{Dn}$ is of order of $|\mathbf{h}-\mathbf{r}|$. In the presence of absorbing boundaries, the large n decay is even stronger. In the presence of scale-free surfaces, for long polymers ($DN \gg h^2, r^2$) it is possible to divide the integral $\int_0^N$ in Eq. (2.12) into $\int_0^{n_1} + \int_{n_1}^N$, where $r^2, h^2 \ll Dn_1 \ll DN$, and show that for fixed $x_1 = n_1/N$, in the limit $N \to \infty$, the second integral divided by $Z(\mathbf{h},N)$ vanishes. This feature is quantitatively demonstrated in Appendix A. Thus, only the first integral includes a significant contributions to the density. In its range ($n < n_1 \ll N$) we can assume $Z(\mathbf{r},N-n) \approx Z(\mathbf{r},N)$ and take it out of the integration so that in the infinite-N limit the density is $\rho(\mathbf{h},\mathbf{r}) = \lim_{N\to\infty}[Z(\mathbf{r},N)/Z(\mathbf{h},N)] \int_0^\infty G(\mathbf{h},\mathbf{r},n)dn$, or using Eq. (2.16),

$$\rho(\mathbf{h},\mathbf{r}) = \frac{\Theta(\hat{\mathbf{r}})}{\Theta(\hat{\mathbf{h}})} \left(\frac{r}{h}\right)^\eta \int_0^\infty G(\mathbf{h},\mathbf{r},n)dn. \tag{2.36}$$

This simplification enables us to perform the integral and derive analytical expressions for the monomer density.

Since the density ρ in Eq. (2.36) depends only on the integral of G it is convenient to define

$$\Phi(\mathbf{h},\mathbf{r}) \equiv \int_0^\infty G(\mathbf{h},\mathbf{r},n)dn. \tag{2.37}$$

From Eq. (2.7),

$$\begin{aligned}\nabla^2_{\mathbf{r}}\Phi(\mathbf{h},\mathbf{r}) &= \int_0^\infty \nabla^2_{\mathbf{r}} G(\mathbf{h},\mathbf{r},n)dn \\ &= (1/D)(G(\mathbf{h},\mathbf{r},\infty) - G(\mathbf{h},\mathbf{r},0)) \\ &= -(1/D)\delta^d(\mathbf{h}-\mathbf{r}),\end{aligned} \tag{2.38}$$

i.e., Φ satisfies the electric Poisson equation for the potential of a point charge of size $\sim 1/D$ at $\mathbf{h}$ near a conducting surface. Consequently, the density at $\mathbf{r}$ and the electric potential are related by

$$\rho(\mathbf{h},\mathbf{r}) = \frac{\Theta(\hat{\mathbf{r}})}{\Theta(\hat{\mathbf{h}})}\left(\frac{r}{h}\right)^\eta \Phi(\mathbf{h},\mathbf{r}). \tag{2.39}$$

The function ρ and Φ for a wedge in $d=2$ with an opening angle $2\alpha = \pi/3$ are plotted in Figure 2.4.

2.2.3 Some properties of the density and the pressure

The expression for calculation of monomer density of an infinite IP in Eq. (2.36), requires knowledge of the exact Green function or electrostatic potential. These are frequently expressed as an infinite sum of functions. Since the polymer is anchored at $\mathbf{h}$, and the system is coarse grained so that the monomer size $a \to 0$, we expect to get a finite result from integrating the density in an arbitrary volume that contains $\mathbf{h}$. Thus, the density $\rho(\mathbf{h},\mathbf{r})$ is singular for $\mathbf{h}=\mathbf{r}$ and the series expansions of the density do not always converge. For a finite a, we would expect that this divergence would be truncated by the value that is obtained by substituting a into the function. Note that while the density diverges for $\mathbf{r}=\mathbf{h}$ when $a \to 0$, the integral of the density remaines finite. The simple expression for the pressure on flat surfaces in Eq. (2.34) can also be expanded in powers of r/h, but will converge only for $r < h$. Alternatively, it can be expanded in the powers of h/r, and will converge only for $h < r$. This situation will recur for more complicated surfaces discussed in the following section.

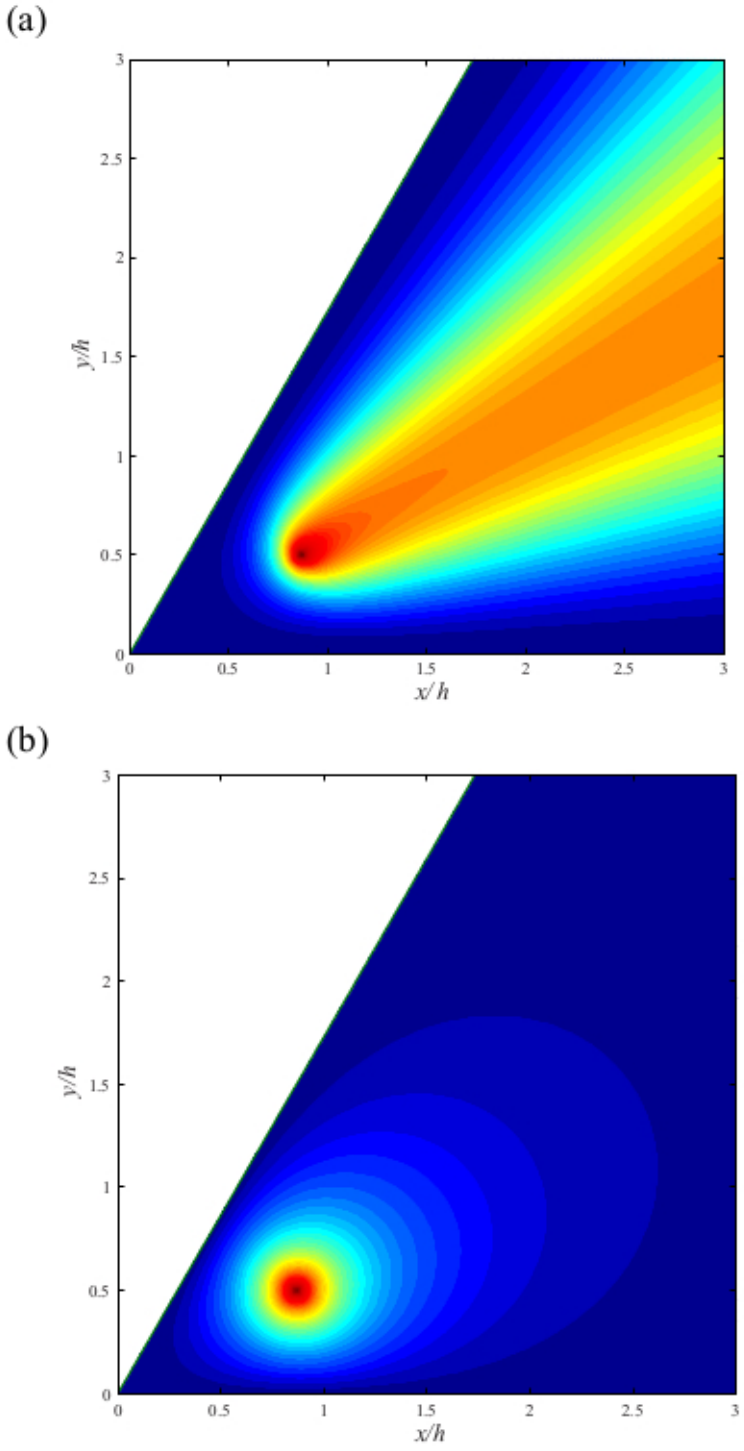

FIGURE 2.4: (a) Monomer density of an infinite IP anchored in a repulsive wedge with opening angle $2\alpha = \pi/3$. (b) The electric potential Φ of a point charge near a conducting surface of similar geometry. The functions plotted in (a) and (b) are related as in Eq. (2.39).

If the expression for the monomer density in an infinite polymer (2.36) is combined with the reciprocity relation of the Green function in Eq. (2.9), or Eq. (2.39) is combined with the reciprocity property of electrostatic potential, we can relate the monomer densities in the situation when the polymer starting point $\mathbf{r}_1$ and the observation point $\mathbf{r}_2$ interchange their roles

$$\rho(\mathbf{r}_1, \mathbf{r}_2) = \left[\frac{\Theta(\hat{\mathbf{r}}_2)}{\Theta(\hat{\mathbf{r}}_1)}\right]^2 \left(\frac{r_2}{r_1}\right)^{2\eta} \rho(\mathbf{r}_2, \mathbf{r}_1). \tag{2.40}$$

From Eq. (2.20) it follows that in scale-free geometries $G(\lambda\mathbf{r}_1, \lambda\mathbf{r}_2, \lambda^2 n) = \lambda^{-d} G(\mathbf{r}_1, \mathbf{r}_2, n)$, which can be used with Eq. (2.36) to obtain

$$\rho(\lambda\mathbf{r}_1, \lambda\mathbf{r}_2) = \lambda^{2-d} \rho(\mathbf{r}_1, \mathbf{r}_2). \tag{2.41}$$

(This relation can also be obtained from the properties of Φ under rescaling.) This means that the structure of the density function can be slightly simplified: If instead of variables $\mathbf{r}_1$ and $\mathbf{r}_2$ we use the direction of the two vectors and their lengths r_1 and r_2, when the ratio of the lengths is $x = r_2/r_1$, then by choosing $\lambda = 1/r_1$ in Eq. (2.41) we find that $\rho(\mathbf{r}_1, \mathbf{r}_2) = r_1^{2-d} f(x, \hat{\mathbf{r}}_1, \hat{\mathbf{r}}_2)$. We therefore expect that the calculation of density function will involve an expansion of the solution in the dimensionless ratio x.

Let us now consider a Kelvin transform of the coordinates where the new position is obtained by inverting the old position with respect to a sphere of radius h: $\mathbf{r}_2 = (h/r_1)^2 \mathbf{r}_1$ (Under this transformation $\mathbf{h}$ maps into itself.) If the potential $\Phi_1(\mathbf{h}, \mathbf{r}_1)$ of the original problem is known, then [58] $\Phi_2(\mathbf{h}, \mathbf{r}_2) \equiv (r_1/h)^{d-2} \Phi_1(\mathbf{h}, \mathbf{r}_1)$ also solves Eq. (2.38). Usually, performing a Kelvin transform requires similar transformation of the boundary surfaces, but in this case the boundary conditions are independent of the length r_1 and therefore are automatically satisfied for r_2. This relation together with Eq. (2.39) leads to the conclusion that

$$\rho(\mathbf{h}, \mathbf{r}_2) = (r_1/h)^{d-2-2\eta} \rho(\mathbf{h}, \mathbf{r}_1). \tag{2.42}$$

This feature conveniently connects the values of the density for, say, $r_1/h = y < 1$ with the values of density at $r_2/h = 1/y > 1$, i.e., the density for $r > h$ can be reconstructed from the density at $r < h$. For $r_1 \ll h$ the electrostatic potential $\Phi \sim \Theta(\hat{\mathbf{r}}_1) r_1^\eta / D h^{d-2}$, since in that region it satisfies the same equation as Z. Therefore, from Eq. (2.39) we find in that limit $\rho(\mathbf{h}, \mathbf{r}_1) \approx A[\Theta(\hat{\mathbf{r}}_1)]^2 r_1^\eta / D h^{d-2+2\eta}$, where A is a dimensionless constant. By using Eq. (2.42) we can now determine that for $r_2 =$

$h^2/r_1 \gg h$ the density is $\rho(\mathbf{h}, \mathbf{r}_2) \approx A[\Theta(\hat{\mathbf{r}}_2)]^2/Dr_2^{d-2}$ with *the same* coefficient A. The latter relation does not depend on h, as could be expected in that region. Since G is a solution of diffusion equation, the expression must include the prefactor $1/D$ of dimension $[\text{length}]^{-2}$. (The same conclusion follows for Eqs. (2.38) and (2.39).) Therefore, aside from angular term, the result is the only dimensionally possible expression for the density.

The method presented in subsection 2.2.1 to compute the entropic pressure of the polymer in a half-space can be generalized to any regular surface (i.e., any surface that appears flat when observed from an infinitesimal distance). For a general surface, we define the distortion $\Delta(\tilde{\mathbf{r}})$ to be in the direction perpendicular to the surface, where $\tilde{\mathbf{r}}$ is a point on the surface. The derivative with respect to $r_\perp$ in Eqs. (2.35) now represents derivative in the direction locally perpendicular to the surface.

The pressure on the boundary corresponds to the second derivative with respect to coordinate perpendicular to the boundary [Eq. (2.34)]. If $\mathbf{r}_2$ and $\mathbf{r}_1$ are related by a Kelvin transform, as mentioned above, and are on the boundary of the surface, then from Eq. (2.42) it follows that the pressures at corresponding points are related by

$$P(\mathbf{h}, \mathbf{r}_2) = (r_1/h)^{d+2-2\eta} P(\mathbf{h}, \mathbf{r}_1). \tag{2.43}$$

From these relations, by repeating the argument analogous to the one in the previous paragraphs, or directly from the expressions of ρ at very large and very small distances, we can establish that for $r_2 \gg h$ the expression for pressure has the h-independent dimensionally correct form $P(\mathbf{h}, \mathbf{r}_2) \approx B[\Theta^{(\hat{\mathbf{s}})}(\hat{\mathbf{r}}_2)]^2 k_B T/r_2^d$, where $\Theta^{(\hat{\mathbf{s}})}(\hat{\mathbf{r}}_2)$ is the derivative of Θ on the unit sphere in direction $\hat{\mathbf{s}}$ perpendicular to the boundary, evaluated on the boundary, and B is some dimensionless constant. Using the arguments outlined above we conclude that at short distances $r_1 \ll h$, the pressure becomes

$$P(\mathbf{h}, \mathbf{r}_1) \approx B[\Theta^{(\hat{\mathbf{s}})}(\hat{\mathbf{r}}_1)]^2 k_B T r_1^{2(\eta-1)}/h^{d+2(\eta-1)}, \tag{2.44}$$

with the same B.

2.2.4 Relating the pressure to the total force

From Eqs. (2.34) and (2.39) the expression for the pressure at a point on a surface can be written as

$$\begin{aligned} P(\mathbf{h},\mathbf{r}) &= \frac{Dk_BT}{2}\frac{\partial^2}{\partial r_\perp^2}\left[\frac{\Theta(\hat{\mathbf{r}})}{\Theta(\hat{\mathbf{h}})}\left(\frac{r}{h}\right)^\eta \Phi(\mathbf{h},\mathbf{r})\right] \\ &= Dk_BT\nabla_{\mathbf{r}}\left[\frac{\Theta(\hat{\mathbf{r}})}{\Theta(\hat{\mathbf{h}})}\left(\frac{r}{h}\right)^\eta\right]\cdot\nabla_{\mathbf{r}}\Phi(\mathbf{h},\mathbf{r}), \end{aligned} \tag{2.45}$$

where we used the fact that both functions vanish on the boundary and their gradients are parallel to each other and perpendicular to the boundaries. This expression can be used to calculate the total force acting in the direction of $\hat{\mathbf{h}}$ by integrating the projection of the force on the desired direction on the entire surface,

$$F_{\hat{\mathbf{h}}} = \int_S d\mathbf{S}\cdot\hat{\mathbf{h}}P(\mathbf{h},\mathbf{r}) = Dk_BT\int\nabla_{\mathbf{r}}\cdot\left\{\hat{\mathbf{h}}\nabla_{\mathbf{r}}\left[\frac{\Theta(\hat{\mathbf{r}})}{\Theta(\hat{\mathbf{h}})}\left(\frac{r}{h}\right)^\eta\right]\cdot\nabla_{\mathbf{r}}\Phi(\mathbf{h},\mathbf{r})\right\}d^d\mathbf{r} \tag{2.46}$$

By applying the divergence operator and using the fact that the function in the first square brackets is harmonic while the electrostatic potential satisfies Eq. (2.38) we find that,

$$\begin{aligned} F_{\hat{\mathbf{h}}} &= Dk_BT\int\hat{\mathbf{h}}\cdot\nabla_{\mathbf{r}}\left[\frac{\Theta(\hat{\mathbf{r}})}{\Theta(\hat{\mathbf{h}})}\left(\frac{r}{h}\right)^\eta\right](1/D)\delta^d(\mathbf{h}-\mathbf{r})d^d\mathbf{r} \\ &= k_BT\int\frac{\partial}{\partial r}\left[\frac{\Theta(\hat{\mathbf{r}})}{\Theta(\hat{\mathbf{h}})}\left(\frac{r}{h}\right)^\eta\right]\delta^d(\mathbf{h}-\mathbf{r})d^d\mathbf{r} \\ &= \eta k_BT/h\ , \end{aligned} \tag{2.47}$$

which coincides with the general expression for the force in Eq. (2.1) with $\mathcal{A}=\eta$, as was seen directly in Eq. (2.18).

Similar calculations can be performed for the force components in an arbitrary direction. If we choose some direction $\hat{\mathbf{s}}\perp\hat{\mathbf{h}}$, we can repeat the above calculation with the new projection direction $\hat{\mathbf{s}}$. Now on the first line of Eq. (2.47) we will have the product $\hat{\mathbf{h}}\cdot\nabla_{\mathbf{r}}$ replaced by $\hat{\mathbf{s}}\cdot\nabla_{\mathbf{r}}$, which will result in the derivative acting only on $\Theta(\hat{\mathbf{r}})$ in direction $\hat{\mathbf{s}}$ [such as $(1/r)(\partial/\partial\theta)$] in three-dimensional spherical coordinates) leading to exactly the same result as in Eq. (2.19).

2.3 Force, monomer density and pressure in specific geometries

We will now discuss the monomer density and the entropic pressure of an IP on a wedge in $d = 2$ and 3 a cone in $d = 3$. The Green functions for the cone and wedge geometries can be found in Appendix B. For simplicity throughout this section we consider cases where the end of the polymer is held along the symmetry axis of the cone or wedge.

2.3.1 Wedge in $d = 2$

Consider a wedge defined in polar coordinates by $-\alpha < \theta < \alpha$ [Figure 2.5(a)]. One end of an IP is held at a distance h from the corner, along the symmetry axis of the wedge. The Green function for this geometry is given in Appendix B [Eq. (B.1)]. In the range where $h^2 \ll DN$ and $r^2 \lesssim DN$, the sum in Eq. (B.1) becomes a power series and the lowest power dominates. Thus the Green function converges to the general form presented in Eq. (2.26). The force amplitude is the lowest power in the series (B.2), i.e.,

$$\eta = \pi/2\alpha. \tag{2.48}$$

In order to derive the monomer density in the wedge, we use Eq. (2.36). For $N \to \infty$ we get

$$\rho(\mathbf{r}) = \frac{1}{2\pi D} \cos\left(\frac{\pi\theta}{2\alpha}\right) \left(\frac{r}{h}\right)^{\pi/2\alpha} \times \tanh^{-1} \frac{2\cos(\pi\theta/2\alpha)}{(h/r)^{\pi/2\alpha} + (r/h)^{\pi/2\alpha}}. \tag{2.49}$$

The monomer density in a wedge with $\alpha = \pi/3$ is depicted in Figure 2.4. The derivative perpendicular to the surface in this geometry is $\frac{\partial}{\partial r_\perp} = \frac{1}{r}\frac{\partial}{\partial\theta}$. Using Eqs. (2.34) and (2.49) we find the entropic pressure on the surface of the wedge (still for $N \to \infty$),

$$P(r) = \frac{\pi}{4\alpha^2} \frac{k_B T}{r^2} \frac{1}{1 + (h/r)^{\pi/\alpha}} \ . \tag{2.50}$$

It is interesting to note the asymptotic behavior of the pressure for small r,

$$\lim_{r\to 0} P(r) \propto r^{\pi/\alpha - 2} \to \begin{cases} 0 & 0 < \alpha < \pi/2 \\ \text{const.} & \alpha = \pi/2 \\ \infty & \pi/2 < \alpha < \pi \end{cases} . \tag{2.51}$$

When the polymer is held outside the wedge ($\alpha > \pi/2$) the pressure on the tip diverges. This behavior can be seen In Figure 2.6, where we plot the pressure on the wedge for three different

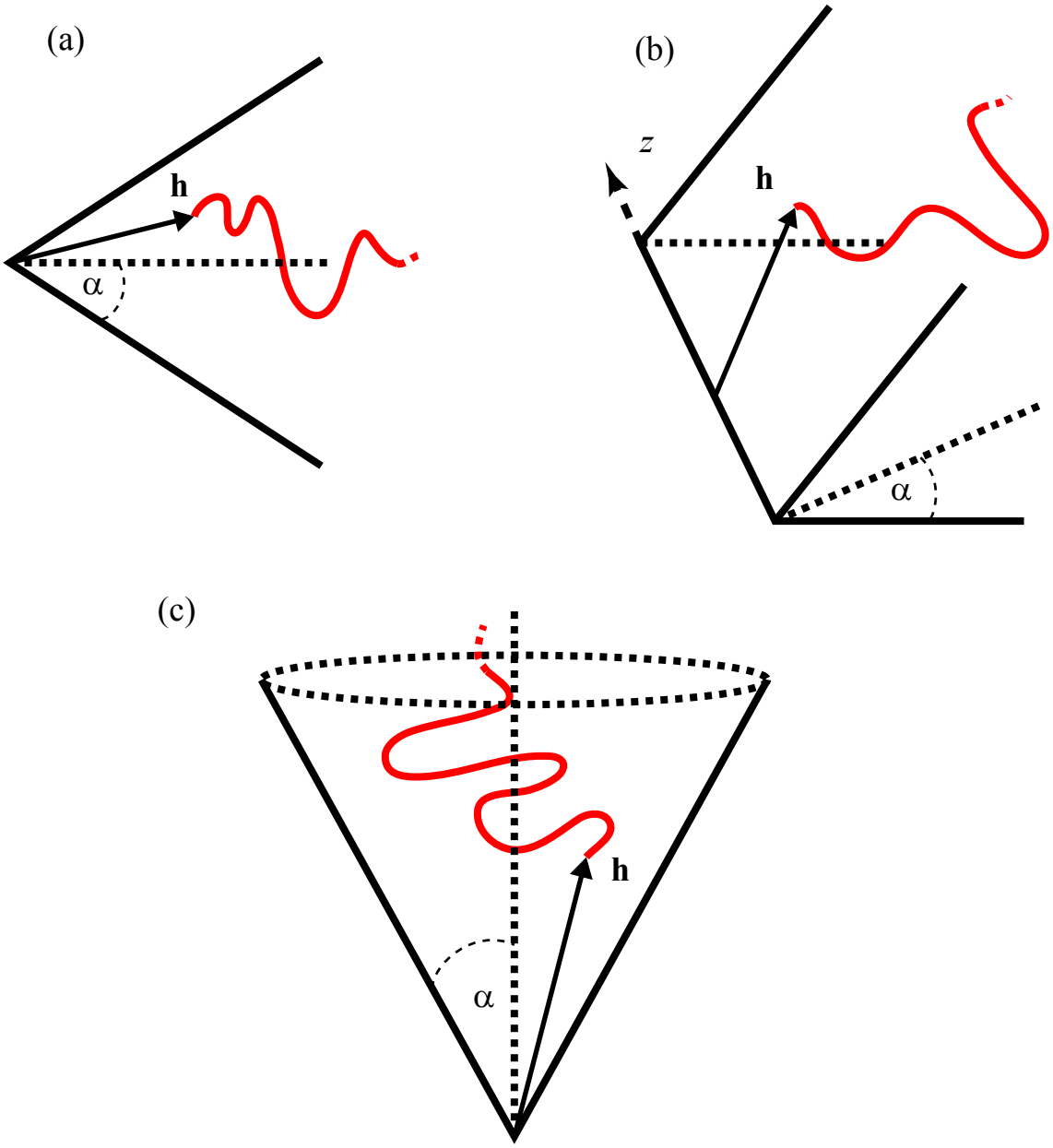

FIGURE 2.5: An ideal polymer confined to scale-free spaces: (a) wedge in $d = 2$, (b) wedge in $d = 3$, and (c) circular cone in $d = 3$.

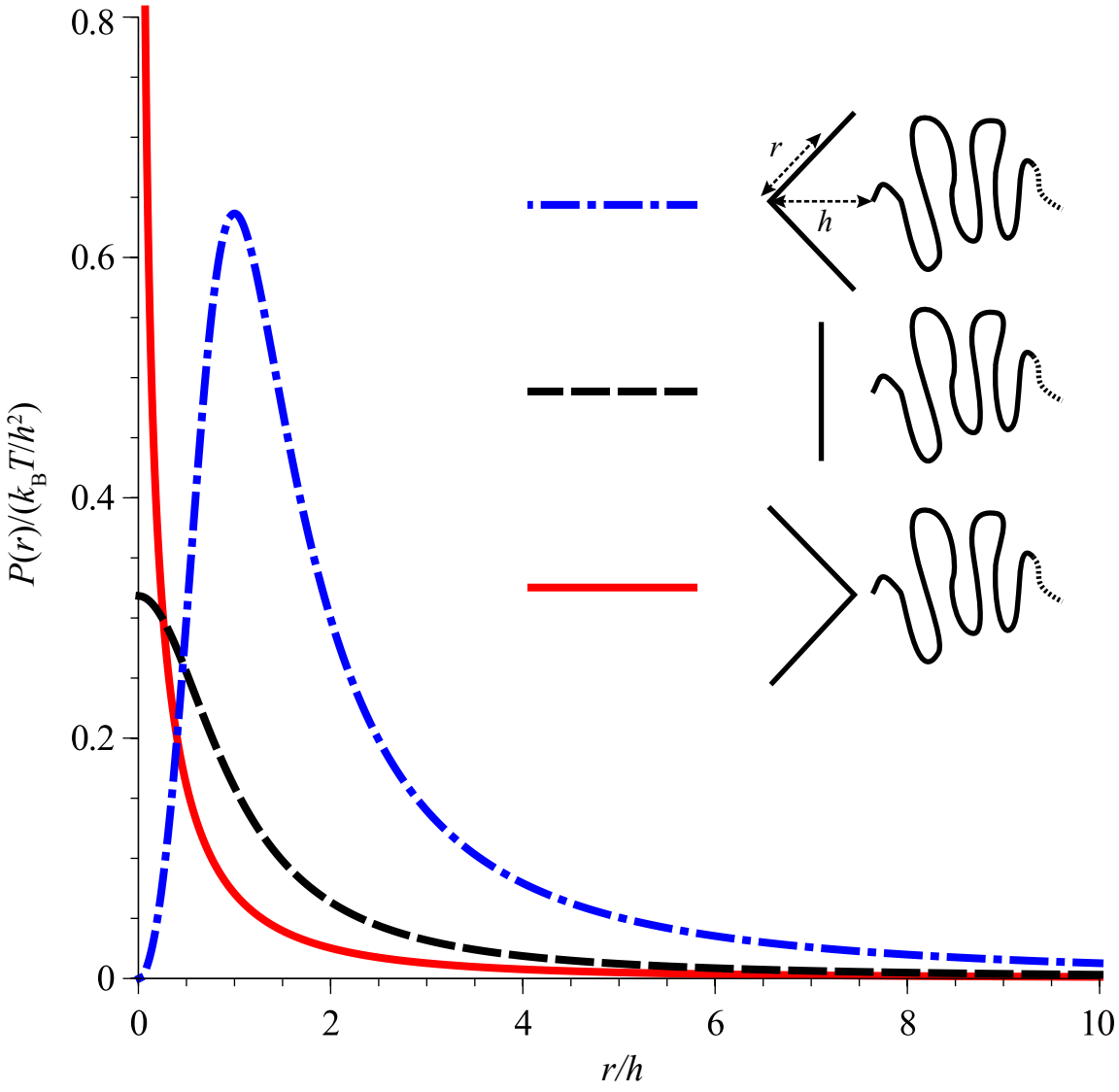

FIGURE 2.6: Scaled entropic pressure of a long IP on a wedge ($d = 2$) as a function of the scaled distance from the tip for three opening angles of the wedge, $\alpha = \pi/4$ (dot-dashed line), $\alpha = \pi$ (dashed line), $\alpha = 3\pi/4$ (solid line).

opening angles. The singularity at the tip of the wedge is similar (but not identical) to the one found in the electric field near the tip of a charged conductor. The analogy to electric fields is not surprising, since we have seen that the monomer density is related to the electrostatic potential of a point charge (Eq. (2.39)). The electric field near the tip of a conducting wedge scales as $r^{\pi/2\alpha-1}$ [59], whereas the polymer pressure scales as $r^{\pi/\alpha-2}$ (see Eq. (2.51)). For a flat plane ($\alpha = \pi/2$), both powers vanish.

2.3.2 Wedge in $d = 3$

The boundary of a wedge in 3-dimensional space is defined in cylindrical coordinates by $-\alpha < \theta < \alpha$ [Figure 2.5]. Consider a case where one end of the polymer is held at a distance h from the corner, along the symmetry axis of the wedge, at $z = 0$. The Green function for this geometry is given in Eq. (B.4). It is obtained by multiplying the Green function of the wedge in $d = 2$ by the $d = 1$ free space propagator. When $z^2 \ll DN$, the Green function is independent of z and when in addition $h^2 \ll DN$, $r^2 \lesssim DN$, it assumes the general form of Eq. (2.26). The force amplitude is the one found in $d = 2$ [Eq. (2.48)]. The monomer density in the wedge is found from Eq. (2.36), in the limit $N \to \infty$

$$\begin{aligned}\rho(r,\theta,z) &= \frac{1}{\pi^{1/2}D\alpha}\frac{(r/h)^{\pi/2\alpha}}{(r^2+h^2+z^2)^{1/2}}\cos\left(\frac{\pi\theta}{2\alpha}\right)\sum_{i=1}^{\infty}\Gamma\left(\frac{1}{2}+\frac{\pi i}{2\alpha}\right)\sin\left(\frac{\pi i}{2}\right)\cos\left(\frac{i\pi\theta}{2\alpha}\right)\times \\ &\left(\frac{rh}{r^2+h^2+z^2}\right)_2^{i\pi/2\alpha}\tilde{F}_1\left[\frac{1}{4}+\frac{i\pi}{4\alpha},\frac{3}{4}+\frac{i\pi}{4\alpha},1+\frac{i\pi}{2\alpha},\left(\frac{2rh}{r^2+h^2+z^2}\right)^2\right], \qquad (2.52)\end{aligned}$$

where ${}_2\tilde{F}_1$ is the regularized hypergeometric function. From Eq. (2.34), the pressure on the surface of the wedge is

$$\begin{aligned}P(r,z) &= \frac{k_BT\pi^{3/2}}{8\alpha^3}\frac{(r/h)^{\pi/2\alpha}}{r^2(r^2+h^2+z^2)^{1/2}}\sum_{i=1}^{\infty} i\sin\left(\frac{\pi i}{2}\right)\left(\frac{rh}{r^2+h^2+z^2}\right)^{\pi i/2\alpha}\Gamma\left(\frac{1}{2}+\frac{i\pi}{2\alpha}\right)\times \\ &{}_2\tilde{F}_1\left[\frac{1}{4}+\frac{i\pi}{4\alpha},\frac{3}{4}+\frac{i\pi}{4\alpha},1+\frac{i\pi}{2\alpha},\left(\frac{2rh}{r^2+h^2+z^2}\right)^2\right]. \qquad (2.53)\end{aligned}$$

Note that at the tip of the wedge we get the same irregular behavior that was encountered for $d = 2$, i.e. for $r \ll h$,

$$\lim_{r\to 0}P \propto \frac{r^{\pi/\alpha-2}}{(h^2+z^2)^{(\pi/\alpha+1)/2}}.$$

The unusual influence of the geometry of two- and three-dimensional wedges is known in the theory or critical phenomena and the remarkable effects of such geometries have been studied in detail [60] in the context of critical adsorption of liquids.

2.3.3 Circular Cone in $d = 3$

Now consider a cone defined in spherical coordinates by $\theta < \alpha$ [Figure 2.5(c)]. The polymer is confined to the cone with one end held at a distance h from the tip along the symmetry axis of the cone. The Green function for this geometry is given in Appendix B. Once more, it contains a sum which becomes a power series when $h^2 \ll DN$, $r^2 \lesssim DN$. As in the case of the wedge, in the limit $N \to \infty$ the first term in the series is dominant, and the Green function converges to the general form of Eq. (2.26). The force amplitude, η, is the lowest root of the equation

$$P_\eta(\cos\alpha) = 0, \tag{2.54}$$

where P_η is the Legendre function. Using the same method that was used for the other geometries to calculate the monomer density in the limit $N \to \infty$, we find

$$\begin{aligned}\rho(\mathbf{r}) = &-\frac{1}{2\pi D\sqrt{hr}} P_\eta(\mu)\left(\frac{r}{h}\right)^\eta \sum_{i=1}^{\infty}\left(\left[(1-\mu_0^2)\frac{\partial}{\partial\mu}P_{\eta_i}(\mu_0)\frac{\partial}{\partial\eta_i}P_{\eta_i}(\mu_0)\right]^{-1}\times\right.\\ &\left. P_{\eta_i}(\mu)\begin{cases}(r/h)^{\eta_i+1/2} & r<h\\ (h/r)^{\eta_i+1/2} & r>h\end{cases}\right),\end{aligned} \tag{2.55}$$

where η_i are the roots of Eq. (2.54), in ascending order, $\eta = \eta_1$, $\mu = \cos\theta$ and $\mu_0 = \cos\alpha$. The derivative in the direction perpendicular to the surface is the same as in the case of the wedge (with θ being the polar angle in spherical coordinates). The pressure on the surface is

$$P(r) = -\frac{k_B T}{2\pi r^3}\frac{\partial}{\partial\mu}P_\eta(\mu_0)\times\begin{cases}(\frac{r}{h})^{\eta+1}\sum_{i=1}^{\infty}\frac{(r/h)^{\eta_i}}{\frac{\partial}{\partial\eta_i}P_{\eta_i}(\mu_0)} & r<h\\ (\frac{r}{h})^{\eta}\sum_{i=1}^{\infty}\frac{(h/r)^{\eta_i}}{\frac{\partial}{\partial\eta_i}P_{\eta_i}(\mu_0)} & r>h,\end{cases} \tag{2.56}$$

Note that for $r \to 0$ we get $P \propto r^{2(\eta-1)}$. The singular asymptotic behavior of the pressure on the tip of the cone is similar to the one found on the wedge (Eq. (2.51)). It is also similar to the behavior of electric fields near the tip of a conducting cone, where the field scales as $r^{\eta-1}$. For a flat plane ($\alpha = \pi/2$, $\eta = 1$), the powers vanish. In fact, if we consider a point charge q held at height h above

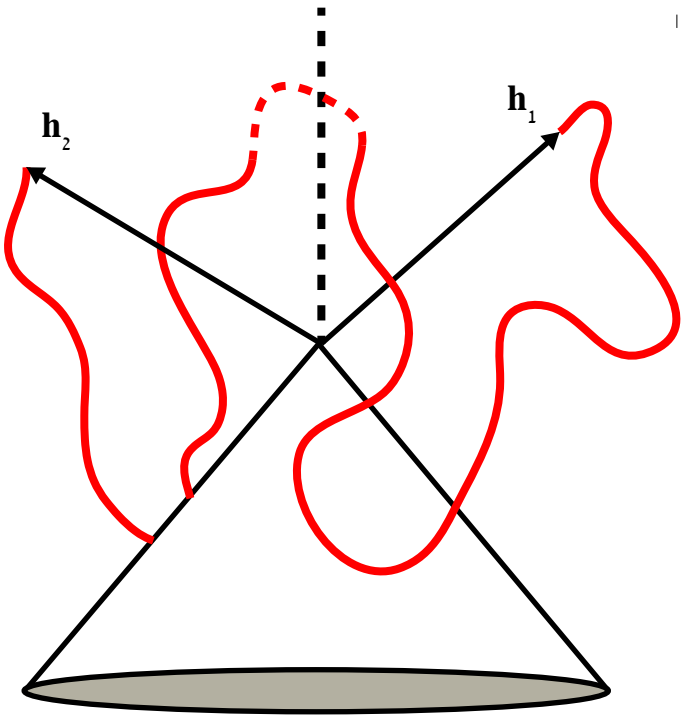

FIGURE 2.7: Ideal polymer with both ends held near a scale-free surface.

a grounded conducting plane, the electric field on the plane is identical with the polymer pressure on a flat plane if we replace $k_BT/2\pi$ by $2qh$.

2.3.4 Polymers held at both ends and ring polymers

Consider an IP held at *both* ends at points $\mathbf{h}_1$ and $\mathbf{h}_2$ close to scale-free surface as depicted in Figure 2.7. The monomer density at a point $\mathbf{r}$ in the allowed space is

$$\rho_N(\mathbf{h}_1,\mathbf{h}_2,\mathbf{r}) = \frac{\int_0^N G(\mathbf{h}_1,\mathbf{r},n)G(\mathbf{r},\mathbf{h}_2,N-n)dn}{G(\mathbf{h}_1,\mathbf{h}_2,N)}. \tag{2.57}$$

For large N, such that $h_1^2, h_2^2 \ll DN$, we can follow the same reasoning as in Section 2.2, and divide the integral $\int_0^N$ into *three* parts $\int_0^{n_1} + \int_{n_1}^{N-n_1} + \int_{N-n_1}^{N}$, where n_1 was chosen such that $h_1^2, h_2^2 \ll Dn_1 \ll DN$. (Note, that when the integration variable n is replaced by $N-n$ in the third integral, it becomes similar to the first integral with the roles of $\mathbf{h}_1$ and $\mathbf{h}_2$ reversed.) The first Green function in the integrand of Eq. (2.57) provides a significant contribution to the integral $\int_0^{n_1}$, while the second Green function is similarly significant in $\int_{N-n_1}^{N}$. Both functions are negligible in $\int_{n_1}^{N-n_1}$. In fact it can be shown that for fixed $x_1 = n_1/N$, in the $N \to \infty$ limit, the latter integral divided by $G(\mathbf{h}_1,\mathbf{h}_2,N)$ vanishes. In the range of the first integral ($n < n_1 \ll N$) we can

assume $G(\mathbf{r}, \mathbf{h}_2, N-n) \approx G(\mathbf{r}, \mathbf{h}_2, N)$ and take it out of the integration so that for large N the contribution of this integral to the density becomes $[G(\mathbf{r}, \mathbf{h}_2, N)/G(\mathbf{h}_1, \mathbf{h}_2, N)] \int_0^{x_1 N} G(\mathbf{h}_1, \mathbf{r}, n)dn$. For large N the ratio of the Green functions preceding the integral can be replaced by the ratio of $\tilde{G}$ functions defined in Eq. (2.21), which, by using Eq. (2.26) and the reciprocity relation (2.9), becomes $(r/h_1)^\eta[\Theta(\hat{\mathbf{r}})/\Theta(\hat{\mathbf{h}}_1)]$. Similar treatment, with the roles of $\mathbf{h}_1$ and $\mathbf{h}_2$ reversed, can be performed for the integral $\int_{(1-x_1)N}^{N}$. The results discussed above become exact in the $N \to \infty$ limit leading to

$$\rho(\mathbf{h}_1, \mathbf{h}_2, \mathbf{r}) = \left(\frac{r}{h_1}\right)^\eta \frac{\Theta(\hat{\mathbf{r}})}{\Theta(\hat{\mathbf{h}}_1)} \int_0^\infty G(\mathbf{h}_1, \mathbf{r}, n)dn + \left(\frac{r}{h_2}\right)^\eta \frac{\Theta(\hat{\mathbf{r}})}{\Theta(\hat{\mathbf{h}}_2)} \int_0^\infty G(\mathbf{h}_2, \mathbf{r}, n)dn. \tag{2.58}$$

By comparing this result with Eqs. (2.58) and (2.36), we see that the contribution from each end of the chain will be equal to the density calculated before for a polymer with one free end, i.e.,

$$\rho(\mathbf{h}_1, \mathbf{h}_2, \mathbf{r}) = \rho(\mathbf{h}_1, \mathbf{r}) + \rho(\mathbf{h}_2, \mathbf{r}), \tag{2.59}$$

where $\rho(\mathbf{h}_i, \mathbf{r})$ is the density which was calculated in Sections 2.2-2.3 with $\mathbf{h} = \mathbf{h}_i$. This result could be expected since the strands leaving the end-points $\mathbf{h}_1$ and $\mathbf{h}_2$ do not interact with each other, and the mid-section of the polymer is so far away, that the fact that this is a single polymer rather than two independent strands does not influence the density. From the relation between the monomer density and the pressure on the surface (Eq. (2.34)) we see that this additive correspondence between a pair of IP strands and a single polymer held by both ends will also apply to the pressure and the total force on the surface. This result can also be immediately applied to the density of infinite ring polymers:

$$\rho_{\text{ring}}(\mathbf{h}, \mathbf{r}) = \rho(\mathbf{h}, \mathbf{h}, \mathbf{r}) = 2\rho(\mathbf{h}, \mathbf{r}), \tag{2.60}$$

as well as to the pressure exerted by such polymers.

2.4 Summary and conclusions

In Chapter 1 it was shown that the force between a polymer and a scale-free surface can be written in terms of universal exponents, which depend on the geometry of the surface and the nature of the interactions between the monomers, but are independent of the microscopic details of the system. In this Chapter we have shown that the universal exponent η also plays an important role in the

monomer density and the pressure of IPs on scale-free surfaces. Additional calculations were needed to completely describe the pressure and the density, but η controlled the behavior at very short distances. We found the general form of the Green function $\tilde{G}$ (Eq. (2.26)) for long IPs. By using the simple connection between the exponent η and the mean end-to-end distance of the polymer R_e (Eq. (2.28)), one can measure η by solving the diffusion equation numerically or extracting R_e from simulations.

In Section 2.2 we showed that the monomer density and the entropic pressure can be derived from the electrostatic potential of a point charge in a confined space. It was also shown that the density possesses some powerful scaling properties that enable one to map the density and the pressure from points near the origin to points far away, and vice versa. The relation to electrostatics also enabled the use of a formalism resembling Gauss' law in electrostatics, to relate the total force to the pressure distribution.

Our calculations were limited to IPs. While they provide some guidance to understanding polymers in good solvents, several important differences exist. The presence of repulsion between monomers modifies both exponent ν and η. The basic expression (2.12) cannot be used in its simplest form to calculate the density because the probability of a polymer reaching point $\mathbf{r}$ in n steps is influenced by the presence of the remaining $N - n$ steps, and proper adjustments need to be made. Even in free space the distribution of the the end-to-end distance of self-avoiding polymers is significantly more complicated (see Chapter 4 and references therein) than the Green function of ideal polymers. Thus, we cannot expect such simple behaviors as exhibited by $\tilde{G}$ in (2.26). In Chapter 4, we will use numeric simulations to study the end-point distribution of SAWs near impenetrable wedges and cones, analogous to the Green function studied here, and see if some of the results obtained here for IPs can be carried over to polymers in good solvent.

The properties of the monomer density discussed in Subsection 2.3.4 indicate that the results in this Chapter can be applied to entropic systems where both ends of the polymer are attached to scale-free surfaces. This may provide a pathway to dealing with polymers attached by both ends to different surfaces, such as a polymer with one end grafted to an AFM tip and the other to a flat substrate. In good solvents expressions like (2.59) and (2.60) are obviously incorrect. However, like in IPs, we expect that for very long polymer the behavior of two ends of a polymer will be the same as that of two (interacting) polymers with their remote ends completely free.

Chapter 3

Entropic Pressure in Lattice Models for Polymers[1]

In the previous Chapter we derived the entropic pressure of a long IP on a SF repulsive surface. IP statistics are observed in Θ-solvents, where the interaction with the solvent molecules cancel the steric repulsion between the monomers [22]. The more general case of polymers with steric interaction is difficult to treat analytically, and often numeric simulations are used [62].

Lattice models for polymers are very useful since they capture exactly all the universal features of the molecules and are simple to implement on a computer. However, when defining local properties like the pressure on a point on a surface, it is best to make sure that the lattice definitions are consistent with the definitions in the continuous models.

In this Chapter we discuss the definitions of entropic forces and pressure in lattice models and show that the usual definition of the pressure must be modified in order to be consistent with the pressure in continuus models, and so that the integration of the pressure over the surface will amount to the total force acting on it.

3.1 Pressure in continuous and discrete systems

3.1.1 Continuous systems

In mechanical systems the pressure is a scalar quantity related to the diagonal elements of the stress tensor [63], and in simple homogeneous isotropic equilibrium systems, such as fluids, it is the main property characterizing the system [64]. In non-homogeneous systems in equilibrium, it is often convenient to consider *local* stresses inside the system, where they characterize momentum transfer,

[1] The work presented in this chapter was published in [61].

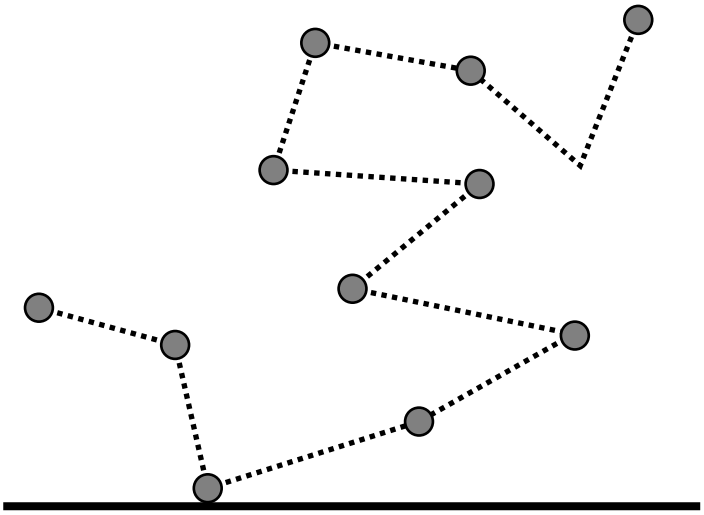

FIGURE 3.1: A polymer composed of hard spheres (circles) connected by springs (dashed lines) near the wall of a large box (solid line). Even though there are several monomers in the polymer, only one is in contact with the wall.

both kinetic momentum and the interaction forces between particles. (See [65, 66] and references therein.) From a kinetic point of view, when classical particles are confined by smooth rigid surfaces (walls), they undergo specular reflections from the walls, leading to a force locally perpendicular to the walls. The average of this force per unit area is the local pressure

$$P(\vec{x}) = k_B T \rho(\vec{x}), \tag{3.1}$$

where k_B is the Boltzmann constant and T is the temperature, while $\rho(\vec{x})$ is the mean local density of particles in contact with the wall at position $\vec{x}$. This ideal-gas-like local expression is unaffected by the interactions between the particles, and relies solely on the 'hard' interaction between each particle and the wall, where the potential changes from 0 to ∞. In statistical mechanics $P(\vec{x})$ is the *ensemble averaged* force per unit area acting on the boundary. In the canonical ensemble such local force is the derivative of the free energy of the system with respect to a local displacement of the boundary perpendicular to itself [14, 54, 46]. This is the pressure that was calculated in Section 2.2.

Consider a single polymer modeled as a chain of $N + 1$ hard spheres connected by N springs (Figure 3.1), placed in a box with flat hard walls. The probability of finding a monomer within a small distance ϵ from the boundary is linear in ϵ, while the probability of finding *two* monomers is proportional to ϵ^2. Thus, when the wall is shifted by an infinitesimal distance, only one monomer

makes contact with the wall and the polymer touches the wall at a single point. The local nature of the pressure is reflected in Eq. (3.1), where the pressure depends on the monomer density at a specific point $\vec{x}$. Note that this density is affected by the interaction between the monomers in the polymer.

The 'beads and springs' model is a *discrete* model defined in a *continuous* space. If we take the $N \to \infty$ limit and at the same time take all the microscopic length scales to zero (the radius of the spheres and the average length of the springs), so that the average end-to-end distance R of the polymer remains finite, we arrive at a *continuous* polymer model [67] like the one considered in Chapter 2. When we place a continuous polymer near a repulsive wall, the density of monomers on the wall vanishes. The entropic pressure of the polymer on the wall at the point $\vec{x}$ is determined by the rate of change of the monomer density close to $\vec{x}$ in the direction perpendicular to the wall [46, 54, 68]. In the above models, which are defined in continuous space, the total force is found by integrating the pressure over the surface, i.e.,

$$\vec{F} = \int P d\vec{S}, \tag{3.2}$$

where $d\vec{S}$ is a vector whose size is that of a surface element, and it is perpendicular to the wall.

3.1.2 Discrete systems

Using lattice models in polymer simulations allows qualitative treatment of universal features of larger systems at the expense of quantitative agreement with real systems [69]. In what follows, we propose a method to recover some of this quantitative agreement. In lattice systems the statistical mechanics approach to the local pressure is reduced to the calculation of discrete changes of the system [70, 71, 72, 55]. Consider a RW or a SAW on a lattice confined to a large box. The walk is allowed to visit the sites on the walls of the box but not to cross them. The force F acting on one flat wall is found by calculating the change in the free energy of the system $\Delta\mathcal{F}$ that results from excluding all the sites along the wall, thus moving the wall by a finite distance Δh, i.e.,

$$F\Delta h = \Delta\mathcal{F}. \tag{3.3}$$

If the wall is a plane (in space dimension $d = 3$) or a line (in $d = 2$) and it is shifted along one of the axes of a hypercubic lattice, as in Figure 3.2(a), Δh is simply the lattice constant a. Similarly, it

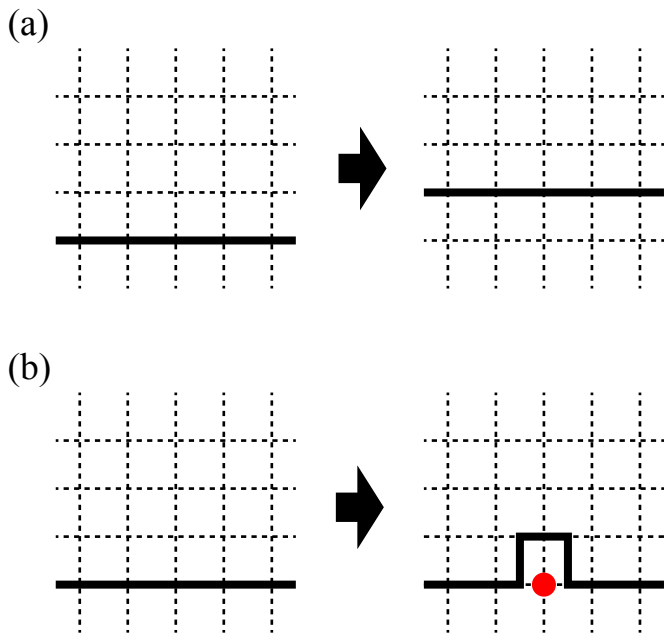

FIGURE 3.2: Discrete changes on a square lattice. (a) The wall is shifted by one lattice constant. (b) The lattice site marked by the red circle is excluded.

is natural to derive the pressure from the change $\Delta\mathcal{F}(\vec{x})$ in the free energy of the system resulting from the exclusion of a lattice site $\vec{x}$,

$$P_d(\vec{x})\Delta h\Delta S = \Delta\mathcal{F}(\vec{x}), \tag{3.4}$$

where ΔS is the surface element associated with the site $\vec{x}$. The subscript d in Eq. (3.4) stands for *discrete*. In what follows we will compare the lattice pressure P_d to the pressure P computed in the continuous case in Chapter 2. In the simple example depicted in Figure 3.2(b), ΔS is the lattice constant, and $\Delta S\Delta h = a^2$.

Unlike in polymer models in continuous space, in the lattice polymer models there can be more than one monomer in contact with the wall (Figure 3.3). More than one site along the wall can be occupied, and in the case of a RW more than one monomer can occupy a single site. For this reason, Eq. (3.2) does not hold in the lattice model, i.e., [55]

$$\vec{F} \neq \int P_d d\vec{S}. \tag{3.5}$$

Thus the local pressure defined in this way is not a good representation of what we mean by pressure in continuous systems. We seek to correct this situation, and define a local pressure in a discrete

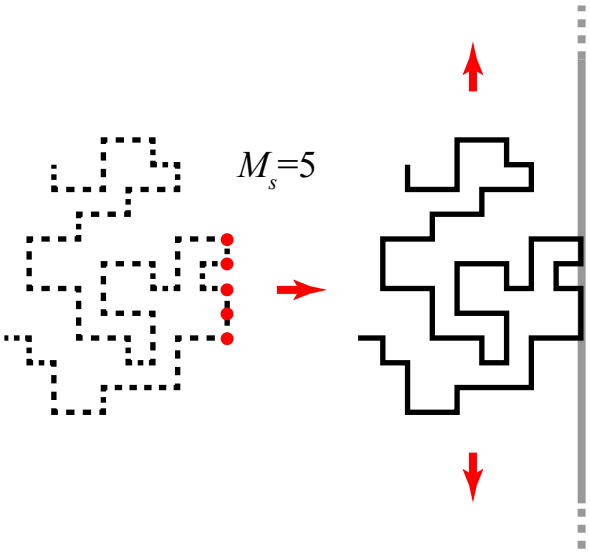

FIGURE 3.3: A SAW on a square lattice brought into contact with the wall of a large box. The system is symmetric to translations along the wall. The walk touches the wall at $M_s = 5$ different sites.

system that is numerically as close as possible to the pressure measured in continuous systems and results in the correct total force after integration.

3.2 General formalism for lattice polymer problems

Consider a polymer modelled as a RW or SAW of N steps on a hypercubic lattice confined to a certain region of space. We study the pressure and the total force on one of the walls of the allowed region. The configurational part of the free energy of the system is

$$\mathcal{F} = -k_B T \ln \mathcal{N}_t, \tag{3.6}$$

where $\mathcal{N}_t$ is the total number of allowed configurations. We denote by $\mathcal{N}_c$ the number of configurations in which the polymer touches the wall at least at one site. When the wall is moved by one lattice constant the total number of available configurations is reduced by $\mathcal{N}_c$, so that the change in the free energy of the system is

$$\Delta\mathcal{F} = -k_B T \ln\left(1 - \frac{\mathcal{N}_c}{\mathcal{N}_t}\right). \tag{3.7}$$

It is convenient to define a dimensionless force variable $\hat{F} \equiv \mathcal{N}_c/\mathcal{N}_t$, so that the total force on the wall is

$$F = -\frac{k_B T}{\Delta h} \ln\left(1 - \hat{F}\right). \tag{3.8}$$

Frequently, $\hat{F} \ll 1$ and we can expand Eq. (3.8) and see that $\hat{F}$ is indeed proportional to the total force, i.e., $F \approx (k_B T/\Delta h)\hat{F}$. We repeat this process with respect to the change in the free energy of the system $\Delta\mathcal{F}(\vec{x})$ associated with the exclusion of the lattice site $\vec{x}$ from the available sites for the walk. If we denote by $\mathcal{N}_{\vec{x}}$ the number of walks that touched the surface at the point $\vec{x}$ at least once, we arrive at

$$P_d(\vec{x}) = -\frac{k_B T}{\Delta h \Delta S} \ln\left(1 - \hat{P}(\vec{x})\right), \tag{3.9}$$

where the dimensionless pressure $\hat{P}(\vec{x}) \equiv \mathcal{N}_{\vec{x}}/\mathcal{N}_t$ [54, 72, 71, 73]. Practically always $\hat{P}(\vec{x}) \ll 1$, and we can expand Eq. (3.9) to get $P_d(\vec{x}) \approx (k_B T/\Delta h \Delta S)\hat{P}(\vec{x})$.

3.3 Force and pressure of a lattice polymer in a large box

When the polymer is confined to a large box (the size of the box is much larger than the average size of the polymer) the system can be regarded as homogeneous, and to a good approximation, invariant with respect to translations along the wall. In this case the relation between the pressure and the total force can be derived from the analysis of lattice polymers in free space (no boundaries). Any configuration in free space can be created by taking a walk s starting from the origin and moving it as a rigid unit to a new position $\vec{x}_0$ (Figure 3.3). Thus each walk w is identified by its shape s_w and its starting position $\vec{x}_{0,w}$. Suppose we wish to study the pressure and force between walks in a large box, and one of the walls which is defined by $x_i = 0$, where x_i is the i spatial coordinate in the system. For each shape s we can identify $x_{i,\min}$, the minimal value of x_i along the walk, and define M_s to be the number of different minimal sites of the walk in the direction of i (Figure 3.3). When a walk w is in contact with the wall, i.e., $x_{i,\min} = 0$, it touches the wall at precisely M_{s_w} sites. Note that this is independent of the starting position of the walk along the wall, and only depends on its shape. Due to the symmetry of the system with respect to translations parallel to the large wall, the number of configurations in which the polymer is in contact with the wall is

$$\mathcal{N}_{\text{con}} = \mathcal{N}_s \cdot \mathcal{N}_b, \tag{3.10}$$

where $\mathcal{N}_s$ denotes the number of shapes the polymer can take [for a RW on a d-dimensional hypercubic lattice $\mathcal{N}_s = (2d)^N$] and $\mathcal{N}_b$ is the number of sites on the wall. The number of configurations that touched the wall at a certain site $\vec{x}$ at least once is independent of $\vec{x}$ due to the same translational symmetry, and can be expressed as

$$\mathcal{N}_{\vec{x}} = \sum_s M_s. \tag{3.11}$$

From Eqs. (3.10), (3.11) and the definition of $\hat{P}$ and $\hat{F}$ we arrive at

$$\sum_{\vec{x}} \hat{P}(\vec{x}) = \frac{\mathcal{N}_b}{\mathcal{N}_t} \sum_s M_s = \hat{F} \frac{1}{\mathcal{N}_s} \sum_s M_s = \langle M \rangle \hat{F}.$$

We see that when the polymer is moving freely in a large box, the ratio between the total force and the integral of the pressure on the surface of the wall is equal to the average $\langle M \rangle$ taken over possible shapes of the walk. It is interesting to note that this average can be measured without the presence of the confining box, and it is in fact a property of polymers in free space. The technique of using walks in free space to study properties of walks in the presence of boundaries is sometimes referred to as CABS (confinement analysis from bulk structure), and has been discussed and used in several recent works [74, 75]. By numerically examining a RWs of $N = 10^5$ steps on a square lattice we find $\langle M \rangle \approx 2.78$. Thus, for RWs on a square lattice, when the walk moves freely in a large confining box with a flat wall of surface S, then the pressure on the wall and the total force F acting on it are related by $P_d S = 2.78F$. In fact, as will be discussed later, even in more complicated, non-homogeneous systems, it is often sufficient to divide the pressure by the constant $\langle M \rangle$ computed in free space.

3.4 Force and pressure of a lattice polymer in a non-homogeneous case

We now examine the relation between the local pressure and the total force applied on the wall for a non-homogeneous system. Consider, for example, a lattice polymer anchored at a site $\vec{x}_0$ near an infinite wall [Figure. 3.4(a)]. The polymer is confined to the half space defined by the wall. As before, it can visit the sites on the boundary but is not allowed to cross it. Let us denote by w a certain configuration of the polymer that *visited* the boundary wall. Also, let us define a variable $m_w(\vec{x})$ that is equal to one if the walk w visited the site $\vec{x}$ on the wall, and zero otherwise (so that $\sum_{\vec{x}} m_w(\vec{x}) = M_w$, where $M_w = M_{s_w}$ defined above). The total number of walks that visited the

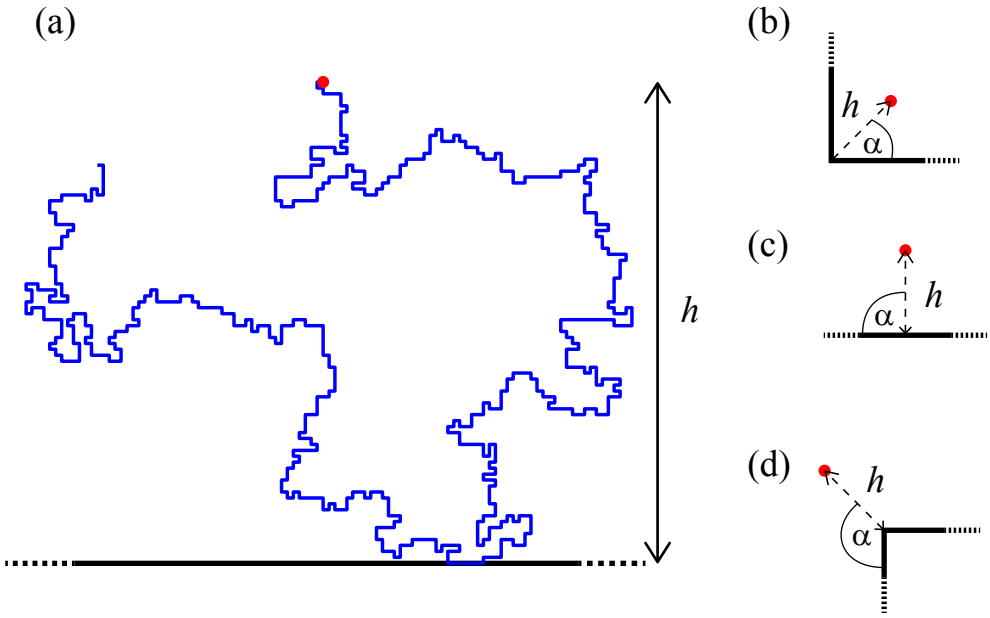

FIGURE 3.4: (a) A SAW on a square lattice in contact with a boundary line. The starting position of the walk (red circle) is at a distance h from the line. (b)-(d) The geometries considered in the force and pressure measurements of section 3.5 are sectors with different opening angles α.

wall can be written as a sum over the configurations w that touched the wall, i.e,

$$\mathcal{N}_{\text{con}} = \sum_{w} 1 = \sum_{w} \sum_{\vec{x}} \frac{m_w(\vec{x})}{M_w}. \tag{3.12}$$

Combining Eq. (3.12) with the definitions of $\hat{F}$ and $\hat{P}$, we find that

$$\hat{F} \;=\; \frac{1}{\mathcal{N}_t} \sum_{\vec{x}} \sum_{w} \frac{m_w(\vec{x})}{M_w} = \sum_{\vec{x}} \frac{\mathcal{N}_{\vec{x}}}{\mathcal{N}_t} \frac{1}{\mathcal{N}_{\vec{x}}} \sum_{w_{\vec{x}}} \frac{m_{w_{\vec{x}}}(\vec{x})}{M_{w_{\vec{x}}}} = \sum_{\vec{x}} \hat{P}(\vec{x}) \left\langle M^{-1} \right\rangle_{\vec{x}},$$

where $w_{\vec{x}}$ is a configuration that touched the point $\vec{x}$ on the wall. We denote by $\langle\rangle_{\vec{x}}$ a *conditional* average with respect to only the walks that visited the site $\vec{x}$. Note that the switch from summation over w to the summation over $w_{\vec{x}}$ in Eq. (3.13) is justified since for any walk w that did not visit the site $\vec{x}$ we will have $m_w(\vec{x}) = 0$ and it will not contribute to the sum. We see from Eq. (3.13) that it is possible to define a *modified* dimensionless pressure

$$\bar{P}(\vec{x}) = \hat{P}(\vec{x}) \langle M^{-1} \rangle_{\vec{x}}, \tag{3.13}$$

that, when integrated on the boundary wall, will result in the total force acting on the wall.

The modified definition of the entropic pressure was derived for a *single* polymer near a boundary wall. It is straight forward to generalize $\bar{P}$ to a system with multiple polymers. In the latter case w would represent a specific configuration of *all* molecules in the system in which at least one monomer contacts the surface and M_w would denote the number of different sites on the surface occupied in w. The remainder of the derivation would not be affected.

In the next section, we study the properties of this correction and check whether the modified pressure recovers the local pressure computed in Chapter 2 for ideal polymers in SF spaces.

3.5 Case in point – polymers on a square lattice near a confining line or sector

We studied numerically the pressure and the force between a RW or a SAW on a square lattice starting from a site $\vec{x}_0$ near a confining boundary. For the geometry of the boundary, three cases discussed in Chapter 2 were considered: an infinite line [Figure 3.4(a),(c)], a sector of opening angle $\alpha = \pi/4$ [Figure 3.4(b)] and a sector of opening angle $\alpha = 3\pi/4$ [Figure 3.4(d)]. The starting position of the polymer was taken to be on the symmetry axis of the sector (irrelevant for the infinite line) at a distance h from the boundary.

3.5.1 Entropic force measurement

In Chapter 1, we mentioned that for continuous polymers in the limit where the typical linear size of the polymer $R \to \infty$ the entropic force between the polymer and the surface is of the form

$$F = \mathcal{A}\frac{k_B T}{h}, \tag{3.14}$$

where the force amplitude $\mathcal{A}$ is a universal constant, i.e., it depends on a small number of parameters such as the dimension of the system, the opening angle of the sector and the presence of steric repulsion between monomers. Specifically,

$$\mathcal{A} = \eta_b - \eta_f, \tag{3.15}$$

where η is the critical exponent that characterizes the anomalous decay of correlations between monomers [76]. We denote by η_f the value of this exponent for a polymer in free space (no boundary) and by η_b the value of η for a polymer anchored to the boundary, i.e., anchored to the confining

line or to the tip of the confining sector. In Chapter 2, we showed that for RWs in, $\eta_f = 0$, whereas for RWs in $d = 2$ confined to sectors, $\eta_b = \pi/2\alpha$, leading to

$$\mathcal{A}_{\mathrm{RW}} = \frac{\pi}{2\alpha}. \tag{3.16}$$

Cardy and Redner [77] found the critical exponents for long SAWs confined to sectors in $d = 2$ using conformal mapping. We will discuss their results in more detail in Chapter 4. For now, we use their calculation of the critical exponents to state that

$$\mathcal{A}_{\mathrm{SAW}} = \frac{15 - 5\alpha/\pi}{48\alpha/\pi}. \tag{3.17}$$

In Section 1.3 we have seen that the force amplitude can also be expressed as $\mathcal{A} = \Delta\gamma/\nu$, where $\Delta\gamma$ is the difference in the critical exponent γ between a polymer in free space and one anchored to the boundary. The change in γ correspond to the change in the entropy of the system when the boundary is introduced, which is greater for RWs since more configurations are excluded. (For a comparison of $\Delta\gamma_{\mathrm{RW}}$ and $\Delta\gamma_{\mathrm{SAW}}$ see Figure 4.3 in the next chapter.) In the same time, the exponent ν is greater for SAWs than for RWs, as they are more extended in space. Thus, the force amplitude is influenced by competing effects. From Eqs. (3.16) and (3.17) it is evident that the greater entropy change prevails so that $\mathcal{A}_{\mathrm{RW}} > \mathcal{A}_{\mathrm{SAW}}$.

In order to demonstrate a measurement of the entropic force, we generated a large number ($\sim 10^7$) of RWs of 10^5 steps on a square lattice, each starting at a distance h from a boundary line or sector as described above. Walks that crossed the boundary were discarded, and among the walks that remained within the allowed space, we counted how many visited the sites on the boundary, thus measuring the ratio $\hat{F} = \mathcal{N}_c/\mathcal{N}_t$. The entropic force is then given by Eq. (3.8). The measurement was performed in a similar way for SAWs, where walks of 512 steps were generated using dimerization [62]. The results are presented in Figure 3.5. The form in Eq. (3.15) for the force is valid only when the distance h from the wall is much greater than any microscopic length scale such as the lattice constant. This is clearly not the case for some of the data presented in Figure 3.5. It has been shown in several works, that to first order, the affect of the microscopic length scale can be taken into account by adding a constant shift δ to the distance h [78, 79, 80, 81]. For this

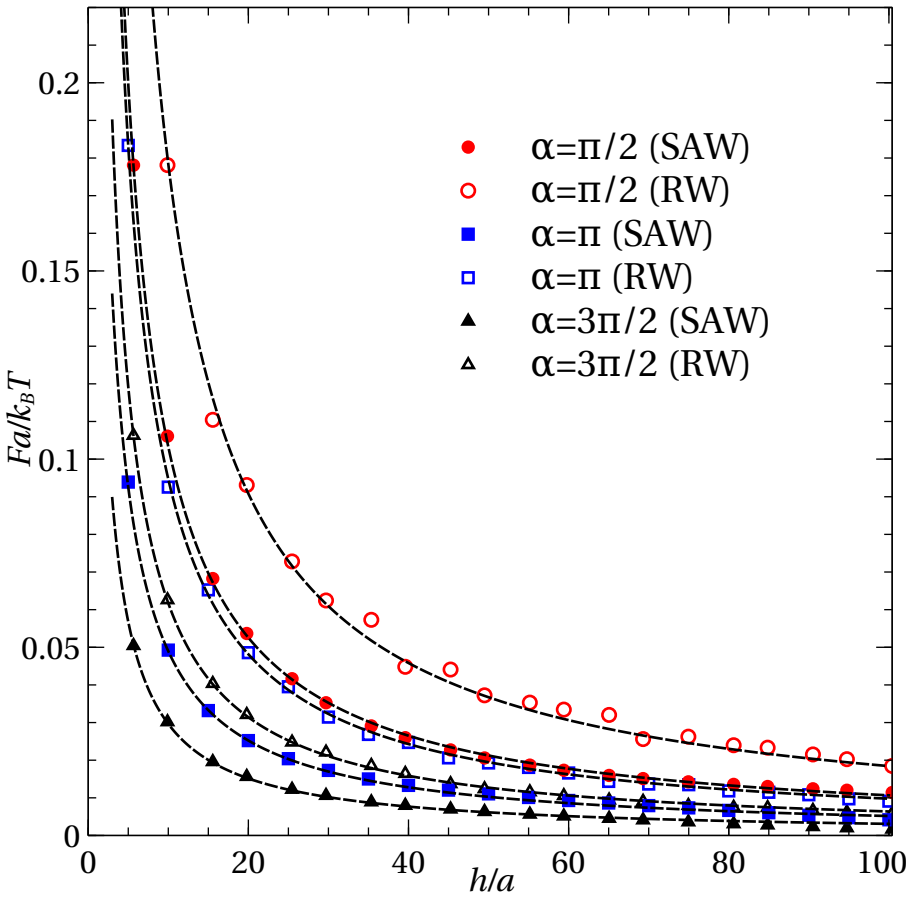

FIGURE 3.5: Entropic force between a RW of 10^5 steps or a SAW of 512 steps on a square lattice and a scale invariant boundary, shown as a function of the distance h between the starting position of the walk and the boundary in lattice units a. The shape of the boundary is a sector with different opening angles α (see legend). The data were fitted to the form in Eq. (3.18) (dashed lines).

reason, we fitted the force measurement data to a function of the form

$$\frac{F(h)}{k_B T} = \frac{\mathcal{A}}{h+\delta}, \tag{3.18}$$

where the force amplitude $\mathcal{A}$ and the shift δ are the fitting parameters. In Table 3.1 we see that the force amplitudes extracted from the measurements are in good agreement with the exact values [Eqs. (3.16) and (3.17)] for $\alpha = 3\pi/4$ and $\alpha = \pi/2$. There are noticeable discrepancies between the theoretical and the measured values when the polymer is confined inside a sector with $\alpha = \pi/4$, where the polymer is closest to the walls and we can expect that the small length scale will be most significant. Another reason for these discrepancies is the fact that the theoretical force amplitudes were computed for infinitely long polymers, while our walks are finite. The finiteness of the walks leads to a reduction of the force. (see discussion for a finite walk near a line in the next section).

	RW		SAW	
α	theory	numerics	theory	numerics
$\pi/4$	2	1.85 ± 0.06	1.15	1.07 ± 0.02
$\pi/2$	1	0.97 ± 0.02	0.52	0.52 ± 0.02
$3\pi/4$	2/3	0.64 ± 0.02	0.31	0.31 ± 0.02

TABLE 3.1: Force amplitudes for RWs of 10^5 steps and SAWs of 512 steps on a square lattice anchored near an infinite boundary in the shape of a sector with opening angle α. Theoretical values for the infinitely long continuous walks are compared with the numerical values extracted from Figure 3.5. The errors represent 95% confidence limits. We did not attempt to estimate systematic errors.

3.5.2 Entropic pressure measurement

Using the same set of configurations generated for the force calculation, we measured the dimensionless pressure $\hat{P}(x) = \mathcal{N}_x/\mathcal{N}_t$, and the corrected pressure $\bar{P}(x) = \hat{P}(x)\langle M^{-1}\rangle_x$, where x is the distance from the tip of the sector (for the infinite line the starting position of the polymer is directly above the point where $x = 0$). We compare these measurements with the exact results obtained in Chapter 2, where the entropic pressure P was found for a continuous infinitely long ideal polymer, held at one end near a scale invariant repulsive sector [Eq. (2.50)].

In Figure 3.6 we present the dimensionless pressure $\hat{P}$ [Figure 3.6(a)] and the corrected pressure $\bar{P}$ [Figure 3.6(b)] for a random walk confined to a sector. It can be seen that $\bar{P}$ is in much better agreement with P [Eq. (2.50)] than $\hat{P}$. For the majority of values of x/a depicted in Figure 3.6, the modification factor $\langle M^{-1}\rangle_x$ is almost constant (see the discussion in the next subsection). We could, therefore, obtain very similar results by dividing the reduced pressure by the constant $\langle M\rangle$ found in section 3.3. For these simple surfaces, it is not clear from the data that the more complicated procedure we suggest here of calculating $\langle M^{-1}\rangle_x$ at each point individually is preferable to simple division of the pressure by a constant. However, the modified pressure is guaranteed to result in the correct total force upon integration on *any* surface, including more complicated ones that are not homogeneous.

A close inspection of the graph reveals that there is still a systematic discrepancy between $\bar{P}$ and P. The measured pressure $\bar{P}$ is slightly larger than the theoretical pressure P. The reason is that our walks are finite. In order to demonstrate this, we used the methods described in Chapter 2 to calculate the pressure of a *finite* continuous ideal polymer in two dimensions anchored at a

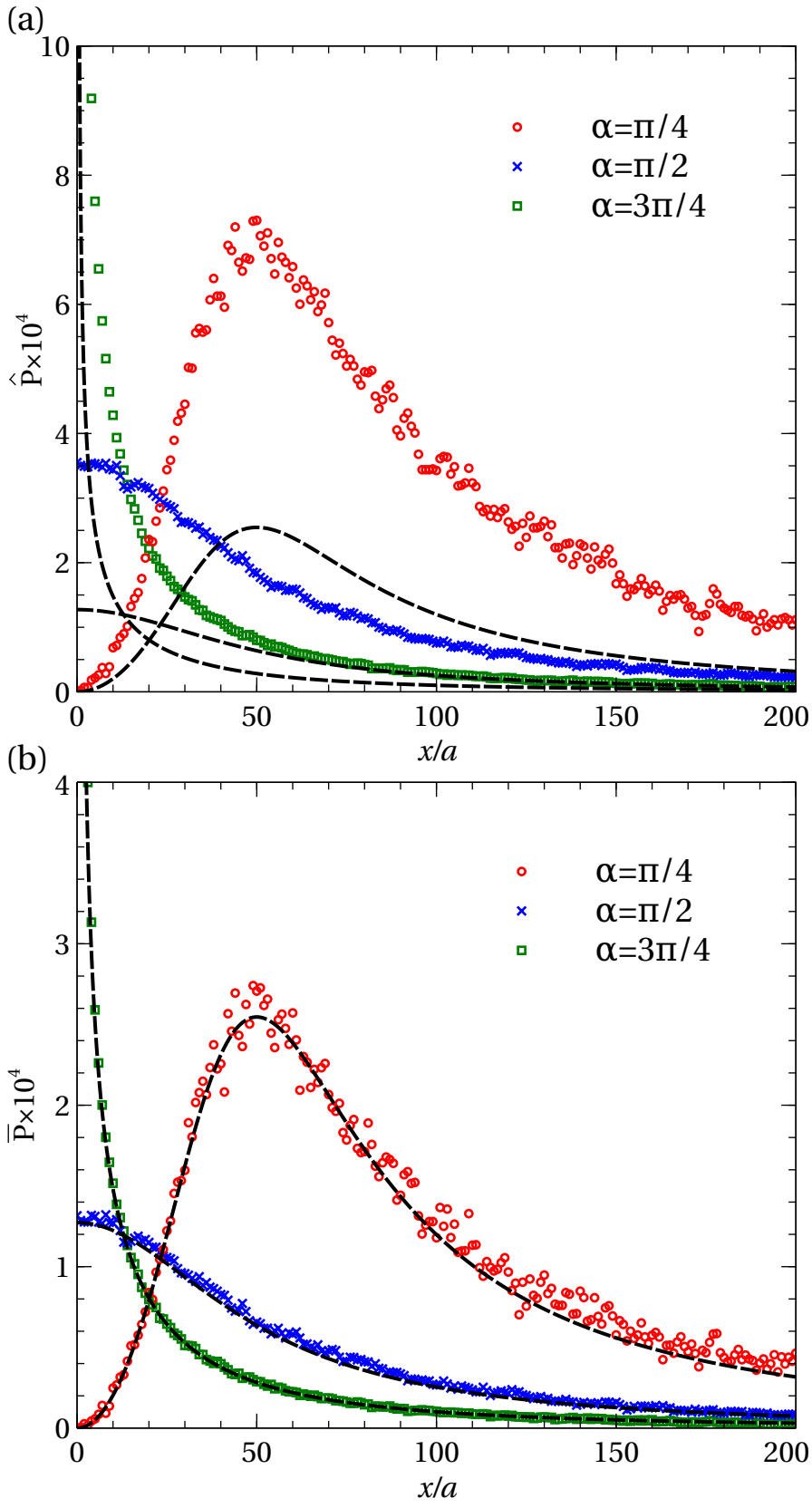

FIGURE 3.6: Entropic pressure of a RW of 10^5 steps on a square lattice anchored approximately at a distance of 50 lattice constants ($h = 50a$) from a scale invariant boundary. (a) The dimensionless pressure $\hat{P}$. (b) The modified dimensionless pressure $\bar{P}$. The dashed lines denote the exact pressure of an infinite continuous ideal polymer [Eq. (2.50)]. Note the different scale in the vertical axis.

distance h near an infinite boundary line (a sector where $\alpha = \pi/2$),

$$P(x,R) = 2k_BT\frac{h}{R^3}\frac{G^{2,0}_{1,2}\left(\frac{h^2+x^2}{R^2}\middle|\begin{matrix}-\frac{1}{2}\\ -1,0\end{matrix}\right)}{\pi\,\mathrm{erf}(h/R)}, \tag{3.19}$$

where $R = Na^2$, $G^{2,0}_{1,2}$ is the Meijer function [82] and erf is the error function. In Fig. 3.7 we show $\bar{P}$ measured for RWs of $N = 10^4$ and 10^5 steps. The results are in excellent agreement with Eq. 3.19. The dependence of the pressure on the size of the polymer is also seen in the figure. For smaller polymers, the pressure at small x is larger in comparison with the infinite polymer limit, but when x approaches the size of the polymer the pressure is cut off exponentially. The fact that finite polymers apply more pressure near the anchor point of the polymer than infinite polymers can be understood when we consider the probability that a section of the polymer will return to the boundary and collide with it. When a segment of the RW wanders to the vicinity of the boundary wall, it increases the risk that the following segments of the walk will cross the wall, which results in discarding the walk from the statistics (similarly to the absorbance of a Brownian particle). The free end of the walk, which is present in finite polymers, can approach the boundary more easily since it has no following segments.

The exact total force of a finite continuous polymer on the line can be found by integrating Eq. 3.19. We find that the force applied by a finite walk, F_{finite}, approaches the infinite limit F_{infinite} from below. For $R \gg h$, the leading correction $F_{\text{finite}} - F_{\text{infinite}} \sim 1/R$.

3.6 Properties of the correction to the pressure

We would like to understand whether the reduction factor $\langle M^{-1}\rangle_{\vec{x}}$ applied to the pressure is a *local* parameter, i.e., it results from the statistics of the system in the vicinity of $\vec{x}$, or rather it depends on long range correlations of the polymer. To achieve this, we note that it can be written in the following way,

$$\langle M^{-1}\rangle_{\vec{x}} = \left\langle \frac{1}{1+\sum_{\vec{x}'\neq\vec{x}} m(\vec{x}')} \right\rangle_{\vec{x}}. \tag{3.20}$$

From Eq. (3.20) we see that the other sites on the boundary affect the correction to the pressure at the site $\vec{x}$ through the conditional function $\langle m(\vec{x}')\rangle_{\vec{x}}$. If this function decays rapidly as the distance $|\vec{x}-\vec{x}'|$ increases (say exponentially), then we could say that the modification of the pressure is local, and depends only on contacts made by the walk in the vicinity of the site $\vec{x}$. In the case

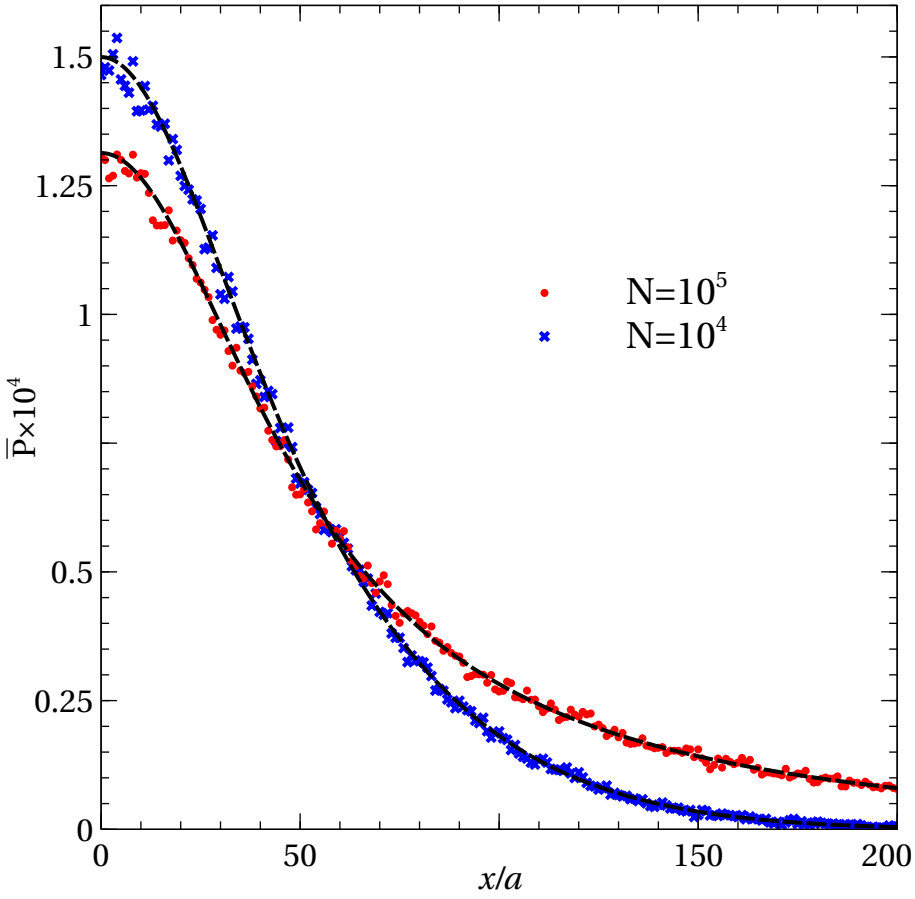

FIGURE 3.7: Entropic pressure of a finite RW on a square lattice of N steps, anchored at a distance of 50 lattice constants ($h = 50a$) from a boundary line. The dashed lines denote the exact pressure given by Eq. (3.19).

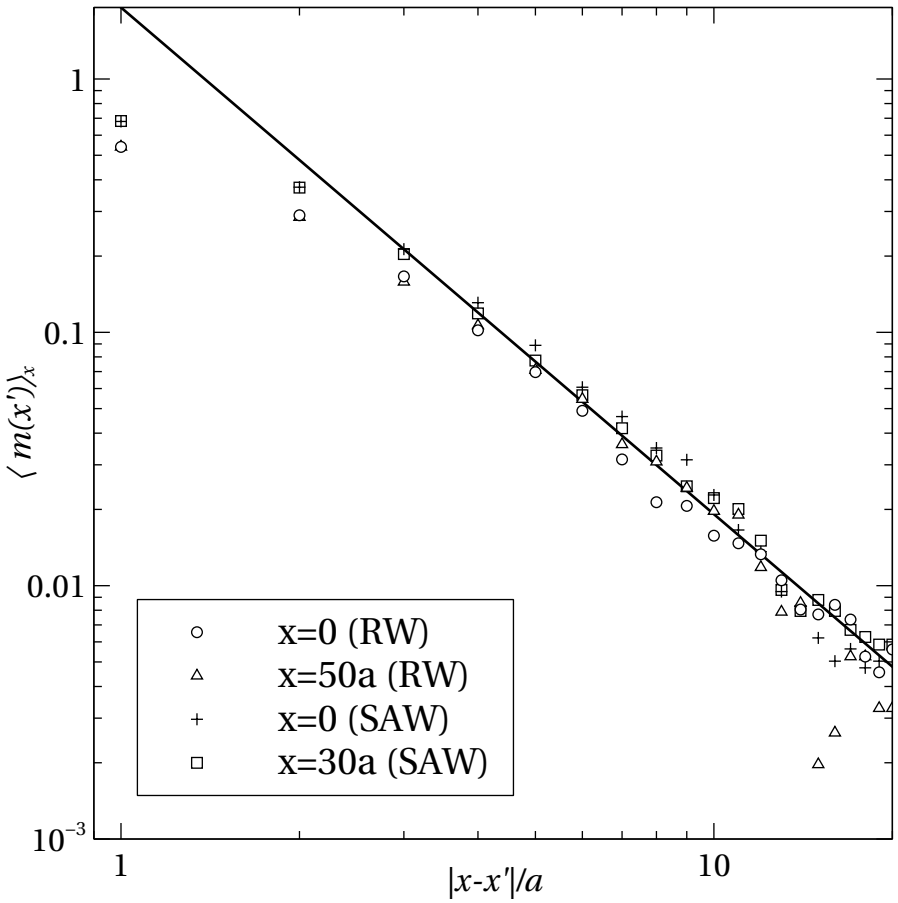

FIGURE 3.8: The conditional function $\langle m(x') \rangle_x$ versus the distance $|x - x'|$ between the sites, taken for RWs of $N = 10^5$ steps and SAWs of $N = 512$ steps on a square lattice. The starting position of the RWs was 50 lattice constants above a repulsive boundary line and for the SAWs it was 30 lattice constants above the line. Apart from the first two points, the density decays as $|x - x'|^{-2}$ (solid line). The conditional density is the same for $x = 0$ (circles and plus signs) directly beneath the starting position and for $x = 50a$ or $x = 30a$ (triangles and squares), even though the systems are not homogeneous.

of RWs and SAWs on a square lattice confined to a sector, we find that $\langle m(x') \rangle_x$ is not a local function, but decays as a power of $|x' - x|^{-2}$ [Figure 3.8]. In fact, it is possible to show that for a RW in d dimensions that touches a $(d-1)$-dimensional boundary plane at a point $\vec{x}$, the function $\langle m(\vec{x}') \rangle_{\vec{x}}$ decays as $|\vec{x} - \vec{x}'|^{-d}$. For SAWs on a square lattice, there seems to be a similar behaviour. This observation leads us to say that in the 2-dimensional case, the correction we found to the entropic pressure is *non-local*. This property of the entropic pressure in a lattice system makes it fundamentally different from the pressure in continuous systems, discussed in section 3.1. In lattice systems, the idea of a pure local pressure which results in the total force on the surface after integration is no longer valid, since the correction $\langle M^{-1} \rangle_{\vec{x}}$ contains important long range contributions.

Another interesting question is whether the reduction factor applied to the pressure is constant or does it vary with position along the boundary (like the pressure). In Figure 3.9 we plot $\langle M^{-1}\rangle_{\vec{x}}$ for a RW anchored at a distance $h = 50a$ from the sector, and a SAW anchored at a distance $h = 30a$ from the sector. Several observations can be made. First, for a walk anchored in the vicinity of an infinite line ($\alpha = \pi/2$), $\langle M^{-1}\rangle_{\vec{x}}$ appears to be constant, i.e., independent of x and equal to the factor found in the homogeneous case (section 3.3). Thus we see that when the walk starts at a distance much greater than the lattice constant, the modification we propose to the entropic pressure is independent of the starting position of the walk. In this case the correction is reduced to a multiplicative factor which depends on a small number of parameters such as the type of lattice, the dimension of the system and the universality class of the walks (e.g. RWs versus SAWs). However, from Figure 3.9 we also see that $\langle M^{-1}\rangle_{\vec{x}}$ does depend on the shape of the surface, and varies when we approach the tip of the sector. For $\alpha = 3\pi/4$, when the polymer is held outside of a $\pi/2$ sector (i.e., inside of a $3\pi/4$ sector), $\langle M^{-1}\rangle_{\vec{x}}$ increases near the corner, whereas for $\alpha = \pi/4$, when the polymer is confined inside the $\pi/4$ sector, $\langle M^{-1}\rangle_{\vec{x}}$ decays to zero at the corner. Note that the pressure behaves in a similar way [Figure 3.6]. The behaviour of $\langle M^{-1}\rangle_{\vec{x}}$ near the corners can be understood qualitatively in the following way: When the polymer makes contact with the surface in an area that is increasingly confined (e.g. close to the corner when $\alpha = \pi/4$), we can expect that more contacts were made on the surface in nearby points since the polymer has fewer options to escape into the bulk. Thus, the total number of contacts with the surface, M, will be larger for these configurations, and the factor $\langle M^{-1}\rangle_{\vec{x}}$ will be smaller. Note that in this case it is harder for the polymer to reach the confined area and therefore the entropic pressure will also be reduced in the vicinity of the corner. On the other hand, when the area in question is less confined, as in the vicinity of the corner with $\alpha = 3\pi/4$, the polymer can reach it more easily, and can more easily escape into the bulk after making contact with the surface, thus making a smaller number of contacts with the boundary. Therefore, for $\alpha = 3\pi/4$, the pressure and $\langle M^{-1}\rangle_{\vec{x}}$ are both increased in the vicinity of the corner.

3.7 Summary and conclusions

Polymers on lattices are often used to study properties of polymers in continuous space, even though there are important differences in the definition and behavior of physical properties in lattice and continuous systems. When dealing with macroscopic quantities such as the force acting on a large

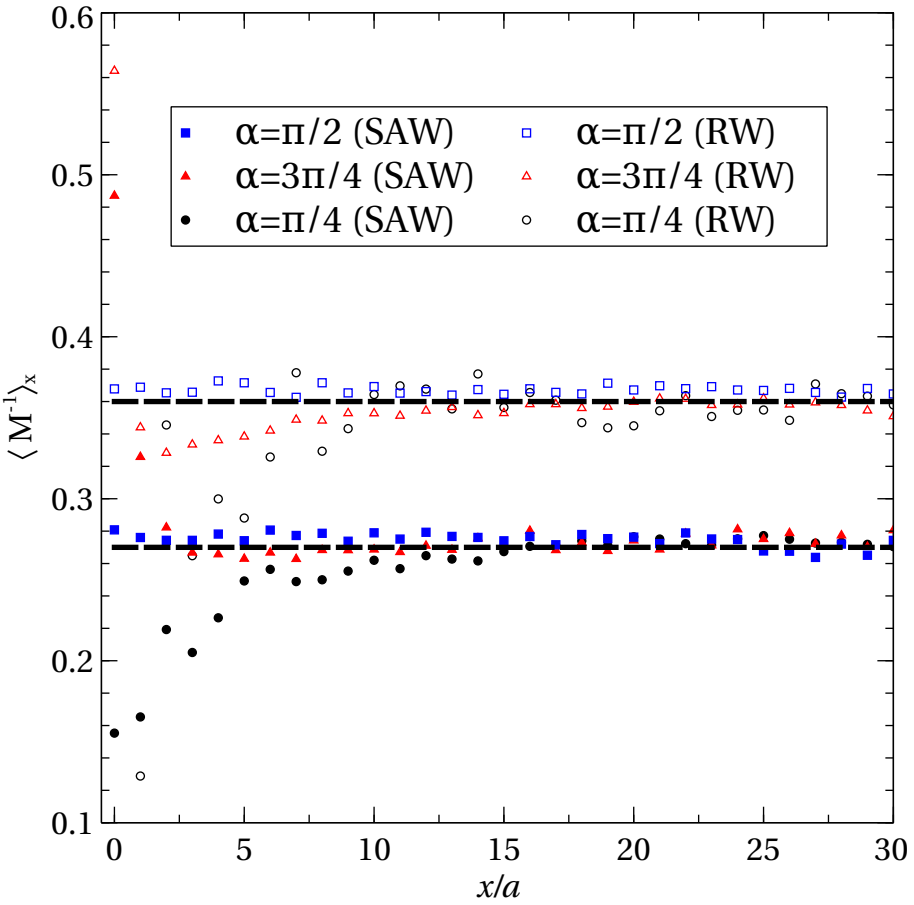

FIGURE 3.9: The correction factor $\langle M^{-1}\rangle_x$ measured for RWs of 10^5 steps and SAWs of 512 steps on a square lattice anchored near a confining sector. The RWs were anchored approximately at a distance $h = 50a$ from the tip of the sector and the SAWs were anchored at a distance of approximately $h = 30a$ from the tip of the sector [see Figure 3.4]. For the case of a boundary line (sector with opening angle π) the correction factor is homogeneous (squares). For a sector with $\alpha = \pi/4$ (circles) the correction decays to zero when the corner is approached (as do the pressure in this case). For a sector with opening angle $\alpha = 3\pi/4$ (triangles), the correction factor increases near the tip (as does the pressure).

object, the results in the lattice systems match those in continuous space. However, this is not always the case when dealing with local properties such as the entropic pressure on a boundary surface. The natural way to define the pressure $P(\vec{x})$ at the point $\vec{x}$ along the boundary in a lattice system is as the change in the free energy of the system which results from excluding the point $\vec{x}$, divided by the volume element related to $\vec{x}$. However, this definition of the pressure is inadequate when we want to use the lattice polymer models to represent polymers in continuous space, where an important requirement is that when the pressure is integrated over the entire surface, the result should be the total force F acting on the surface. It is known [55] that $P(\vec{x})$ defined above does not satisfy this condition.

For a polymer in a large box, where the pressure on the wall is constant, we show that the difference between the integral of the pressure and the total force is a constant factor that can be calculated from the statistics of polymers in free space. Thus in this case this surface effect is in fact a bulk property [74, 75], that depends on a small number of parameters such as the type of lattice and the universality class of the lattice polymer (e.g. RWs versus SAWs).

For non-homogeneous cases, we define a modified entropic pressure, denoted $\bar{P}$ in dimensionless units, that, upon integration, *does* result in the correct total force acting on the surface. Even though in many cases, when the surface geometry is simple, it is sufficient to divide the lattice pressure by a constant value as mentioned above, our modified pressure is guaranteed to result in the correct total force after integration even on more complicated boundaries. Note that the total force matches the one measured in continuous space. Also, computing our modified pressure in simulations does not require significant numerical effort.

We show that our modified pressure calculated for RWs on a square lattice near scale invariant repulsive boundaries matches the exact results obtained for continuous polymers in this geometry, and use this system to study the properties of the proposed modification. We show that it is *non-local*, i.e., it depends on long range correlations between contact points along the surface. We conclude that the entropic pressure of a lattice polymer cannot be considered as a purely local property that results in the total force after integration, like the pressure in the continuous systems.

Chapter 4

Simulations of Random and Self-Avoiding Walks Near Wedges and Cones[1]

In this Chapter we study numerically long RWs and SAWs attached to the corner of an impenetrable wedge in two dimensions ($d = 2$), or the tip of an impenetrable cone in $d = 3$, of sizes ranging up to $N = 10^6$ steps. We study the critical exponent γ_α that determines the behavior of the number of configurations $\mathcal{N}_\alpha$ of a walk attached to the tip of an impenetrable cone/wedge with opening angle α, (see Figure 4.1), according to

$$\mathcal{N}_\alpha \propto N^{\gamma_\alpha - 1}. \tag{4.1}$$

Also, we study the end-point distribution of the walks and check if the results obtained for RWs in Chapter 2 can be carried over to SAWs. The case of $d = 2$ is of particular theoretical interest since in that geometry there is an analytical estimate for the value of the wedge exponent γ_α for SAWs [77], as well as for the end-point distribution of the walks. We show that the values obtained for γ_α are in agreement with the theory, while the predictions for the end-point distribution are not consistent with the simulation results. We discuss the possible reasons for this discrepancy. The work presented in this Chapter was published in [83].

4.1 Efficient implementation of the pivot algorithm

Monte Carlo simulations face a challenge to generate large ensembles. The pivot algorithm [84, 85, 86, 2, 26] is a dynamic method which generates SAWs with fixed N and free end-points. In each

[1] The work presented in this chapter was published in [83].

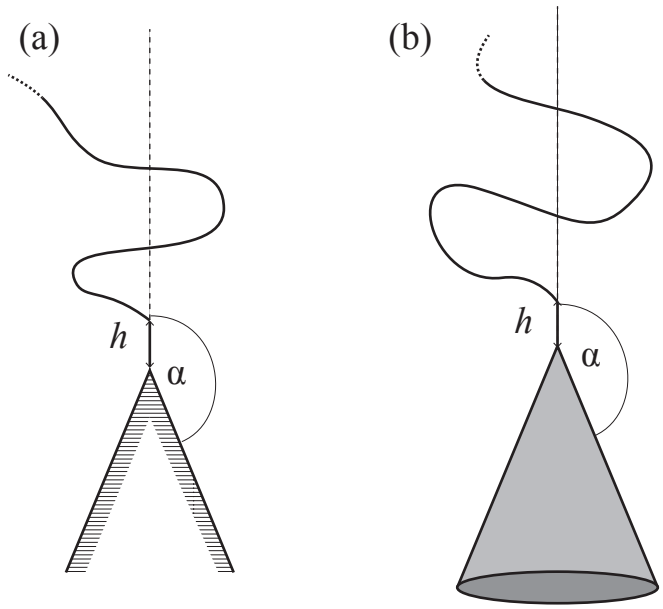

FIGURE 4.1: Geometries considered in this Chapter. (a) A two-dimensional wedge with opening angle α. (b) A three-dimensional cone with opening angle α.

time step a random site along the walk is used as a pivot point for a random symmetry action on the lattice (e.g., rotation or reflection) to be applied to the part of the walk subsequent to the pivot point. The resulting walk is accepted if it is self-avoiding; otherwise, it is rejected and the old walk is sampled again. The pivot algorithm is most efficient when studying large scale properties of the polymers such as R^2 [23]. Still, the bottleneck in the algorithm was always the self-avoidance tests, which required $O(N^x)$ operations ($x \approx 1$).

Recently, Clisby [2, 26] introduced a new data structure called a SAW tree that allows for a faster implementation of the pivot algorithm. An N-site SAW is represented by a binary tree [87]. The N leafs of the tree are individual sites of the walk, while each of the $N-1$ internal nodes represents a section of the walk. Each internal node contains aggregate information about the section of the walk that it represents, such as the bounding box of the section, which is a convex shape that completely contains it. Each node also contains a symmetry operation. The walk corresponding to a SAW tree is constructed in a recursive procedure starting from the root and moving down the tree. At each step, the symmetry operation stored in the node is performed on the right child, and then the left and right children are concatenated. Clisby also defined a set of rotation operations [87] that can change the structure of the tree while not changing the SAW it represents. A pivot move can be implemented by selecting a node and changing the symmetry operation it contains, after using rotations to bring it to the root of the tree. In order to check for intersections between

sections of the walk, one can recursively check for intersections between bounding boxes of left and right children in the tree. Clisby showed that on average, a remarkably low number of intersection tests is needed, and a test for self-intersection can be done in at most $O(\log N)$ time. As mentioned in [26], the SAW tree can be used to perform fast intersection tests with surfaces. This is done by recursively checking for intersections between the bounding boxes of left and right trees and a boundary surface. In this work, we implemented such intersection tests for wedges and cones which also take no longer than $O(\log N)$ time to perform. Note that while the self-intersection tests are used to accept or reject pivot moves, in the simulations described in this Chapter, the intersection tests of walks and surfaces are used only to decide whether to include the walks in the statistics of a particular geometry. The improved implementation of the pivot algorithm enables the study of SAWs in confined spaces of sizes that were not accessible to simulations in the past. For a more detailed description of the SAW tree and its use see Chapter 5 and [2].

4.2 Measurement of the exponent γ_α

In order to study the behavior of the exponent γ_α, we measured the probability $p_\alpha(N)$ of successfully moving a lattice walk with N steps that was generated in free space to the vicinity of an excluded wedge/cone with opening angle α (without changing its shape). This probability is equal to the fraction of walks that, starting near the tip of the cone/wedge, do not intersect with the boundary. From Eqs. (1.7) and (4.1),

$$p_\alpha(N) = \frac{\mathcal{N}_\alpha}{\mathcal{N}_\mathrm{f}} \propto N^{-\Delta\gamma_\alpha}, \tag{4.2}$$

where $\Delta\gamma_\alpha = \gamma_\mathrm{f} - \gamma_\alpha$.

We used the pivot algorithm to generate at least 2×10^6 SAWs in free space with $N = 10^5$ to 10^6, where sequential samples were separated by 10^3 pivot attempts. Each simulation began with an initialization of the SAW in order to avoid any systematical errors due to its initial configuration. Madras and Sokal [85] estimated that it is sufficient to discard the first $20N/f$ time steps in the simulation, where f is the acceptance rate of the pivot moves. Given that the lowest acceptance rate in our simulation was $f \sim 0.07$ (for SAWs on the square lattice with $N = 10^6$) we found it sufficient to discard the first $500N$ time steps in all configurations studied in this work. We selected the pivot points uniformly from the sites along the walk. Note that it is possible to obtain better accuracy or reduce the simulation time and retain the same accuracy by using non-uniform selection of the pivot sites along the walk, thus reducing the autocorrelation time for the samples in the simulation

α/π	$\Delta\gamma_\alpha$	α/π	$\Delta\gamma_\alpha$
5/16	0.973 ± 0.049	11/16	0.2588 ± 0.0058
3/8	0.743 ± 0.036	3/4	0.207 ± 0.004
7/16	0.602 ± 0.019	13/16	0.162 ± 0.0034
1/2	0.482 ± 0.011	7/8	0.12 ± 0.002
9/16	0.39 ± 0.012	15/16	0.0793 ± 0.0014
5/8	0.3175 ± 0.0083	1	0.0005 ± 0.0031

TABLE 4.1: Difference in the critical exponents $\gamma_{\rm f} - \gamma_\alpha$ measured for SAWs in $d = 3$ confined to a cone with opening angle α [red circles in Fig. 4.3(a)].

[88]. Also, as an alternative to sampling the walk only once in 10^3 pivot attempt, it is possible to use batch means [89], in which case there are some subtleties regarding our use of subsets of the time series (For example, sub-series must be batched up separately). These improvements of the simulation were used in the work described in Chapter 5.

In every sample the walk was tested for intersection with a wedge/cone with various opening angles α, placed so that the starting position of the walk is ten lattice units from the tip. We measured the probability $p_\alpha(N)$ that the walk will not intersect with the boundary and the distribution of the end-point of the walk (used in Sec. 4.4). Note that the pivot attempts were performed in *free* space and, when studying the end-point distribution of a SAW in a particular wedge/cone, only those samples in which the walk did not intersect with the surface were considered. Since the pivot algorithm in free space is ergodic, all samples in the generated ensemble are taken into account with the same statistical weight. The same is true for a subset of this ensemble where the walks do not intersect a certain boundary.

In order to verify the validity of our method, we repeated the simulation for RWs, this time accepting any pivot attempt, without checking for self-avoidance, and compared our data with known theoretical result (see Chapter 2 and [46, 19]). Note that Eqs. (1.7) and (4.1) are valid in the asymptotic limit $N \to \infty$ and, in principle, we should consider finite size corrections (For example $\mathcal{N}_{\rm f} \propto N^{\gamma_{\rm f}-1}\mu^N\left(1 + O(N^{-\Delta})\right)$, where $\Delta \approx 0.52$ [90] in $d = 3$). However, since the smallest N in this simulation is 10^5, we find that finite size corrections are negligible compared to the errors due to the statistical scattering of the data.

In Figure. 4.2 we present, in logarithmic scales, the success probabilities as a function of the size of the walk, for SAWs in $d = 2$ and $d = 3$. The linear dependence is clearly observed. The absolute values of the slopes of the linear fits shown in Figure 4.2 represent the difference in the critical exponents, $\Delta\gamma_\alpha$, and they are presented in Figure 4.3 (red circles). A similar analysis

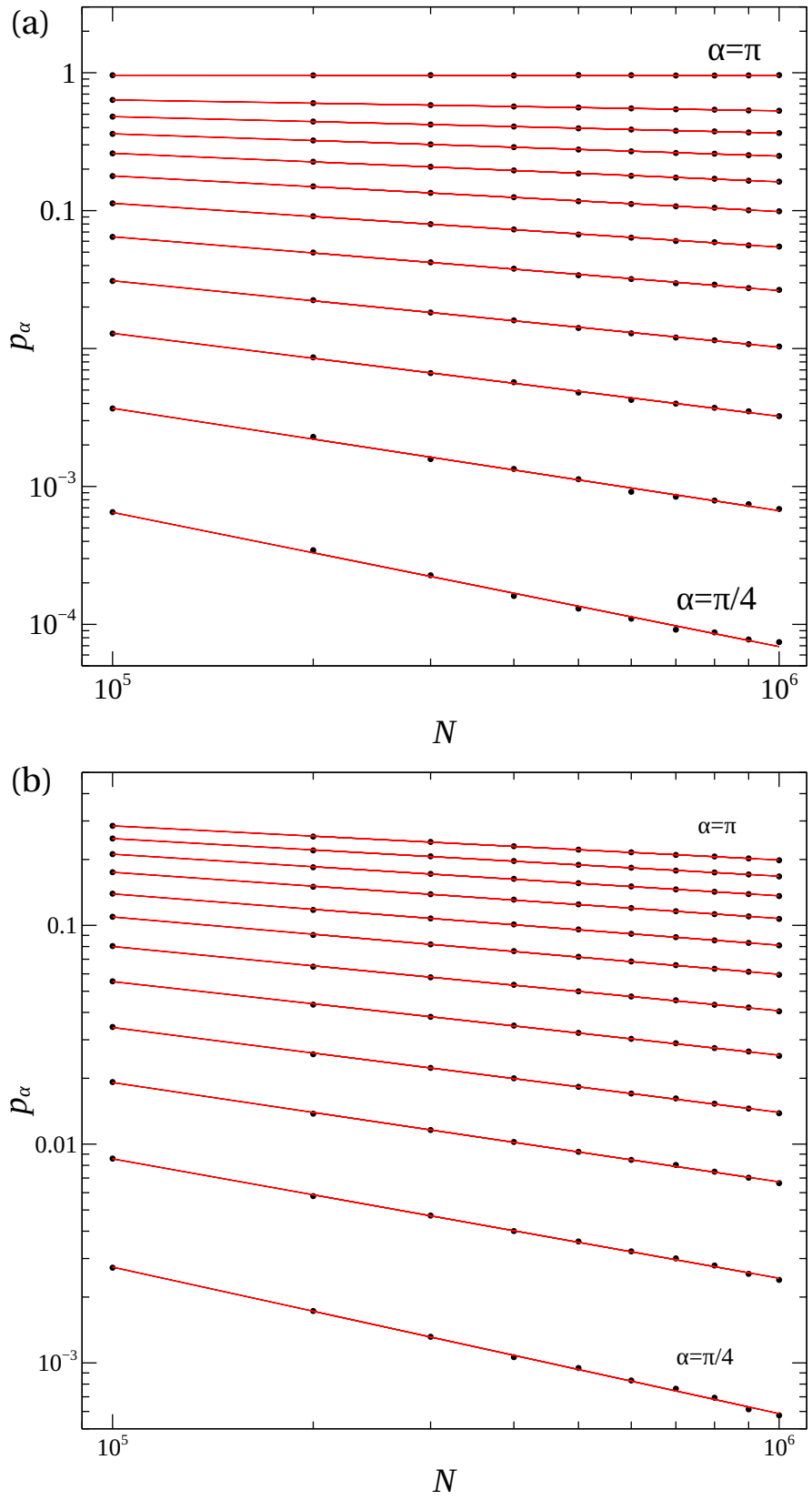

FIGURE 4.2: Success probabilities p_α for the confinement of SAWs of size N in a three-dimensional cone (a) or a two-dimensional wedge (b) with different opening angles $\alpha = j\pi/16$, $j = 4, 5, ..., 16$. The continuous lines are linear fits.

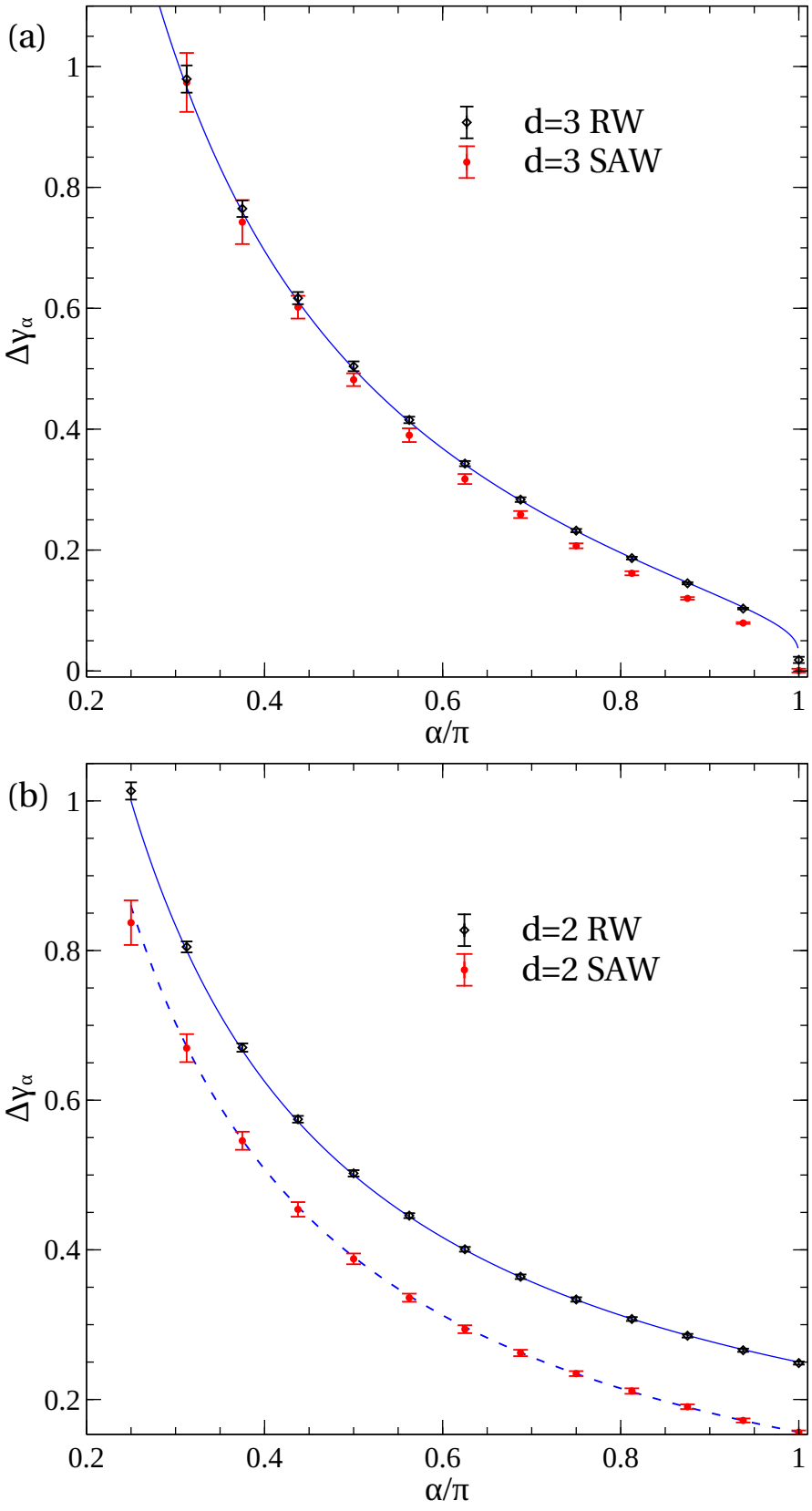

FIGURE 4.3: Difference in the critical exponents $\gamma - \gamma_\alpha$ as a function of the opening angle of the cone in dimension $d = 3$ (a) or wedge in $d = 2$ (b), for RWs (black diamonds) and SAWs (red circles). The dashed line represents the prediction by Cardy and Redner [77] for two-dimensional SAWs, while the solid lines represent known values for RWs [18, 19, 46, 53].

for RWs is also shown in Figure 4.3 (black diamonds). The dashed line in Figure 4.3(b) represents the prediction from conformal invariance [77], while the solid lines in Figures 4.3(a) and 4.3(b) represent the known values of $\Delta\gamma_\alpha$ for RWs in two and three dimensions [18, 19, 46, 53]. We find excellent agreement with all theoretical predictions. For SAWs in $d = 3$, where there are no analytical estimates for $\Delta\gamma_\alpha$, we present our numerical estimates in Table 4.1. Recently Clisby *et al.* [88] used the pivot algorithm to study SAWs near a flat plane ($\alpha = \pi/2$) and reached the very accurate estimate $\Delta\gamma_\alpha = 0.479315(20)$, in agreement with our result $\Delta\gamma_\alpha = 0.482 \pm 0.011$. Note that in [88] a specific geometry for the boundary was studied while in this work we study a range of excluded surfaces.

It is interesting to observe the dependence of the critical exponents on the dimensionality and the presence of self-avoidance when the cone/wedge is reduced to a semi-infinite line (when $\alpha \to \pi$) [91, 92, 93, 94]. In $d = 2$, a semi-infinite line is a significant barrier to the walk and the change in the critical exponent $\Delta\gamma_\pi > 0$. (In the language of renormalization group, one can say that in this case, the boundary constitutes a *relevant* perturbation on the free space Hamiltonian [91, 94]). In $d = 3$, the semi-infinite line is not a significant barrier and does not change the critical exponents. However, for ideal polymers in $d = 3$, $\Delta\gamma_\alpha$ approaches zero like $1/\ln|\pi - \alpha|$. (In this case the semi-infinite line constitutes a *marginal* perturbation). As can be seen in Figure 4.3(a) (solid line), the approach to zero is almost vertical. Note that the values shown for $\alpha/\pi = 1$ were measured for RWs and SAWs with an excluded semi-infinite line. For SAWs we measured $\Delta\gamma_\pi = 0$, while for RWs, the discrete space results in a small error in the opening angle of the cone that is significant due to the diverging derivative of $\Delta\gamma_\alpha$ near $\alpha = \pi$, and we measured $\Delta\gamma_\pi = 0.018$.

4.3 End-point distribution of self-avoiding walks in free space

To set the stage for the study of the end point distribution of SAWs confined to wedges and cones, we start with the end-point distribution for a SAW starting from the origin in *free* space $g_{\rm f}(\vec{r})$, normalized so that $\int g_{\rm f}(\vec{r})d^dr = 1$. The free space distribution was studied extensively over the years. In the limit $N \to \infty$, $g_{\rm f}(\vec{r})$ depends on $\vec{r}$ only through the ratio $\vec{r}/R$ [22],

$$g_{\rm f}(\vec{r}) = \frac{1}{R^d} f(r/R), \tag{4.3}$$

where the prefactor $1/R^d$ is required for normalization. Several properties of the function $f(x)$ are known [95, 96, 97, 98, 99]: For large values of x,

$$f(x) \propto x^{t_{\rm f}} \exp\left(-Dx^{\delta_{\rm f}}\right), \tag{4.4}$$

where

$$t_{\rm f} = (\nu d - \gamma_{\rm f} + 1 - d/2)/(1-\nu) \tag{4.5}$$

and

$$\delta_{\rm f} = 1/(1-\nu). \tag{4.6}$$

A similar exponential cutoff might be expected to hold for a polymer near an excluded cone/wedge, since the conformations of sizes significantly exceeding R are very rare. This effect is not expected to be modified significantly by the presence of an excluded boundary near one of the polymer ends. In the limit $x \to 0$, $f(x)$ describes the chance of a SAW to return to the origin. It is known that in this case

$$f(x) \propto x^{s_{\rm f}}, \tag{4.7}$$

where

$$s_{\rm f} = (\gamma_{\rm f} - 1)/\nu. \tag{4.8}$$

Note that these results carry over to ideal polymers, where, since $\gamma = 1$ and $\nu = 1/2$, the powers $t_{\rm f} = s_{\rm f} = 0$, i.e. the distribution does not vanish for $\vec{r} \to 0$. Also for ideal polymers $\delta_{\rm f} = 2$ and we recover the Gaussian distribution. Note that the Gaussian form at large x for an ideal polymer attached to a wedge/cone [Eq. (2.26)] is independent of the opening angle of the cone, as expected. The power law dependence in Eq. (4.7) is present when the system has no characteristic length scale, and thus we expect to find it again when the polymer is attached to a scale free surface like a cone or wedge. However, the dependence of the power $s_{\rm f}$ on the the other exponents, given in Eq. (4.8) relies on the translation invariance of the system [22, 99] and is not expected to hold when the boundary is introduced. Indeed, from Eq. (2.26) we see that for an ideal polymer, the power law dependence at small r does not agree with Eq. (4.8).

When attempting to extract powers such as t, s and δ from Monte Carlo simulations [100, 101, 102], we usually need to take into account two types of corrections to the analytical forms presented in Eqs. (4.3), (4.4) and (4.7). The first are corrections to scaling laws which result from the fact

that the walks in the simulation are finite. For example $R^2 \propto N^{\nu}(1 + O(N^{-\Delta}))$, where $\Delta \approx 1/2$ in $d = 2, 3$ [102]. As we mentioned in Section 4.2, we find that such corrections are negligible here when compared to the statistical scattering of the data. The second are nonasymptotic corrections which result from the fact that Eqs. (4.4) and (4.7) are expected to hold only in the regions $x \gg 1$ and $x \ll 1$ respectively. We attempted to estimate the effect of these correction by fitting different radial regions of the measured distributions separately. For small $x = r/R$ we used a simple power law of the form

$$f(x) = Ax^s, \tag{4.9}$$

with A and s the free parameters, and for the region of large x we used the form

$$f(x) = Bx^t \exp\left(-Dx^{\delta}\right), \tag{4.10}$$

with B, t, D, and δ as the free parameters. The cutoffs for the large and small x regions where selected so that the best agreement with the theory for the exponents s, t and δ is achieved. The same cutoffs were later used to analyze the behavior of SAWs attached the cones and wedges. We also fitted the entire distribution to a function of the form given in Eq. (4.10), to see if it can be described by such a 'phenomenological' function [100, 101, 102]. Note that in principle, when using the entire distribution, the parameters in Eq. (4.10) are not independent of each other due to normalization conditions. We do not take that into account directly in the fitting procedure but only indirectly by using properly normalized data. For SAWs in $d = 3$ we find that attempting to fit different regions of the distribution separately does not alter or improve the results obtained by the phenomenological description and we only present the exponents derived from the phenomenological fit. This is not surprising since in $d = 3$, $t_{\mathrm{f}} \approx s_{\mathrm{f}} \approx 0.26$ and both Eq. (4.4) and Eq. (4.7) can be satisfied by the same function. In $d = 2$ we used $x > 1.1$ for the large x fit (blue dashed line in Figure 4.4(a) and $x < 0.4$ for the small x fit (red dash-dot line). The exponents obtained from the fits to the free space end-point distributions are given in Tables 4.2 and 4.3.

We find good agreement with the theory apart from a slightly smaller value of s_{f} and t_{f} both in $d = 2$ and $d = 3$, probably due to the nonasymptotic corrections mentioned above. Note that the error estimates in the tables represent statistical scattering of the data but not systematical errors caused by non-asymptotic corrections for example.

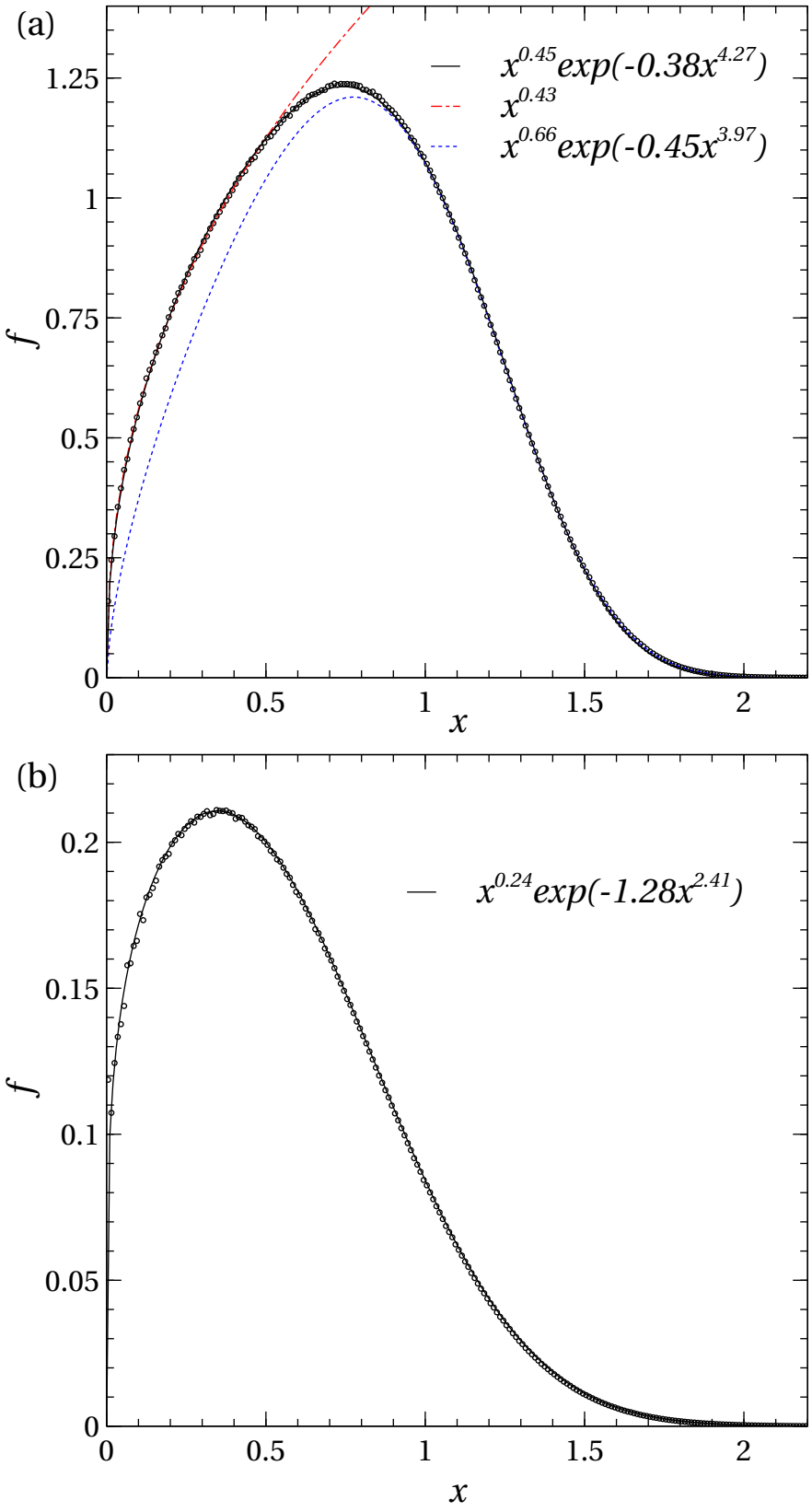

FIGURE 4.4: Scaled end-point distribution function $f(x) = R^d g_f(\vec{r})$ of a SAW in free space with (a) 10^5 steps on a cubic lattice and (b) 5×10^5 steps on a square lattice, where R^2 is the mean square end-to-end distance of the walk and $x = r/R$. The solid lines are fits to the function in Eq. (4.10). The blue dashed line is a fit to a function of the same form performed only on the region $x > 1.1$. The red dash-dot line is a fit to a simple power law [Eq. (4.9)], performed only on the region $x < 0.4$.

	s	t	δ
theory	0.458	0.625	4
pheno.	-	0.4507 ± 0.0016	4.269 ± 0.014
$x > 1.1$	-	0.66 ± 0.05	3.97 ± 0.07
$x < 0.4$	0.436 ± 0.003	-	-

TABLE 4.2: Scaling exponents describing the end-point distribution of a free SAW in $d = 2$ with 5×10^5 steps. The numerical values were obtained from the fits shown in Figure 4.4(a). The phenomenological results (pheno.) were obtained by fitting the entire distribution to the form given in Eq. (4.10). We also attempted to use only the region with $x > 1.1$ to the same functional form while fitting a simple power law [Eq. (4.9)] to the region $x < 0.4$. The error estimates are derived from statistical scattering of the data and do not include systematical corrections mentioned in the text.

	t	δ
free theory	0.260	2.427
free numeric	0.2435 ± 0.0019	2.413 ± 0.008
$\alpha = 3\pi/8$	1.408 ± 0.047	2.662 ± 0.088
$\alpha = \pi/2$	0.952 ± 0.015	2.615 ± 0.036
$\alpha = 5\pi/8$	0.6883 ± 0.0082	2.560 ± 0.023
$\alpha = 3\pi/4$	0.5278 ± 0.0043	2.505 ± 0.013
$\alpha = 7\pi/8$	0.3923 ± 0.0028	2.4838 ± 0.0094
$\alpha = \pi$	0.2508 ± 0.0021	2.4078 ± 0.0074

TABLE 4.3: Scaling exponents describing the end-point distribution of SAWs in $d = 3$ with 10^5 steps in free space [Figure 4.4(b)] or attached to the tip of an excluded cone with opening angle α [Figure 4.5(b)]. The numerical values were obtained from the fits shown in Fig. 4.4(b) and 4.5b, were we used the function from Eq. (4.4). The error estimates are derived from statistical scattering of the data and do not include systematical corrections mentioned in the text.

	pheno.		$x > 1.1$		$x < 0.4$
α	t	δ	t	δ	s
$3\pi/8$	1.500 ± 0.022	4.834 ± 0.084	1.64 ± 0.42	4.47 ± 0.34	1.54 ± 0.11
$\pi/2$	1.1596 ± 0.01	4.794 ± 0.048	1.42 ± 0.21	4.24 ± 0.16	1.126 ± 0.046
$5\pi/8$	0.9630 ± 0.0063	4.754 ± 0.036	1.54 ± 0.16	3.99 ± 0.10	0.916 ± 0.019
$3\pi/4$	0.8373 ± 0.0056	4.710 ± 0.036	1.51 ± 0.13	3.911 ± 0.082	0.782 ± 0.014
$7\pi/8$	0.7425 ± 0.0051	4.682 ± 0.36	1.26 ± 0.10	3.969 ± 0.069	0.6870 ± 0.0092
π	0.6736 ± 0.0049	4.659 ± 0.037	1.097 ± 0.087	4.00 ± 0.059	0.6166 ± 0.0084

TABLE 4.4: Scaling exponents describing the end-point distribution of a SAW with 5×10^5 steps on a square lattice attached to the corner of an excluded wedge with opening angle α. The values were obtained from the fits shown in Figure 4.5(a). The phenomenological results (pheno.) were obtained by fitting the entire distribution to the form given in Eq. (4.10). We also attempted to use only the region $x > 1.1$ and fit to the same functional form while fitting a simple power law [Eq. (4.9)] to the region $x < 0.4$. The error estimates are derived from statistical scattering of the data and do not include systematical corrections mentioned in the text.

4.4 End-point distribution for SAWs attached to wedges and cones

4.4.1 Radial distribution

In order to understand the behavior of SAW attached to wedges and cones, we attempt to separate the radial and the angular dependence of the end-point distribution, as can be done for RWs (Eq. (2.26)). To study the radial behavior we define

$$g_\alpha(r) \equiv \int_{-\alpha}^{\alpha} g_\alpha(r,\theta) d\theta \quad (d=2), \tag{4.11}$$
$$g_\alpha(r) \equiv \int_{0}^{\alpha} g_\alpha(r,\theta) \sin\theta d\theta \quad (d=3).$$

We also define the scaled distribution $f_\alpha(x) = R^d g_\alpha(r)$, where $x = r/R$ as before. In Figure 4.5 we present the radial end-point distributions $f_\alpha(x)$ for SAWs starting from the tip of an excluded cone/wedge with opening angle α. The exponents extracted from the fits are shown in Tables 4.3 and 4.4.

Both in $d = 2$ and $d = 3$, $f_\alpha(x)$ can be closely approximated by a single function of the form given in Eq. (4.10). The power s at small radii increases dramatically when the opening angle is decreased (from 0.25 to 1.4 in $d = 3$ and from 0.67 to 1.5 in $d = 2$), while the exponential decline at large x remains roughly the same. In the case of a semi-infinite line ($\alpha = \pi$), we see again that for a SAW in $d = 3$ the effect of the line is negligible, and $f_\pi(x)$ is indistinguishable from $2f(x)$ [Figure 4.5(b)]. Note that the factor two enters here due to the azimuthal symmetry), while in $d = 2$, the distribution differs significantly from the free space form [Figure 4.5(a)]. We see that the

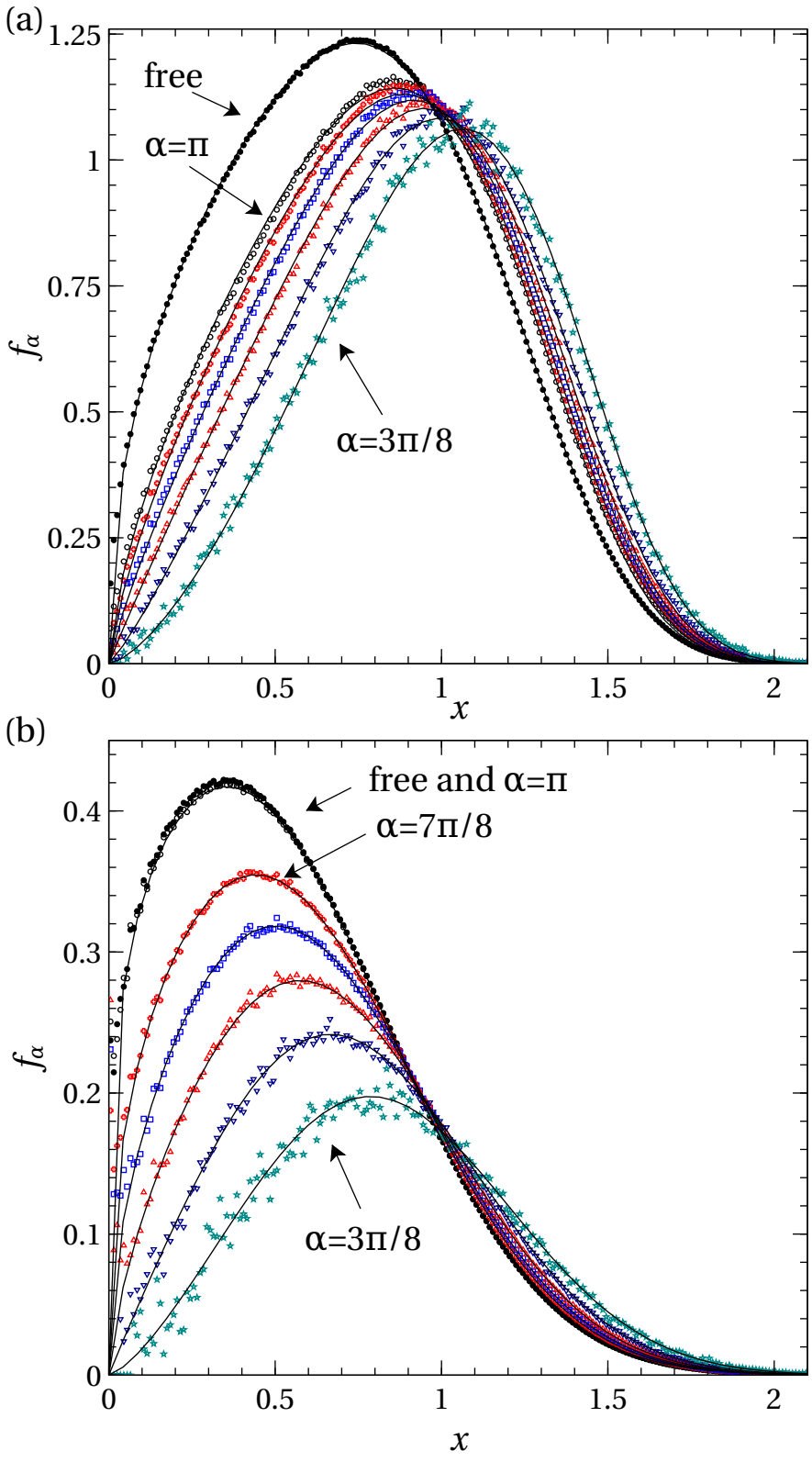

FIGURE 4.5: Scaled radial end-point distribution $f_\alpha(x) = R^d g_\alpha(r)$ of a SAW with (a) 10^5 steps on a cubic lattice and (b) 5×10^5 steps on a square lattice starting near the tip of an excluded wedge/cone with opening angle α, where r is the distance from the tip of the wedge/cone, R^2 is the mean square end-to-end distance of the walk in free space and $x = r/R$. The distributions are plotted for $\alpha = i\pi/8$ with $i = 3, 4, .., 8$. The solid lines are fits to the functional form in Eq. (4.10). We also plot the free space distributions $f(x)$ in $d = 2$ and $2f(x)$ in $d = 3$, where the factor two enters due to the azimuthal symmetry.

radial dependence of polymers in good solvent is qualitatively similar to that of ideal polymers. The opening angle of the cone/wedge affects the exponent s, whereas the exponent δ, related to large stretching of the polymer, is roughly independent of the surface to which the polymer is attached. The small variations in δ with respect to the opening angle of the cone are most likely a result of our fitting procedure, where we impose simple functional forms on the end-point distribution.

4.4.2 Angular distribution in the wedge

We now turn to the angular distribution of end-points in the wedge ($d = 2$). In [77] the angular distribution for a two-dimensional walk was defined,

$$g_\alpha(\theta) \equiv \int_0^\infty g(r,\theta) r dr, \tag{4.12}$$

and it was predicted that for SAWs starting from the corner of an excluded wedge,

$$g_\alpha(\theta) \propto \left[\cos\left(\frac{\theta\pi}{2\alpha}\right)\right]^{\frac{\Delta\gamma_{\pi/2}}{\nu}}. \tag{4.13}$$

Note that the power $\Delta\gamma_{\pi/2}/\nu$ is determined by the exponents of a polymer near an infinite line (where $\alpha = \pi/2$), and is *independent of the opening angle of the wedge* to which the polymer is attached. This behavior also exists in ideal polymers, where, in $d = 2$ the angular function from Eq. (2.26), $\Theta_\alpha(\theta) = \cos(\theta\pi/2\alpha)$ [46, 53]. Eq. (4.13) was found to be in good agreement with extrapolation of enumeration of short SAWs, although small systematical discrepancies were observed [77].

We measured the angular density for RWs with $N = 10^6$ steps and SAWs with $N = 5 \times 10^5$. In order to test the validity of Eq. (4.13), we attempted to fit the angular density to the form

$$g_\alpha(\theta) = A\left[\cos\left(\frac{\theta\pi}{2\alpha}\right)\right]^y, \tag{4.14}$$

where A and y are the free parameters. In Figure 4.6 we present $g_\alpha(\theta)$ along with the corresponding fits for selected opening angles α. The power y extracted from the fits is presented in Figure 4.7.

For RWs, we find that the power is close to the known value for infinite walks, $y = 1$, with deviations that result from the fact that the walks in the simulation are finite. The functional form in Eq. (2.26) is expected to hold when h, the distance between the starting point of the polymer and the corner of the wedge (ten lattice units in this case), is much smaller than the characteristic

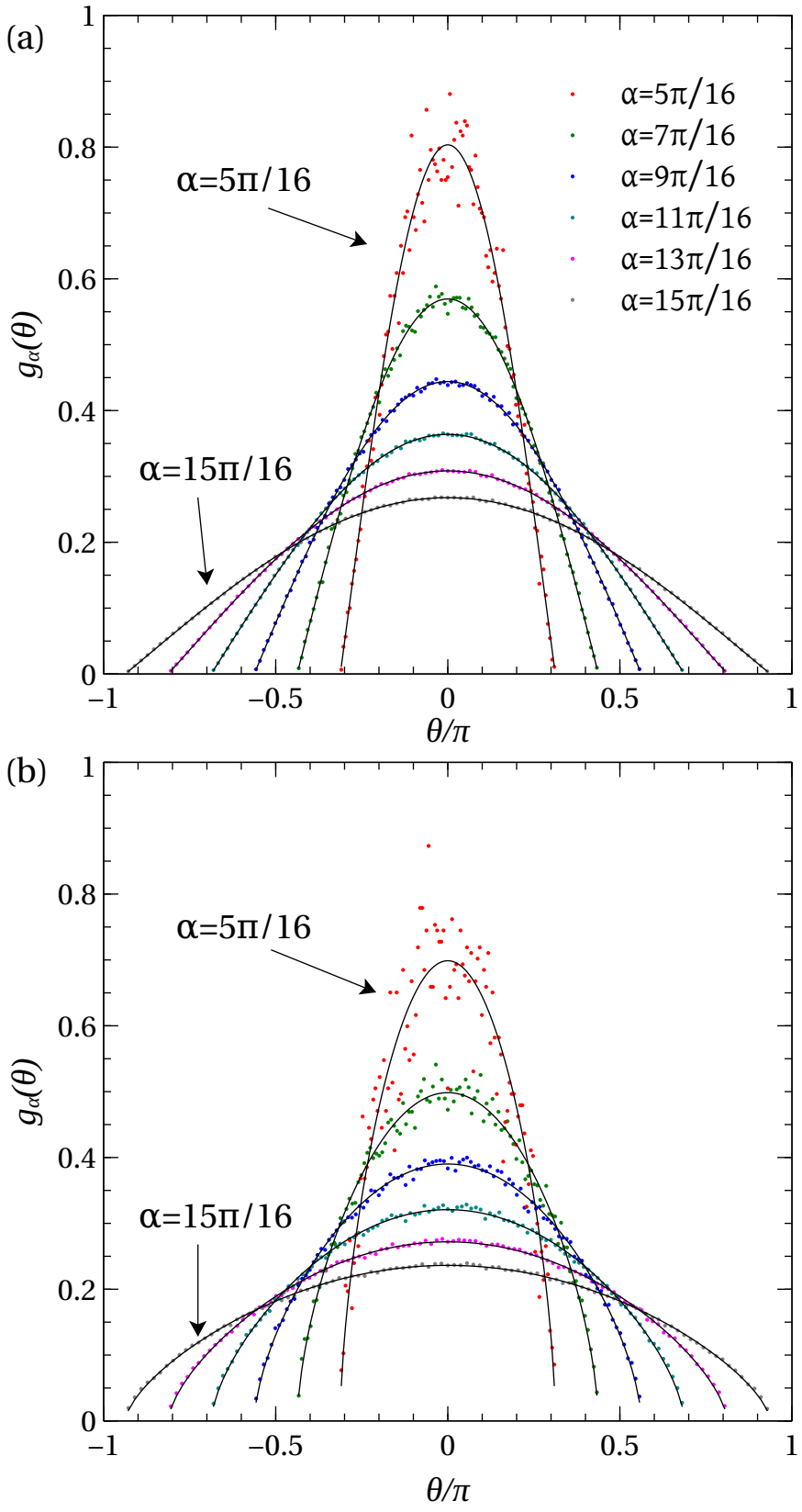

FIGURE 4.6: Angular probability distribution for the end-point of (a) a RW of size $N = 10^6$ and (b) a SAW of size $N = 5 \times 10^5$ starting near the corner of a two-dimensional wedge with opening angles $\alpha = j\pi/16$ where $j = 5, 7, .., 15$. The continuous lines represent fits made to the functional form in Eq. (4.14).

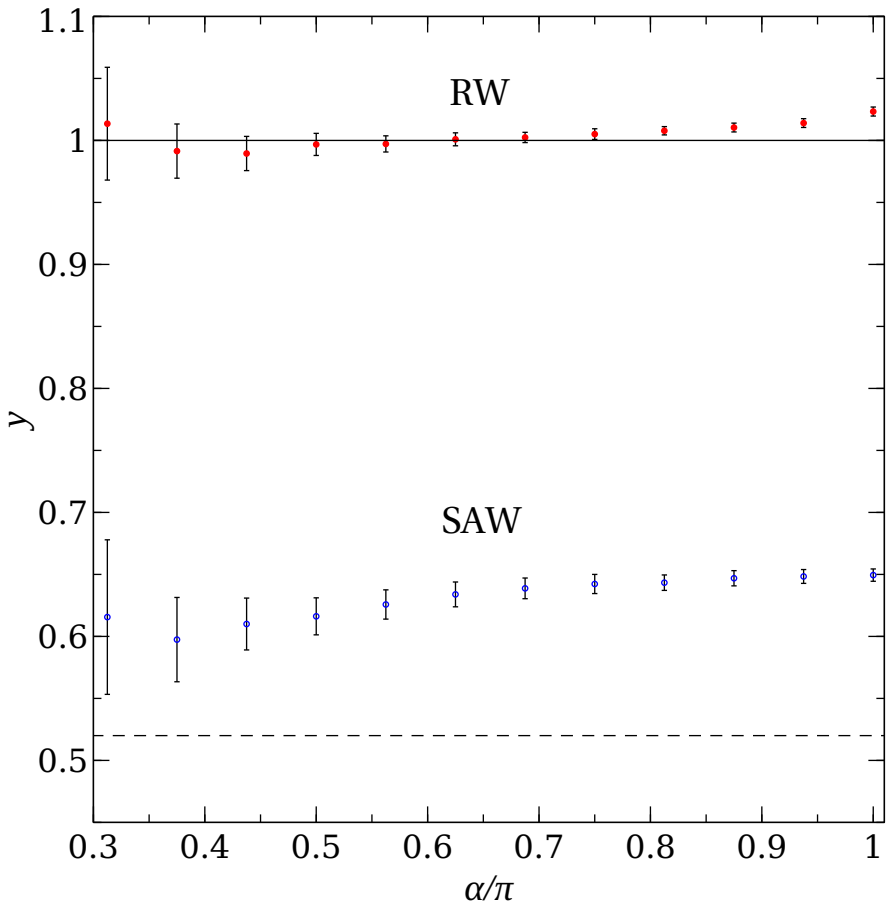

FIGURE 4.7: The power y extracted from the fits in Fig. 4.6, as a function of the opening angle of the wedge. The solid line denotes the known value $y = 1$ for RWs. The dashed line denotes the prediction in [77] for SAWs.

size of the polymer (say R). As can be seen in Figure 4.7, for larger values of α, where the polymer is less confined and R is smaller, the deviation from the line $x = 1$ is more significant. Note that for the SAWs in the simulation the characteristic sizes are much greater (since ν is greater) and we do not expect such corrections to be important.

For SAWs, the power y does not match the predicted value, $y = 0.52$ [77], and exhibits a weak dependence on the opening angle of the wedge. The small deviation is in fact consistent with the systematical errors reported in [77]. The prediction in Eq. (4.13) is based on the assumption that the dominant contribution for the integral in Eq. (4.12) comes from a region where $\rho_\alpha(r,\theta)$ can be separated into a product of angular and radial functions and the angular part has the form given in Eq. (4.13). This kind of separation is expected to occur for long polymers in the limits $r \gg R$ or $R \gg r \gg h$, since in these regions the system has no typical length scale. For long RWs, we know the separation into a product of radial and angular functions occurs for any r (see Eq. (2.26)). We measured the detailed end-point probability distribution $g(r,\theta)$ for a two-dimensional SAW near an excluded semi-infinite line. As can be seen in Figure 4.8, the distribution *does not* separate to a product of a radial and angular functions. To get a sense of the angular dependence of g, we fitted the angular distribution at different radii to the form in Eq. (4.14) and observed the changes in the power y computed from the fits [Figure 4.8(b)]. For small r/R, g is flatter, i.e., displays weaker variation with respect to θ. For large r/R, the power y saturates as expected. We find that $g_{\alpha=\pi}(r,\theta)$ can be roughly approximated by the function

$$g_\alpha(r,\theta) \propto \left\{ x^{a_1} \left[\cos\left(\frac{\theta\pi}{2\alpha}\right)\right]^{b_1} + A x^{a_2} \left[\cos\left(\frac{\theta\pi}{2\alpha}\right)\right]^{b_2} \right\} e^{-Bx^4}, \tag{4.15}$$

where $x = r/R$ as before, $a_1 = 1.9$, $a_2 = 3.53$, $A = 3.84$, $b_1 = 0.3$, $b_2 = 0.8$ and $B = 0.44$. The power in the exponent in Eq. (4.15) was assumed to be $\delta = 1/(1-\nu) = 4$, as is known for a SAW in free space and in accordance with the results of Sec. 4.4.1. These values should not be taken too seriously. The function in Eq. (4.15) is an example of a simple form of $g_\alpha(r,\theta)$ that separates into a product of angular and radial functions for $x \ll 1$ and $x \gg 1$ but displays non-trivial angular dependence for arbitrary x. The density in Eq. (4.15) crosses over between two powers of the cosine at a typical radius that depends on A, B, a_1 and a_2. It seems that to properly describe $g_\alpha(r,\theta)$ for SAWs in wedges, more terms similar to the two in the curly brackets of Eq. (4.15) with different powers and prefactors must be used.

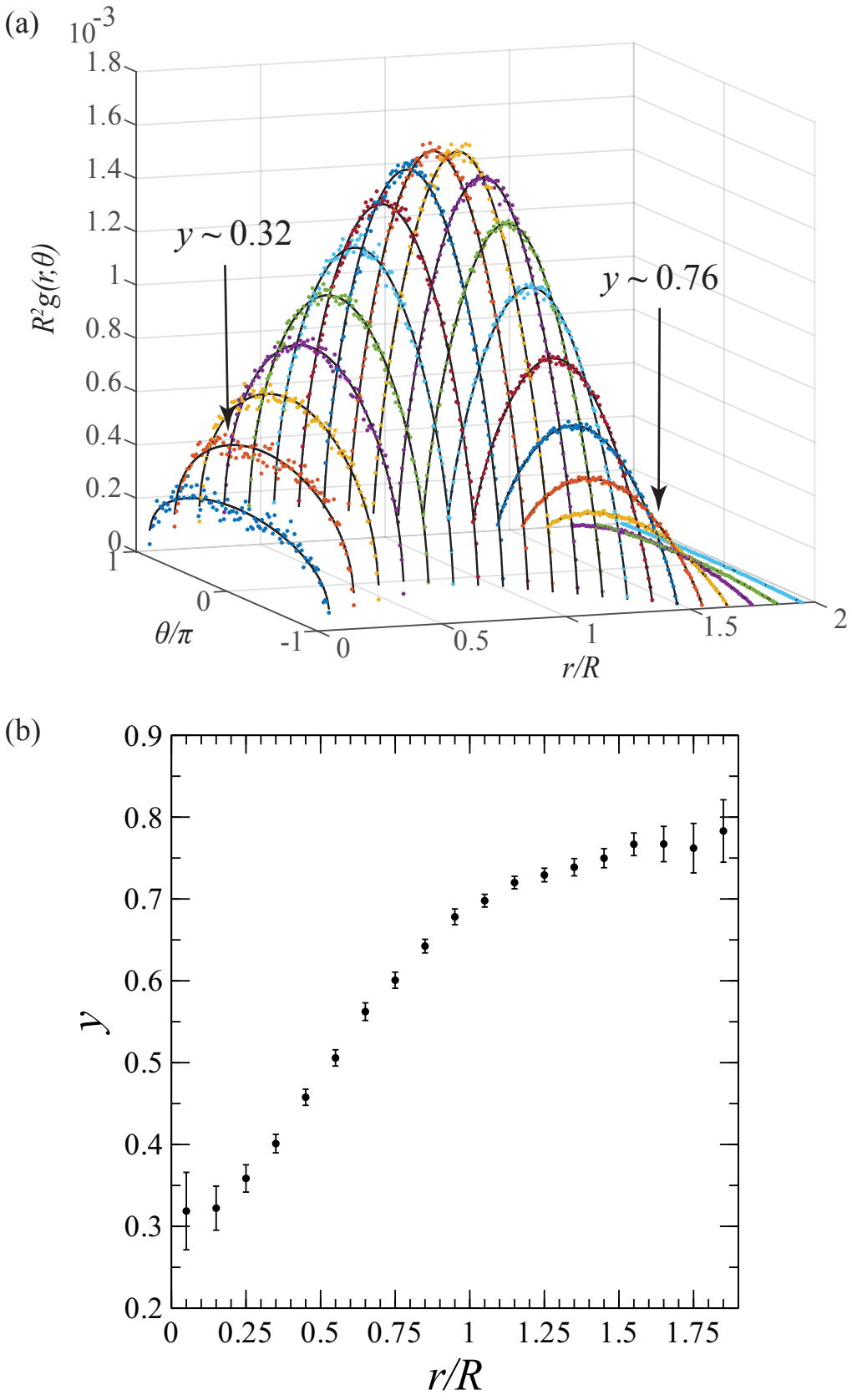

FIGURE 4.8: (a) End-point distribution function $g(r,\theta)$ of a SAW of 5×10^5 steps near an excluded semi-infinite line, for various values of r/R, where R^2 is the mean square end-to-end distance of a SAW in free space (without the excluded line). The solid lines represents fits to the functional form in Eq. (4.14). (b) The power y from the fits in (a).

4.5 Universal size ratio R_α^2/R^2

The ratio between the mean square end-to-end distance R_α^2 of the polymer attached to a cone/wedge and R^2 for a polymer in free space is a universal property which becomes independent of N for large polymers. It was studied for a polymer near a flat surface both numerically [103, 104] and analytically [105, 106, 107, 108, 94]. Freed [105] extended the renormalization group method to include polymers attached to a wall. The wall and the steric repulsion between monomers were introduced as perturbations to the ideal polymer model in free space. If the surface has dimension $d_\parallel = 2$, both the steric repulsion and the boundary become irrelevant when the dimension of the system $d > 4$ (see Sec. 4.2). The end-point distribution function and the polymer size can then be evaluated by expanding in $\epsilon = 4 - d$. Douglas and Kosmas [94] treated a polymer near a surface of arbitrary dimension by introducing a second parameter $\epsilon_\perp = (2 + d_\parallel) - d$. They showed that to first order in ϵ and $\epsilon_\perp$ the universal ratio depends only on the dimensions of the system and the surface and on the exponent ν. For a real polymer in $d = 3$ near a plane, which corresponds to $\alpha = \pi/2$ in our description, they found $R_\alpha^2/R^2 \approx 7/6$. We measured a value of 1.22, in agreement with [107].

For ideal polymers (RWs), Eq. (2.27) determines R_α^2/R^2 and the α dependence of the ratio can be written in terms of $\Delta\gamma_\alpha$,

$$R_\alpha^2/R^2 = \frac{\Delta\gamma_\alpha}{d\nu} + 1. \tag{4.16}$$

Even though $g_\alpha(r)$ for SAWs is different from that which is known for RWs (see Sec. 4.4.1), we compared the universal ratio R_α^2/R^2 measured for SAWs to the measured $\Delta\gamma_\alpha$. As is shown in Figure 4.9, we find that Eq. (4.16) describes the relationship between these properties quite well, especially in $d = 3$. It is not surprising that the ratio R_α^2/R^2 can be expressed in terms $\Delta\gamma_\alpha$, since both R_α^2/R^2 and $\Delta\gamma_\alpha$ are monotonic functions of α. However, it is notable that R_α^2/R^2 is, to a good approximation, linear in $\Delta\gamma_\alpha$ for a wide range of opening angles, with the *same* slope in terms of universal exponents as is known analytically for RWs. Quantitatively, we observe that

$$R_\alpha^2/R^2 = 1 + A_1\Delta\gamma + A_2\Delta\gamma^2 + ..., \tag{4.17}$$

where $A_1 = 1/d\nu$, while $A_2 < 0.01$ in $d = 3$ and $A_2 \sim 0.1$ in $d = 2$. We do not have an analytical basis for this result. Possibly, such a relation may emerge from higher order terms in the renormalization group approach.

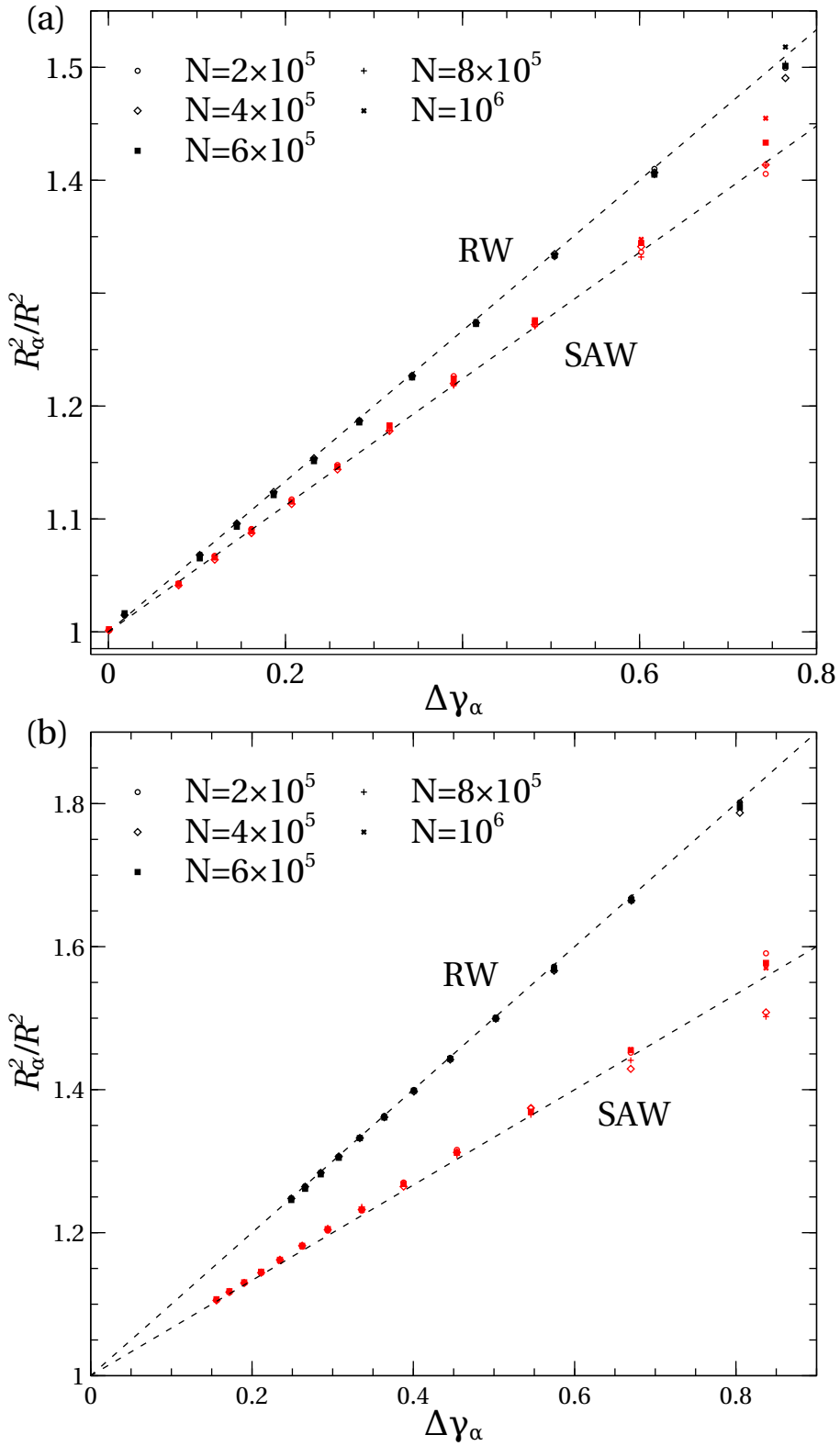

FIGURE 4.9: Mean square end-to-end distance R_α^2 for RWs (black symbols) and SAWs (red symbols) of 5 sizes from $N = 2 \times 10^5$ to $N = 10^6$, starting from the tip of a repulsive cone in $d = 3$ (a) or wedge in $d = 2$ (b) with opening angle α, divided by the corresponding mean square end-to-end distance of the walks in free space R^2. The ratio is shown as a function of the difference in the critical exponent γ for a polymer in free space and a polymer attached to a cone/wedge. The dashed lines denote the known theoretical result for infinite RWs (Eq. (4.16)).

4.6 Summary and conclusions

The generation of large ensembles of long chains has always presented a challenge in polymer simulations [78, 79]. This is especially true when attempting to measure universal properties, since the critical point in the polymer system is reached only in the limit $N \to \infty$. The recent implementation of the pivot algorithm by Clisby [2, 26], allowed a significant increase in polymer sizes feasible in simulations.

In this work, we demonstrated that by using intersection tests with surfaces that take advantage of the SAW tree data structure (which lies at the heart of Clisby's implementation), it is possible to perform a direct study of large polymers near surfaces and measure their universal properties. We expect that this advancement can be used not only in the study of polymers in various geometries, but also in simulating polymers with different topology (e.g. star polymers [109] and polymer brushes [110]). In the next Chapter, we improve upon the numerical methods used here and study the winding angle distribution of RWs and SAWs of sizes ranging up to $N = 10^7$ steps.

Scale free boundaries such as infinite wedges and cones constitute a special class of systems, where the universal properties change continuously (e.g. with the opening angle of the cone/wedge). This quality makes it possible to study universal properties which are shape depended like γ_α and R_α^2/R^2 and find relations like that in Eq. (4.17).

Our study of the end-point distribution of SAWs in wedges and cones revealed similarities in the radial behavior of the distribution $g_\alpha(r)$ to the IP case which was studied in Chapter 2 (especially regarding the ratio R_α^2/R^2), but also an important difference in the angular dependence. The end-point distribution $g_\alpha(r,\theta)$ for SAWs is more complicated than that of RWs and generally does not separate into a product of angular and radial functions.

Chapter 5

Winding Angles of Long Lattice Walks[1]

As we have shown in the previous Chapter, Clisby's SAW tree allows the numerical study of SAWs of sizes that were not previously available to simulations. This is particularly important when studying properties of polymers that increase very slowly with N, like the winding angle of polymers around a point (in $d = 2$) or a line ($d = 3$).

In this Chapter we use the SAW tree structure to perform measurements of the winding angles of RWs and SAWs with N ranging up to 10^7. In Section 5.1 we explain how the winding angle can be measured in a very efficient way. In Sections 5.2 and 5.3 we verify the theoretical predictions for RWs and planar SAWs. In Sections 5.4 and 5.5 we study the unsolved problem of a SAW winding in $d = 3$ around a line.

5.1 Efficient measurement of global properties of polymers

As we have seen in Chapter 4, the pivot algorithm [84, 85, 86, 2, 26], particularly in Clisby's implementation, is a highly efficient method to study global properties of SAWs. A pivot attempt can be performed in a time not exceeding $O(\ln N)$. Clisby accomplished this by storing the walks in a new data structure in which a walk is represented as the concatenation of sub-walks of smaller sizes. A global property of the walk can be deduced from the properties of the sub-walks it is constructed from. For example, the end-point of the walk can be found by using the end-points of each of the sub-walks, along with the symmetry operation used during the concatenation. This is illustrated in Figure 5.1. In Figure 5.1(a) two SAWs on a square lattice, w_1 and w_2, are drawn. The SAW in Fig. 5.1(b) is obtained by applying the symmetry operation q (a 90 degree counter-clockwise rotation) to w_2 and then concatenating it with w_1. Note that we use the convention that all walks start from $(1, 0)$. The end point $\mathbf{x}_i$ of w_i is marked by a dashed line in Figs. 5.1(a) and 5.1(b). It is

[1] The work presented in this chapter was published in [111].

shown that $\mathbf{x}_3$ can be derived from $\mathbf{x}_1$, $\mathbf{x}_2$ and q, without knowing the positions of all the sites in the walk.

The data structure used to represent the walks in the simulation is a binary tree where each node contains the global properties of the walk which corresponds to sub-tree that contains all the nodes below it in the tree. These properties include the end point of the walk, the symmetry operation used to concatenate its sub-walks and a bounding box. The bounding box is a convex shape that completely contains the walk [see Figures 5.1(a),(b)]. Clisby showed that pivot operations can be done by applying transformations to change the structure of the tree and the symmetry operations in the nodes. Moreover, self intersection tests can be done by recursively checking for intersections between the bounding boxes of right and left children in the tree. These procedures are explained in detail in [2].

In our simulation, we use the fact that the winding angle of a random or SAW is also a global property that can be deduced from the sub-walks that form it. Consider a random or SAW w which is represented by Clisby's binary tree. The following recursive function can be used to compute its winding angle:

Compute $\varphi(w)$

1. Check whether the bounding box of w intersects with the line (in dimension $d = 3$) or point (in $d = 2$) $x = y = 0$.

2. If not, there is no possibility that the walk has encircled the origin and the winding angle can be computed immediately from the position of the first site and the end point of the walk. The function will then return this angle and terminate. Note that the necessary information is found in the node at the root of the tree and there is no need to trace the sites along the walk.

3. If the bounding box does intersect with the line/point $x = y = 0$:

   (a) Call the function again to calculate $\varphi_1 =$ *compute* $\varphi(w_l)$, where w_l is the sub-walk of w that corresponds to the left sub-tree of the SAW tree which represents w.

   (b) Call the function again to calculate $\varphi_2 =$ *compute* $\varphi(w_r)$, where w_r is defined similarly to w_l. Note that when computing φ_2 we need to take into account the fact that w_r is acted upon by a symmetry operation q and then shifted to the end point of w_l, $\mathbf{x}_l$, before it is concatenated with w_l.

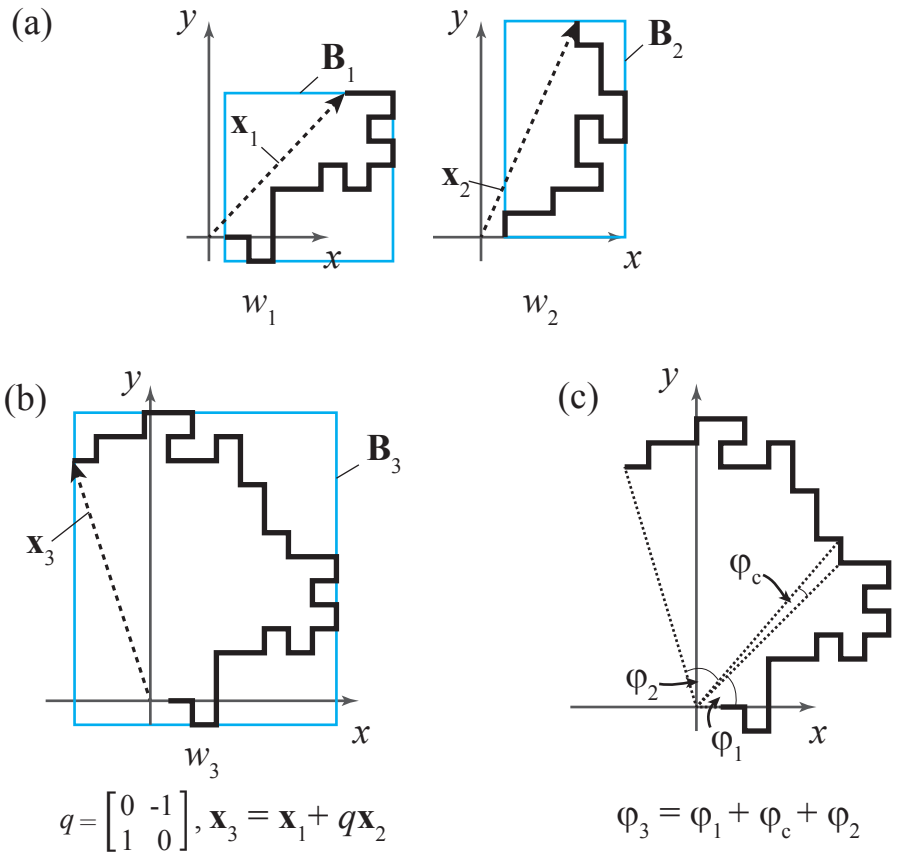

FIGURE 5.1: (a) Two SAWs, w_1 and w_2, drawn on a square lattice. By convention the walks start at $(1, 0)$. The end points of the walks are denoted $\mathbf{x}_1$ and $\mathbf{x}_2$, and are indicated by the dashed lines. The bounding boxes of the walks are marked by the cyan rectangles. (b) The walk w_3 is obtained by using a symmetry operation q on w_2 and then concatenating it with w_1. The end point $\mathbf{x}_3$ can be obtained from $\mathbf{x}_1$, $\mathbf{x}_2$ and q without knowing the position of all the sites along the walks w_1 and w_2. (c) The winding angle φ_3 of w_3 can also be derived from the global properties of its sub-walks. The angles φ_1, φ_2 and φ_c can be computed from the knowledge of $\mathbf{x}_1$, $\mathbf{x}_2$ and q, without tracing all the steps along the walk.

(c) Calculate the angle φ_c, between the last site of w_l and the first site of w_r. This angle will depend only on $\mathbf{x}_l$ and q.

4. return $\varphi_1 + \varphi_c + \varphi_2$.

The operation of *Compute* $\varphi(w)$ is illustrated in Figure 5.1(c). In order to compute the winding angle of w_3, the function will first check whether its bounding box intersects with the origin. Since in this case it *does* intersect with the origin [see Figure 5.1(b)]. The function will continue to compute φ_1 and φ_2 recursively and the angle φ_c shown in the figure and return their sum. Since the lattice walks tend to move away from the origin, when the function *Compute* $\varphi(w)$ is called to compute the winding angle of sections of the walk that are far from its beginning, it will usually find that their bounding boxes do not intersect with the point/line $x = y = 0$, and return their winding angle in a single step. In fact, we find that the number of times that *Compute* $\varphi(w)$ is called is very small even when the number of sites in w is large. This is illustrated in Figure 5.2. For example, in order to compute the winding angle of a SAW in $d = 3$ with $N = 10^7$, the recursive function is called only 62 times on average.

In what follows, we study the winding angles of RWs and SAWs of sizes ranging from $N = 100$ to $N = 10^7$ sites on square and cubic lattices. For each size, we started from an initial configuration, performed a sequence of pivot attempts and computed their winding angles after each attempt. The initial configuration was selected in the same way as in Chapter 4. If, as a result of a potential pivot move the walk intersects with the point/line $x = y = 0$, or, for a SAW, intersects with itself, the pivot move is rejected and the same configuration is sampled again. An important detail in the implementation of the pivot algorithm is the distribution from which the pivot point along the walk is selected. Usually, the pivot point is selected uniformly from the sites along the walk [85]. However, when computing the winding angle of the walks, we find that the correlation between successive measurements is significantly reduced when we use a distribution that favors sites closer to the starting point of the walk. We used the distribution that was defined in [88].

5.2 Winding angle of random walks

In order to test the theoretical prediction for the winding angle of RWs we can compute the average square winding angle and check its dependence on N. From Eq. (1.15),

$$\langle x^2 \rangle = \int x^2 p(x) dx = \frac{1}{3}, \tag{5.1}$$

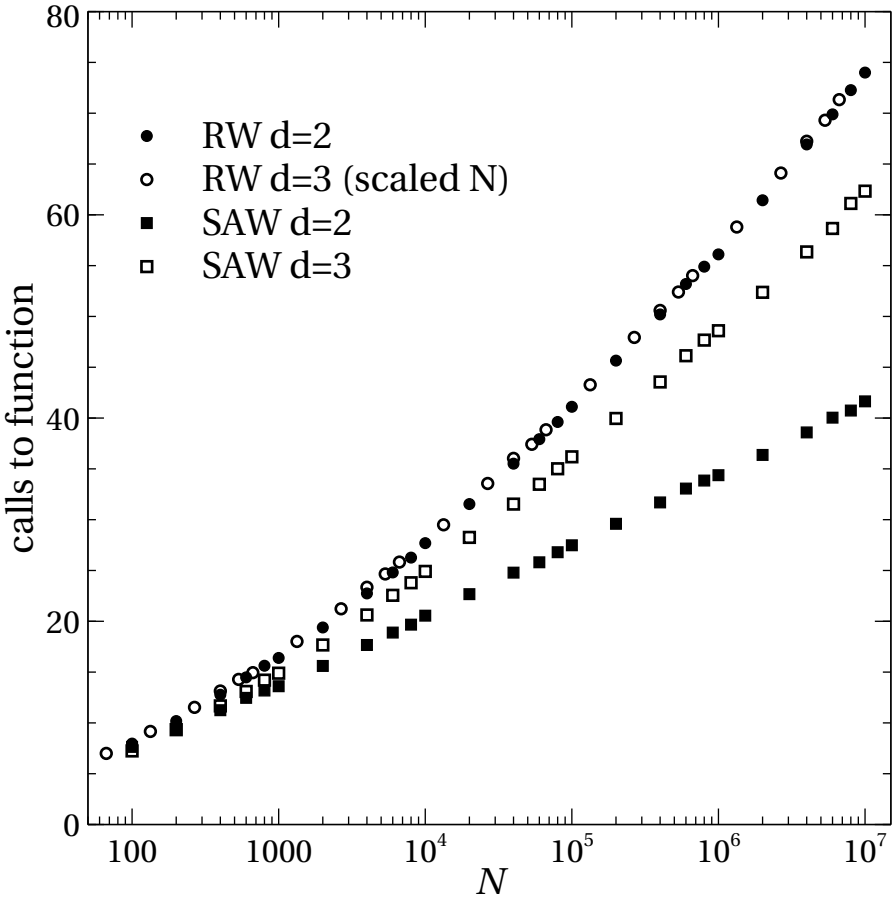

FIGURE 5.2: The average number of times the recursive function *Compute* $\varphi(w)$ that computes the winding angle of an N-step walk w is called as a function of the number of sites N of the walk. The circles denote RWs and the squares denote SAWs. Open symbols correspond to dimension $d = 3$ and full symbols to $d = 2$. Note that for RWs in $d = 3$, we re-scaled N by a factor of $2/3$, the average fraction of steps taken in a direction perpendicular to the z axis.

i.e., $\langle\varphi^2\rangle = (\ln t)^2/12$. For a RW with large N, the winding angle is expected to agree with Eq. (1.15) where the diffusion time t is proportional to the number of steps in the walk, i.e., $t = c_0 N$. We therefore expect that in the large N limit,

$$\sqrt{\langle\varphi^2\rangle} = \frac{1}{\sqrt{12}}(\ln c_0 + \ln N) = A + \frac{1}{\sqrt{12}} \ln N. \tag{5.2}$$

The additive constant A in Eq. (5.2) depends on local properties of the system like the shape and size of the excluded area near the origin where the RW is not allowed to visit [38]. However, in the large N limit, the root mean square winding angle should be proportional to $\ln N$ with a prefactor of $1/\sqrt{12}$, independent of any local properties.

In [33], $\sqrt{\langle\varphi^2\rangle}$ was studied as a function of N for RWs on a square and cubic lattices with N ranging up to 10^3. Some non-negligible deviations from the theory were observed, and it was stipulated that the main reason for these was finite size corrections. Here we use walks with $N = 10^2 - 10^7$ to study the effect of finite N and see if $\sqrt{\langle\varphi^2\rangle}$ converges to the predicted form when N increases.

In Figure 5.3(a), $\sqrt{\langle\varphi^2\rangle}$ is plotted against N in semi-logarithmic scale. The dependence is very close to linear. In order to take into account the finite size corrections, we performed two non-linear fits. The first was to the form

$$\sqrt{\langle\varphi^2\rangle} = A + B \ln N + C(\ln N)^{-\Delta}, \tag{5.3}$$

and in the second we used integer powers of $1/\ln N$, i.e.,

$$\sqrt{\langle\varphi^2\rangle} = c_0 + c_1 \ln N + c_2(\ln N)^{-1} + c_3(\ln N)^{-2}. \tag{5.4}$$

The curves produced by the two forms are practically indistinguishable for the values of N in our simulation. For a RW on a square lattice, this curve is denoted by the solid line in Figure 5.3(a), where it is shown that it is in a slightly better agreement with the data than the linear fit denoted by the dashed line. In Figures 5.3(b) and 5.3(c) we present the residuals of the linear and non-linear fits. Clearly, the linear form suffers from a systematic disagreement with the data, while the residuals of the non-linear form seem to scatter randomly around zero. Thus, both Eq. (5.3) and Eq. (5.4) agree with the results of our simulations. A similar behavior was observed for RWs on the cubic lattice. The fitting parameters acquired from the non-linear fits are presented in Table

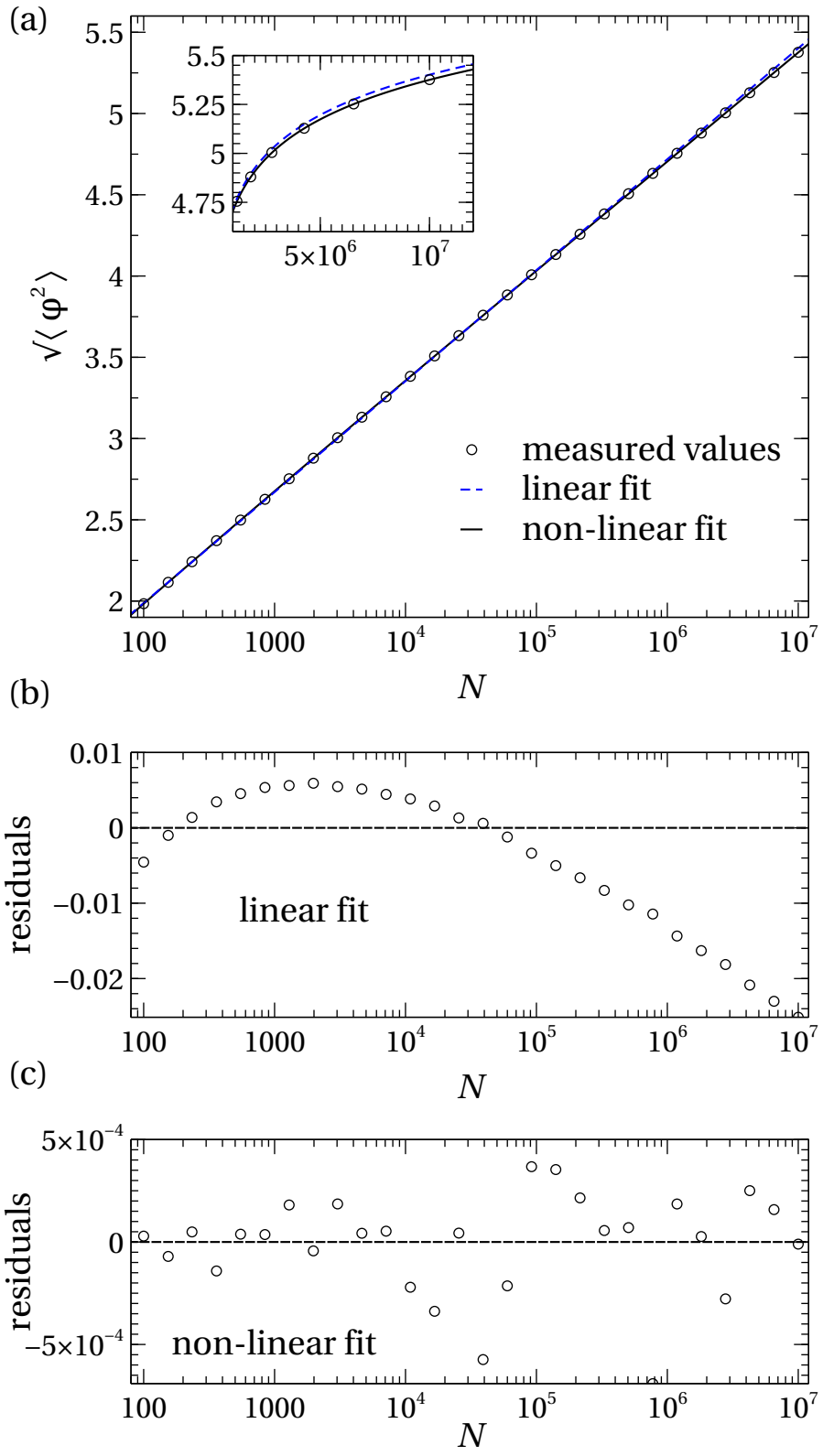

FIGURE 5.3: (a) Root mean square winding angle of a RW on a square lattice, shown as a function of the number of sites in the walk N in semi-logarithmic scale. The region with $N = 10^6 - 10^7$ is shown in the inset in linear scale. The dashed line denotes a linear fit and the solid line denotes non-linear fits [Eqs. (5.3) and (5.4)] that take into account finite size corrections. (b) Residuals of the linear fit. (c) Residuals of the non-linear fits. Note that the curves from Eqs. (5.3) and (5.4) are indistinguishable in this range of values for N.

	$d = 2$	$d = 3$
A	0.78 ± 0.03	0.69 ± 0.03
B	0.2888 ± 0.0005	0.288 ± 0.001
C	-0.321 ± 0.017	-0.357 ± 0.012
Δ	0.62 ± 0.12	0.54 ± 0.11
c_0	0.74 ± 0.006	0.63 ± 0.005
c_1	0.2894 ± 0.0003	0.2892 ± 0.0002
c_2	-0.48 ± 0.05	0.56 ± 0.04
c_3	0.33 ± 0.11	0.45 ± 0.09

TABLE 5.1: Fitting parameters from Eqs. (5.3) and (5.4) for the root mean square winding angle of RWs with N sites on square ($d = 2$) and cubic ($d = 3$) lattices.

5.1. Note that the parameter B from the fit to Eq. (5.3) is in agreement with the theoretical value of $1/\sqrt{12} \approx 0.2887$, both in dimensions $d = 2$ and $d = 3$, while c_1 from the fit to Eq. (5.4) slightly deviates from the theory. Possibly, Eq. (5.3) captures the leading order finite size corrections to $\sqrt{\langle \varphi^2 \rangle}$ more accurately.

5.3 Winding angle of planar self-avoiding walks

For long SAWs on a square lattice, the winding angle was shown to have a Gaussian distribution [Eq. (1.16)] [45]. Even before this analytical result, the winding angle was studied numerically. Fisher *et al.* [32] used exact enumeration of short (up to $N = 21$) walks and Monte Carlo simulations of SAWs with $N \leq 170$ to measure the winding angle distribution. They found that, to a good approximation,

$$\langle \varphi^2 \rangle \propto \ln N, \tag{5.5}$$

and

$$2.9 < \frac{\langle \varphi^4 \rangle}{\langle \varphi^2 \rangle^2} < 3.2, \tag{5.6}$$

which is close to the Gaussian value 3. Due to the limited computer resources at the time and the lack of an efficient algorithm to compute the winding angle of the walks, it was not possible to measure the winding angles longer SAWs and observe the convergence to the Gaussian form.

In this work, we studied the winding angles of SAWs on the square lattice with N ranging from 10^2 to 10^7. The mean square winding angle is shown as a function of N in semi-logarithmic scale in Fig. 5.4(a). The dashed line denotes a linear fit which results in

$$\langle \varphi^2 \rangle = (-2.268 \pm 0.002) + (2 \pm 0.002) \ln N. \tag{5.7}$$

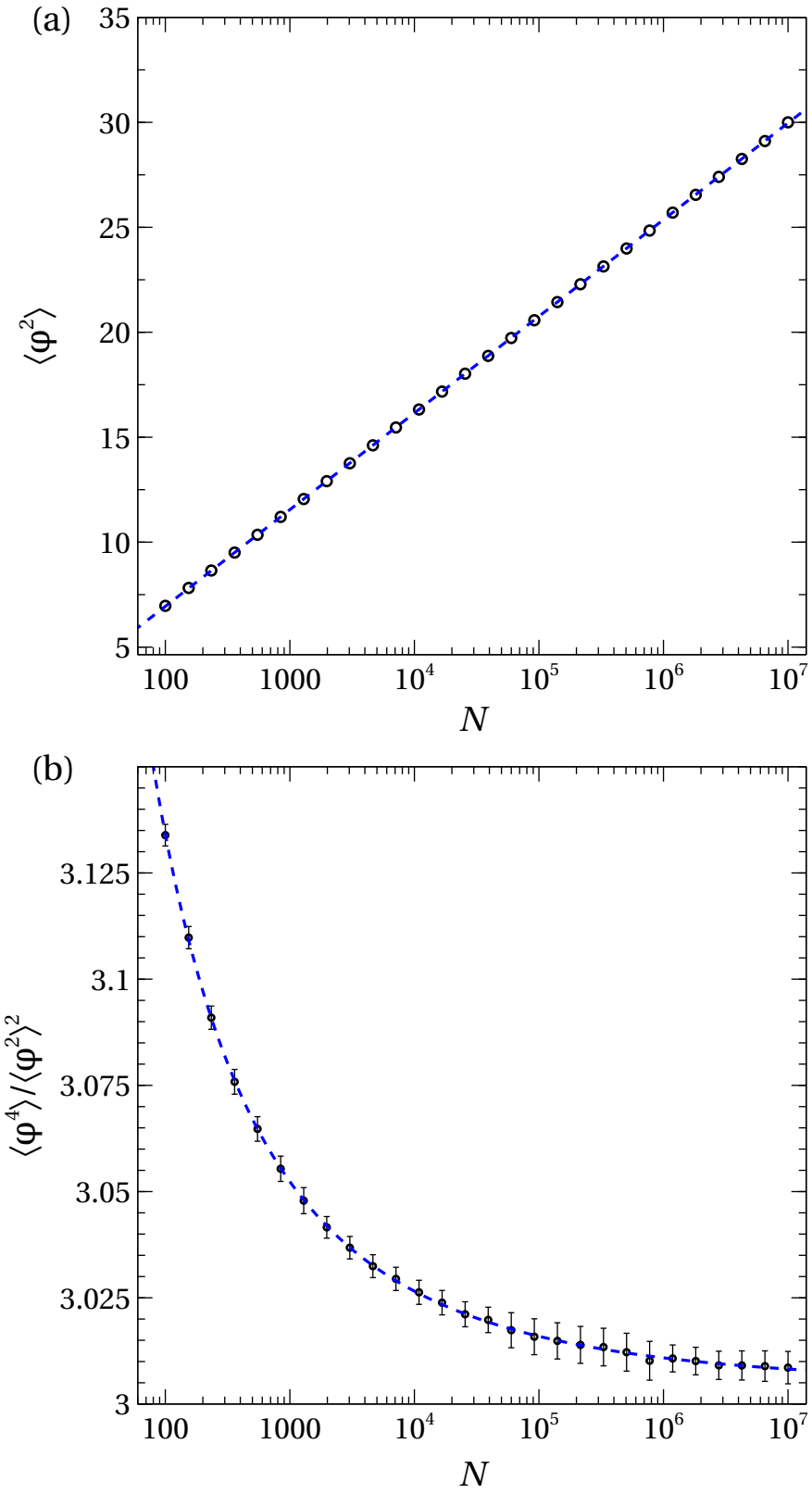

FIGURE 5.4: (a) The mean square winding angle of a SAW with N sites on a square lattice. The dashed line is a linear fit. (b) The ratio $\langle\varphi^4\rangle/\langle\varphi^2\rangle^2$ approaches the Gaussian value 3 as N increases. The dashed line denotes a non-linear fit according to Eq. (5.8)

The slope is in excellent agreement with the theoretical value [Eq. (1.16)]. Note that the linear relation holds quite well even for relatively short walks ($N \sim 10^2$). To observe finite size corrections to the Gaussian distribution of φ, we measured the ratio $\langle\varphi^4\rangle/\langle\varphi^2\rangle^2$. The results are shown in Figure 5.4(b). Note that (a) even for $N = 10^2$, $\langle\varphi^4\rangle/\langle\varphi^2\rangle^2 \approx 3.13$, not far from the Gaussian value, which is consistent with the results for the linear dependence of $\langle\varphi^2\rangle^2$ on $\log N$. (b) The small but noticeable difference from the Gaussian form converge slowly to zero. Even for walks with $N = 10^7$ we observe a non-negligible deviation from 3. To study the finite size corrections we fitted the data to the form

$$\langle\varphi^4\rangle/\langle\varphi^2\rangle^2 = A + B(\ln N)^{-1} + C(\ln N)^{-2}. \tag{5.8}$$

[This form was in slightly better agreement with the data than a function with non-integer powers like in Eq. (5.3).] The result is denoted by the dashed line in Fig. 5.4(b). We find $A = 3.0097 \pm 0.0013$, $B = -0.262 \pm 0.020$, and $C = 3.85 \pm 0.07$. Note that A is very close to the Gaussian value. The small difference is most likely a result of corrections in the form of higher powers of $1/\ln N$ that were not taken into account in Eq. (5.8).

5.4 Winding angle of self-avoiding walks on the cubic lattice

Despite the long standing interest in this problem, the exact distribution $p_N(\varphi)$ of the winding angle of a SAW with N sites around a rod in dimension $d = 3$ is unknown. The only analytical result that we know of was obtained by Rudnic and Hu [34], where they used renormalization group methods to show that in $d = 4 - \epsilon$, to first order in ϵ, $p_N(\varphi)$ follows the Gaussian distribution given in Eq. (1.17). The authors also reported a Monte Carlo simulation of SAWs with up to 910 steps, where they were only able to study the pre-asymptotic regime where RW behavior was observed. More recently, Walter *et al.* [41] utilized the improvement in computer power to study the winding angle distribution of SAWs on the cubic lattice with $N \leq 25000$. They showed that $p_N(\varphi)$ does not converge to the Gaussian form and found that $\langle\varphi^2\rangle \propto (\ln N)^{2\psi}$ where $\psi = 0.75(1)$. They also showed that $\langle\varphi^4\rangle/\langle\varphi^2\rangle^2$ converges to 3.74(5), which differs significantly from the first order ϵ-expansion prediction.

Here we extend the study to walks with N up to 10^7 to see whether the behavior that was observed in [41] persists as $N \to \infty$, or a pre-asymptotic regime has been observed.

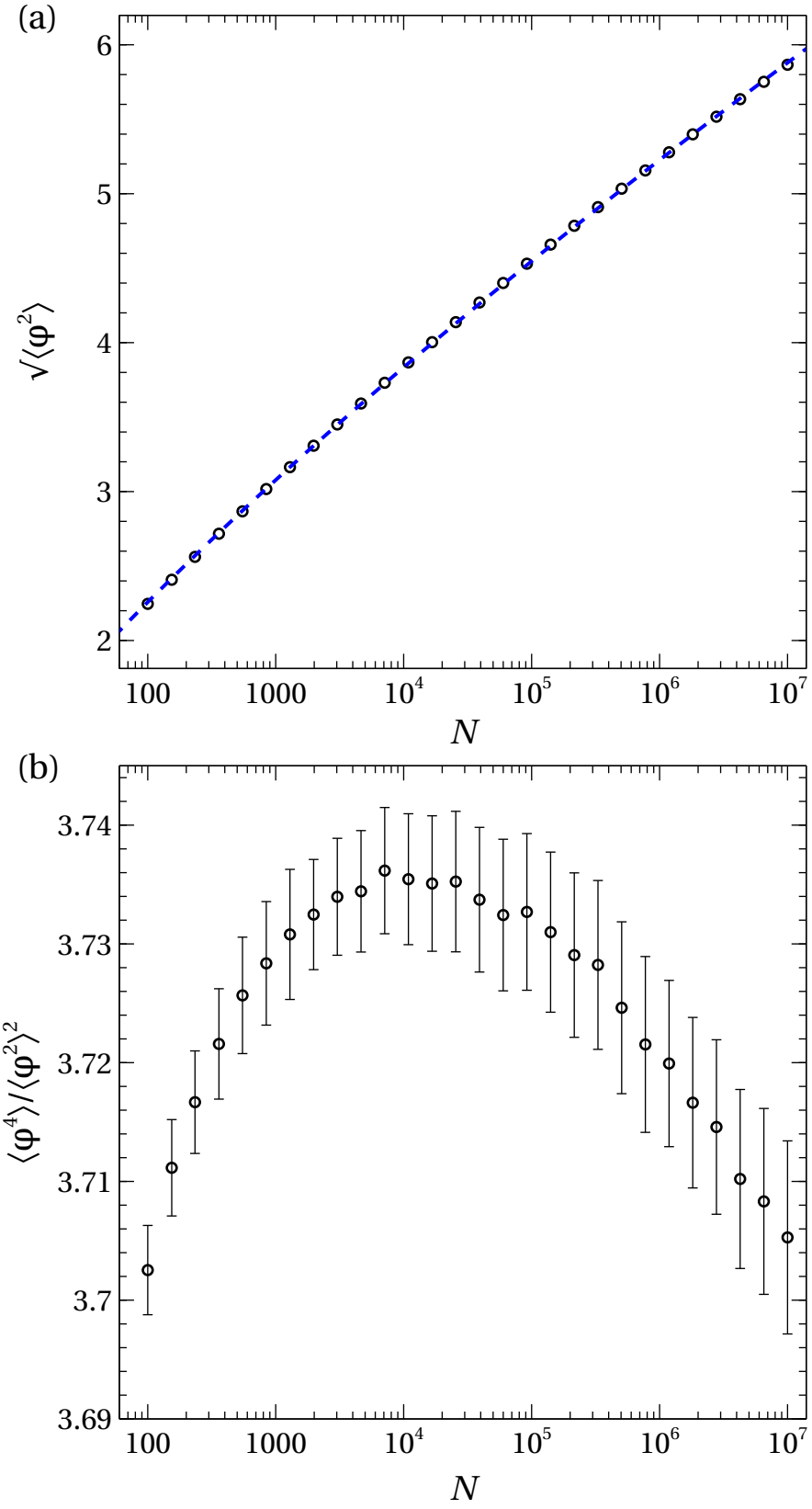

FIGURE 5.5: (a) The root mean square winding angle of a SAW with N sites on a cubic lattice. The dashed line is a power law fit. (b) The ratio $\langle\varphi^4\rangle/\langle\varphi^2\rangle$.

Our results for the root mean square winding angle of a SAW with N sites on a cubic lattice are depicted in Figure 5.5(a). The dashed line denotes a power law fit to the form

$$\sqrt{\langle\varphi^2\rangle} = A \cdot (\ln N)^{\psi}, \tag{5.9}$$

that resulted in $A = 0.703 \pm 0.004$ and $\psi = 0.764 \pm 0.003$. Note that ψ extracted from our data is in agreement with the result in [41]. The ratio $\langle\varphi^4\rangle/\langle\varphi^2\rangle^2$ from our simulation is shown in Figure 5.5(b). Note the *non-monotonic* dependence of $\langle\varphi^4\rangle/\langle\varphi^2\rangle^2$ on the number of sites in the walk. We find that it reaches a maximum value of 3.73 ± 0.01 for $N \approx 10^4$ (in agreement with the result in [41]) and then decreases as the walks increase in size. For $N = 10^7$ we find $\langle\varphi^4\rangle/\langle\varphi^2\rangle = 3.705 \pm 0.008$, still far from the Gaussian value 3 predicted from first order ϵ-expansion [34]. The non-monotonic behavior is quite surprising, since we do not have a reason to expect that $\langle\varphi^4\rangle/\langle\varphi^2\rangle^2$ will reach its maximum value around $N = 10^4$. This behavior might indicate a cross-over from a non-asymptotic regime at finite N to the asymptotic regime at infinite N. One possible reason for such a cross-over can be the influence of the lattice on which the walks are created. In Figure 5.6 we present the winding angle distribution of SAWs on a cubic lattice for N ranging from 10^4 to 10^7. For $N = 10^4$ the lattice structure is evident in the distribution $p_N(\varphi)$, where narrow peaks are observed at specific angles corresponding to lattice sites close to the z axis. This effect is diminished significantly when N increases, and the peaks in the distribution are not observable in our simulation for $N = 10^7$. In Figure 5.6(b) we show that $p_N(\varphi)$ for different N collapse to a single curve when φ is scaled by $(\ln N)^{0.76}$, in agreement with the results in [41] and with the behavior shown in Figure 5.5. Note that the effects of the lattice structure were not evident in Figures 8 and 9 in [41] due to the coarse binning in those graphs (The bin width in the histograms was 0.5 radians, compared to $\pi/1000$ in our graphs.).

5.5 The Gaussian argument

The Gaussian form of the winding angle distribution given in Eq. (1.16) can be explained by the following simple argument [38, 32]: Starting from the first step, the SAW can be divided into segments of lengths $1, 2, 4, ..., 2^m \approx N/2$. The i-th segment has 2^i steps, and starts after approximately 2^i steps of the walk. Thus both its linear size and its distance from the origin are typically of the order of $2^{i\nu}$, where $\nu = 3/4$ for SAWs in $d = 2$ [22]. The winding angle of each segment is then expected to be of order one. The total winding angle of the walk is approximately

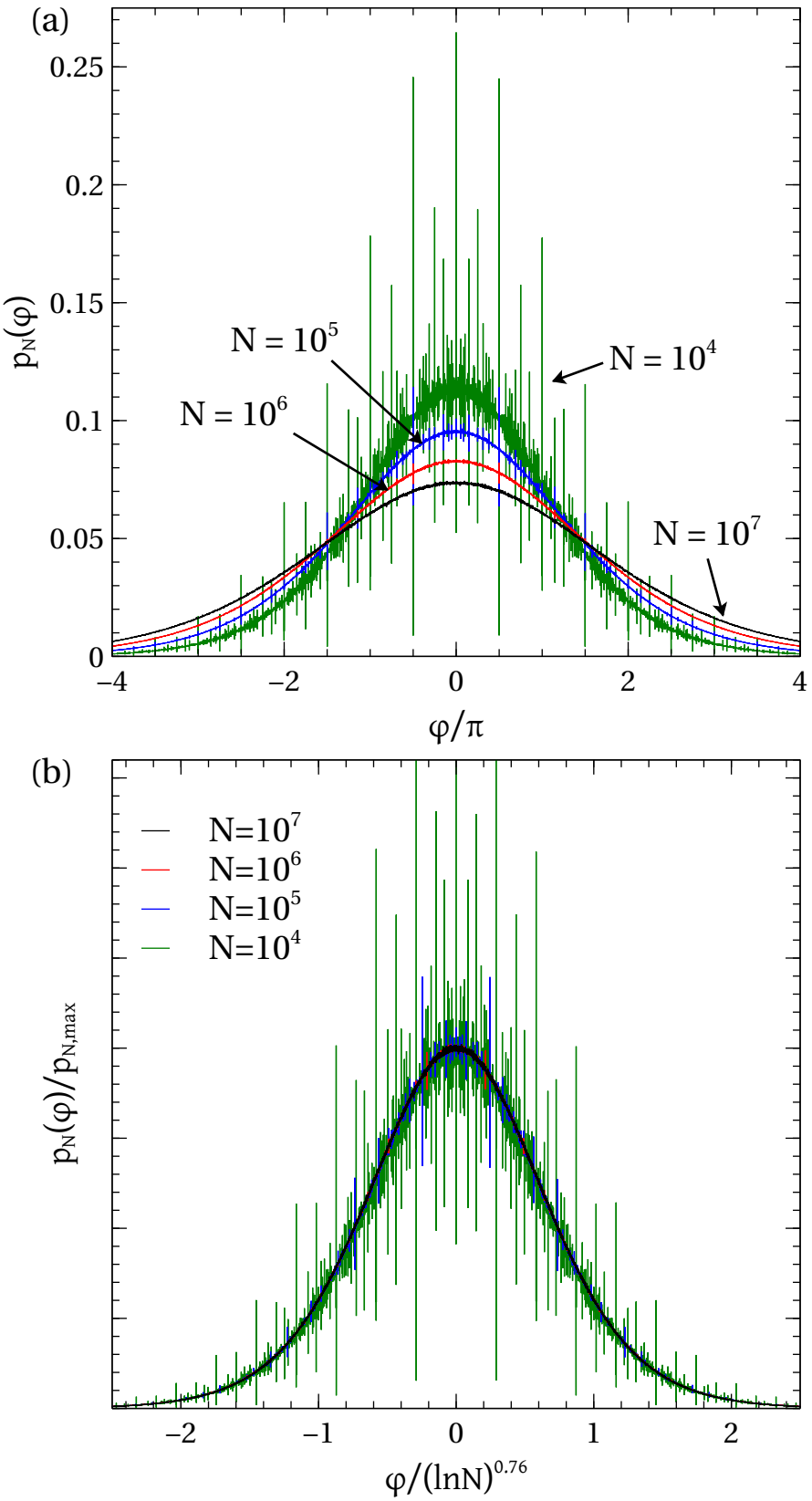

FIGURE 5.6: (a) Winding angle distribution of a SAW with N steps on a cubic lattice. (b) The distribution divided by the maximal value, as a function of scaled angle.

the sum of the changes in the winding angles of these individual segments, i.e.,

$$\varphi = \sum_i \Delta\varphi_i. \tag{5.10}$$

The SAW is a self-similar object, and it is expected that the properties of the smaller segments are identical to those of the larger segment when they are scaled down to the same size. Thus, the angles $\Delta\varphi_i$ have identical distributions. Under the assumption that they are independent, and with a finite variance, the central limit theorem states that in the limit of large m, φ will have a Gaussian distribution with a variance proportional to $m \propto \ln N$.

In [38] it was mentioned that this argument fails when it is applied to RWs since a RW is allowed to return to the vicinity of the excluded center, while a SAW in $d = 2$ cannot return to the origin without self-intersection. In fact in $d = 2$ the size of the effective excluded area is of the order of the segment size, and upon rescaling those properties remain unchanged. For a RW, the size of the excluded center has the size of a lattice cell for any segment size. We suspect that this is also the reason why the Gaussian argument fails for SAWs in $d = 3$.

In order to understand the behavior of SAW in $d = 3$ we studied their return to an infinite cylinder of radius r centered on the z axis. [The SAW tree allows very fast intersection tests between the walk and a the cylinder, that take time no longer than $O(\ln N)$ [83]]. In Figure 5.7 we present the probability $P_r(n)$ that the site n in a SAW of N steps will be inside a cylinder of radius r. Note that in this simulation these cylinders are not excluded regions like the infinite line $x = y = 0$ and we use them simply to check if the walk is wandering close to the excluded center. In Figure 5.7(a) we depict on a logarithmic scale $P_r(n)$ as a function of n for several sizes r and several total lengths N of the SAWs. We note that for fixed r the data points of larger Ns nicely continue the trend of the smaller Ns. This is true apart from a small increase in $P_r(n)$ near the end of the walk (as $n \sim N$). This increase implies that the probability for the site n to be inside the cylinder is reduced by the presence of a *finite* part of the walk subsequent to n, and when this part is not present (near the end of the walk) it is easier for the walk to return to the cylinder. All graphs have $P_r(n) \approx 1$ until the size of the segment of the walk $an^\nu \sim r$, and then decay with a slope of about -1.2. This decay is slow but converging in the sense that in the asymptotic limit (when $N \to \infty$) only a finite number of sites will be in the cylinder. In Figure 5.7(b) we show that these curves collapse when P_r is plotted against the scaled position $n/r^{1/\nu}$. This collapse demonstrates that when a long walk is scaled down, the statistics of the walk in a cylinder around the z axis

correspond to those of a smaller cylinder, with reduced radius. The rescaling in Figure 5.7(b) does not change the size of the excluded line, but the collapse of varying cylinder radius to the same curve indicate that if we take a segment of a SAW and scale it down, it does not correspond to an earlier (smaller) segment but correspond to the behavior of a SAW with a smaller excluded center. Thus, its winding angle distribution will not be identical to that of a preceding segment and will, probably, have a larger variation $\Delta\varphi$.

By rotating the SAW tree we can divide the walk into segments of differing sizes in the simulation. For SAWs with $N = 2^{23}$ in $d = 2, 3$, we measured the winding angles of segments of sizes $128, 256, ..., 2^{22}$, starting from the origin (i.e, the size of the i segment was 64×2^i). The change in the winding angle $\Delta\varphi_i$ and the correlation between the changes of different segments were measured. In both $d = 2$ and $d = 3$, we find that the correlation between the different segments is very weak (Pearson correlation smaller than 0.05). Thus, to a good approximation, $\Delta\varphi_i$ can be considered as independent of each other. In Figure 5.8 we present the variances of the individual segments. The first segment was omitted from the graph since it scales differently than the others (The first segment starts at the origin and does not have a preceding segment that is half its size.). As expected, in $d = 2$, the variance of the different segments is constant. We find that it equals 0.75 as denoted by the dashed line in Figure 5.8. In $d = 3$, we see that the variance of the winding angle increases as i increases, as we predicted earlier. The solid line in Figure 5.8 denotes a power law growth of $\langle\Delta\varphi_i^2\rangle \sim i^{0.52}$, which is consistent with the results of the previous section. (Due to the small range of i and some arbitrariness in the numbering of the segments, the error in this exponent can be as large as 0.1.) Under the assumption that the winding angles of the different segments are independent,

$$\langle\varphi^2\rangle \approx \int_1^m \langle\Delta\varphi_i^2\rangle di \propto m^{1.52} \propto (\ln N)^{1.52}. \tag{5.11}$$

5.6 Summary and discussion

The method described in Section 5.1 to compute the winding angle relies on the fact that some properties of a lattice walk can be deduced from aggregate information about large sections that constitute the walk, without knowing its small scale details. This approach can be useful in various situations. For example, it is possible to perform fast intersection tests of a SAW with various surfaces (as we did in Chapter 4 and was done in [88]). This can be used in future studies to

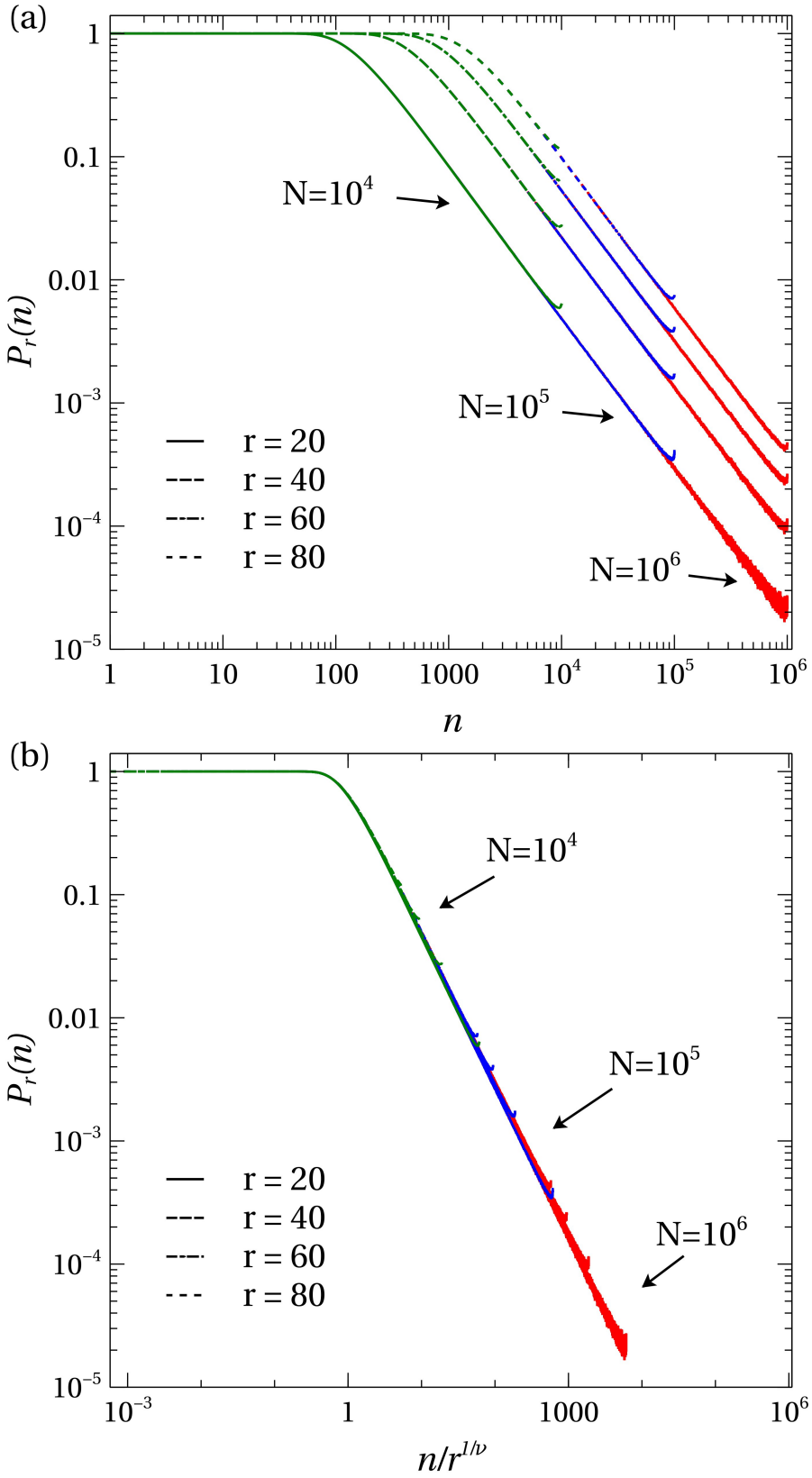

FIGURE 5.7: Probability of the n site in a SAW with N steps on the cubic lattice to be inside a cylinder of radius r around the z axis.

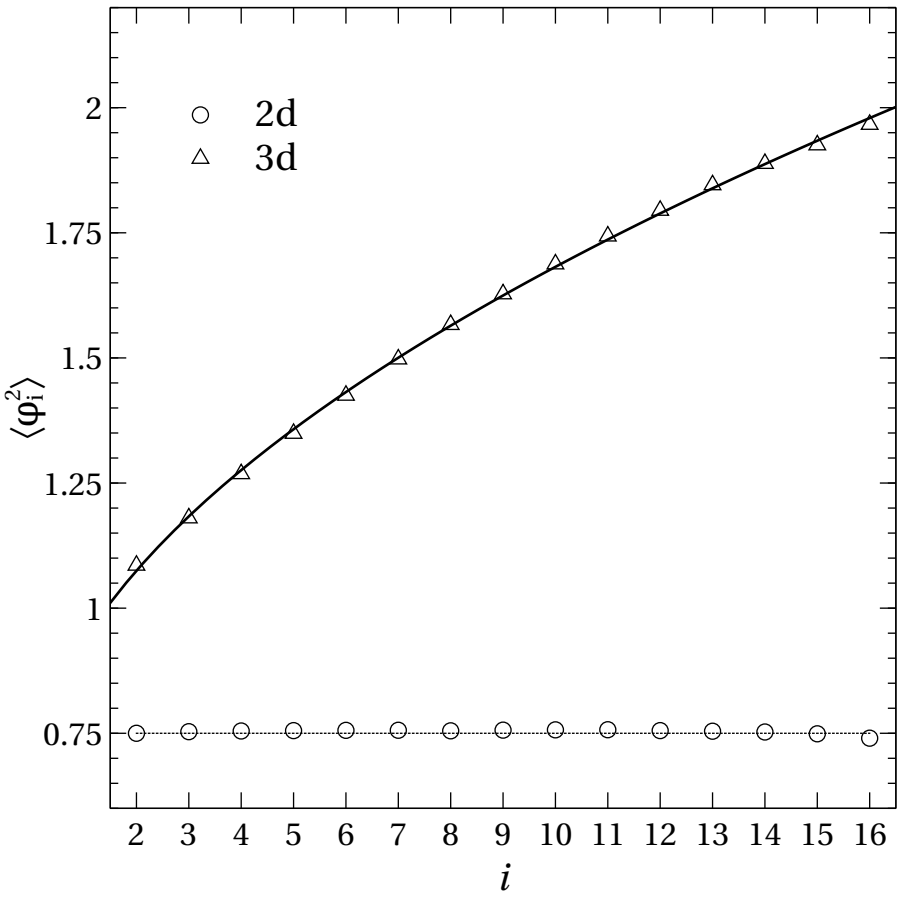

FIGURE 5.8: The change in the winding angle of of a SAWs on square ($d = 2$) and cubic ($d = 3$) lattices for segments of the walk of sizes $64 * 2^i$, starting from the beginning of the walk. The first segment ($i = 1$) was omitted from the graph. For SAWs in $d = 2$, $\langle \Delta\varphi_i^2 \rangle$ is approximately 0.75 for all segments (dashed line), while for SAWs in $d = 3$, $\langle \Delta\varphi_i^2 \rangle$ increases with i. The solid line represents a power law increase of $\langle \Delta\varphi_i^2 \rangle \sim i^{0.52}$.

measure the distribution $p(\varphi)$ of the winding angle of long walks near excluded regions of different shapes and sizes. Specifically, it would be interesting to know how a smaller radius of the excluded center increases the winding angle of a SAW.

By studying RWs and SAWs with the number of sites N ranging up to 10^7, we were able to verify theoretical predictions about $p(\varphi)$ and its dependence on N, and observe the effect of finite size corrections. For RWs, we showed that as $N \to \infty$, $\sqrt{\langle\varphi^2\rangle}$ is linear in $\ln N$ with the predicted slope $1/\sqrt{12}$, apart from finite size corrections [Eqs. (5.3) and (5.4)].

For SAWs on the square lattice, we showed that the ratio $\langle\varphi^4\rangle/\langle\varphi^2\rangle^2$ approaches Gaussian value 3, as is predicted by the theory, with a small correction that decays slowly as N increases.

For SAWs on the cubic lattice, we observed non-monotonic dependence of $\langle\varphi^4\rangle/\langle\varphi^2\rangle^2$ on N. This surprising result shines a different light on the previous result by Walter *et al.* [41], where it was shown that for SAWs with $N \leq 25000$, $\langle\varphi^4\rangle/\langle\varphi^2\rangle^2$ converges to a constant value of 3.74(5) as N is increased. (We show that this is in fact approximately the maximum value of $\langle\varphi^4\rangle/\langle\varphi^2\rangle^2$.) This behavior might indicate a cross-over from a non-asymptotic regime to the asymptotic behavior in the limit $N \to \infty$. It is possible that the cross-over is related to the structure of the lattice. We showed that the lattice structure is evident in the winding angle distribution even for walks with $N = 10^5$ and diminishes for larger walks.

In Section 5.5 we demonstrated that the square winding angle of a SAW in $d = 3$ can be obtained from the summation of the square change in the winding angles of $m \propto \ln N$ independent segments of the walk. Unlike the situation in $d = 2$, where these segments have identical mean square winding angles, in $d = 3$ the mean square winding angle of the i segment increases approximately as $i^{0.52}$, which leads to an increase of the total square winding angle proportional to $(\ln N)^{1.52}$, as was measured here and in [41]. We stipulate that the increase in the winding angle of the individual segments can be explained by the fact that when the segment are scaled down to the same size, the excluded center is also effectively scaled down, and thus the winding angle is increased.

To summarize, by using the improved implementation of the pivot algorithm, we have increased the size of polymers in the simulation by several orders of magnitude. This enabled us to observe interesting and unexpected behavior of the winding angle of SAWs in $3d$. The scaling behavior observed in Section 5.5 for $3d$ SAWs is not currently understood analytically and demands further study.

Chapter 6

Concluding Remarks

In this Thesis we investigated the equilibrium properties of long polymers in SF spaces. Even though the equilibrium properties of polymers, in free and confined spaces, have been the subject of numerous studies in over half a century, there are still fundamental problems that remain unsolved. These include the end-point distribution of a polymer in good solvent and the winding angle distribution of a polymer around a rod.

These equilibrium properties constitute important building blocks in our understanding of out-of-equilibrium processes such as the self assembly of complex biological molecules. For example, the natural extension of the problem of a polymer winding around a rigid rod is the winding of a polymer around a flexible rod (or another polymer), where structures like the famous double helix can be formed. Thus it is valuable, from time to time, to return to the elementary problems in polymer physics and apply new numerical and analytical methods in their study (such as the new implementation of the pivot algorithm used in Chapters 4 and 5).

In Chapters 2 and 4 we studied the properties of polymers in SF spaces where the geometry of the system included a single defining parameter α, the opening angle of the cone or wedge. This property enables the study of the universal properties of the system as they vary in a continuous way. We found that in some cases, a single universal feature controls several, seemingly unrelated properties of the polymer. For example, for IPs the exponent η controls the amplitude of the force applied on the surface, the short and long range behavior of the pressure and the monomer density, and the mean extension of the polymer with respect to its conformations in free space. In our simulations (that were not reported in this work), we find that the electric field like property of IPs found in Chapter 2, where the pressure diverges near the corner of the surface, seems to carry over to polymers in good solvent. However, at this point, we do not know if the exponent η controls the power law form of the pressure and the density in that case for short and long distances, as it does

for IPs. This point deserves further study. The highly efficient implementation of pivot algorithm due to Clisby [2] used in Chapters 4 and 5 will allow a detailed numerical study of these properties in the future. When such a study is performed in a lattice model for polymers, it will be important to pay close attention to the lattice definitions of local properties like the entropic pressure. As we have seen in Chapter 3, lattice models of polymers exhibit non-trivial differences from continuous models, and one has to make sure that the physical properties are consistent with the continuous description of the system and with reasonable physical assumptions (such as the arrival at the total force on a surface after integrating the local pressure on it).

In Chapter 4 we reported a deviation of the angular distribution of the end-point of planar SAWs attached to wedges from the theoretical predictions that rely on conformal field theory (CFT) [77]. The two-dimensional case is relevant in experiments involving grafted polymers. It has been shown for example that single stranded DNA, when adsorbed on modified graphite surface [112], exhibits scaling properties of a self-avoiding walk on a plane. The use of CFT results in polymer physics is based on the mapping between magnetic and polymer systems [Eq. (1.6)]. Possibly, the deviation from the theory is related to the fact that Eq. (1.6) connects the magnetic system in the canonical ensemble to the polymer system in the *grand canonical* ensemble, where N is not fixed. In our simulations, as in many physical situations, the polymers are in the canonical ensemble with a fixed N. It would be interesting to perform further study on the equivalence of ensembles in the polymer system with respect to end-point distributions in free and confined spaces.

The behavior of the winding angle of a polymer around a line seen in Chapter 5 opens the door to further study of the problem. As we have seen in Section 5.5, the total winding angle of the walk can be approximated as the sum of the winding angles of independent segments. We have stipulated that the different square winding angles of the segments can be explained from the change in the volume of the excluded center observed by each segment when they are scaled to the same size. It would be interesting to study the winding angle of polymers around centers of different sizes, and see if the dependence of the winding angles on the size of the excluded center is consistent with our explanation. Moreover, one can study the winding of polymers around SF surfaces like the ones considered in Chapters 2 and 4, that are invariant under rescaling, and observe the behavior of the winding angles of the segments. The methods reported in Chapters 4 and 5 are most suitable for this kind of research.

Thus, there are several open questions that arise from the work in this Thesis that should be studied in the future. In this work, we have developed the tools that will enable such a research.

Appendix A

Derivation of the Monomer Density of an Ideal Polymer for $N \to \infty$

In the calculation of the monomer density and the entropic pressure we examined separately the contribution of different parts of the polymer. The monomer density in the limit $N \to \infty$ is given by

$$\rho(\mathbf{h},\mathbf{r}) = \lim_{N\to\infty} \int_{n=0}^{N} G(\mathbf{h},\mathbf{r},n) Z(\mathbf{r},N-n) dn / Z(\mathbf{h},N). \tag{A.1}$$

In order to evaluate this integral we select the ratio $x_1 = n_1/N$ such that $0 < x_1 \ll 1$ and split the integral in Eq. (A.1),

$$\begin{aligned} \rho(\mathbf{h},\mathbf{r}) &= \lim_{N\to\infty} \left\{ \left(\int_0^{n_1} + \int_{n_1}^{N-n_1} + \int_{N-n_1}^{N} \right) G(\mathbf{h},\mathbf{r},n) Z(\mathbf{r},N-n) dn / Z(\mathbf{h},N) \right\} \\ &= \lim_{N\to\infty} \left\{ N \left(\int_0^{x_1} + \int_{x_1}^{1-x_1} + \int_{1-x_1}^{1} \right) G(\mathbf{h},\mathbf{r},n) Z(\mathbf{r},N-n) dx / Z(\mathbf{h},N) \right\}, \end{aligned} \tag{A.2}$$

where we have changed the variable of integration to $x = n/N$. Using the scaling properties of the functions G and Z for large N (G scales as in Eq. (2.26) and $Z(\mathbf{h},N) = \left(h/\sqrt{DN}\right)^{\eta} \Theta(\hat{\mathbf{h}})$ as in Eq. (2.16)), we see that in the limit $N \to \infty$, for $n_1 < n < N - n_1$,

$$\begin{aligned} G(\mathbf{h},\mathbf{r},n) &\propto \left(\frac{1}{N}\right)^{d/2+\eta} G^*(\mathbf{h},\mathbf{r},x), \\ Z(\mathbf{r},N-n) &\propto \left(\frac{1}{N}\right)^{\eta/2} Z^*(\mathbf{r},1-x), \end{aligned}$$

where Z^* and G^* do not depend on N. Therefore,

$$N \int_{x_1}^{1-x_1} G(\mathbf{h}, \mathbf{r}, n) Z(\mathbf{r}, N-n) dx / Z(\mathbf{h}, N) \propto \left(\frac{1}{N}\right)^{d/2+\eta-1} \to 0.$$

Since for $x \to 1$ the partition function $Z(\mathbf{r}, N-n) \to 1$ and becomes independent of N, and it is always smaller than one (it is the survival probability of a random walker), in the same limit,

$$N \int_{1-x_1}^{1} G(\mathbf{h}, \mathbf{r}, n) Z(\mathbf{r}, N-n) dx / Z(\mathbf{h}, N) \propto \left(\frac{1}{N}\right)^{d/2+\eta/2-1} \to 0.$$

Only the first part of the polymer will contribute to the monomer density in the limit of an infinitely long polymer, as described in the main text, and will lead to density in Eq. (2.36).

Appendix B

Green and Partition Function for Ideal Polymers in Various Geometries

Below we list the exact solutions of Eq. (2.7) that were used to derive the results in Chapter 2. These solutions were taken from [113].

B.1 Wedge in $d = 2$

The wedge defined in Figure 2.5(a) is described in polar coordinates by $-\alpha < \theta < \alpha$. The exact solution of equation (2.7) is [113]

$$G(r', \theta', r, \theta, N) = \frac{1}{2\alpha DN} \exp\left(-\frac{r^2 + r'^2}{4DN}\right) \sum_{i=1}^{\infty} I_{\eta_i}\left(\frac{rr'}{2DN}\right) \cos(\eta_i \theta) \cos(\eta_i \theta'), \tag{B.1}$$

where

$$\eta_i = \frac{i\pi}{2\alpha}, \quad i = 1, 2, 3, \ldots \tag{B.2}$$

and I_{η_i} is the modified Bessel function of the first kind. The partition function can be found by integrating Eq. (B.1):

$$\begin{aligned} Z(r', \theta', N) &= \int G(r', \theta', r, \theta, N) r dr d\theta \qquad \text{(B.3)} \\ &= \frac{r'}{\sqrt{\pi DN}} \exp\left(-\frac{r^2}{8DN}\right) \times \\ &\quad \sum_{i=1}^{\infty} \frac{1}{i} \left[I_{\frac{\eta_i - 1}{2}}\left(\frac{r'^2}{8DN}\right) + I_{\frac{\eta_i + 1}{2}}\left(\frac{r'^2}{8DN}\right) \right] \sin^2\left(\frac{\pi i}{2}\right) \cos\left(\eta_i \theta'\right). \end{aligned}$$

B.2 Wedge in $d = 3$

The solution in $d = 3$ is obtained by multiplying the Green function of a wedge in $d = 2$ by the free space propagator in $d = 1$, leading to

$$G(r', \theta', z', r, \theta, z, N) = \frac{1}{4\alpha\pi^{1/2}(DN)^{3/2}} \exp\left(-\frac{(z-z')^2}{4DN}\right) \times \sum_{i=1}^{\infty} \exp\left(-\frac{r^2+r'^2}{4DN}\right) I_{\eta_i}\left(\frac{rr'}{2DN}\right) \cos(\eta_i\theta') \cos(\eta_i\theta). \tag{B.4}$$

Integrating Eq. (B.4) one can immediately see that the partition function for the wedge in $d = 3$ does not depend on the z coordinate. In fact it is identical with the partition function for the wedge in $d = 2$ in Eq. (B.3).

B.3 Circular cone

A circular cone in $d = 3$ is defined in spherical coordinates by $\theta < \alpha$ [Figure 2.3(c)]. The solution to Eq. (2.7) in the cone is [113]

$$G(r', \theta', \phi', r, \theta, \phi, N) = -\frac{1}{4\pi DN\sqrt{rr'}} \exp\left(-\frac{r^2+r'^2}{4DN}\right) \sum_{i=1}^{\infty} \left\{ I_{\eta_i+1/2}\left(\frac{rr'}{2DN}\right) (2\eta_i+1) \times \sum_{m=0}^{\infty} (2-\delta_{m,0}) P_{\eta_i}^{-m}(\mu) P_{\eta_i}^{-m}(\mu') \cos(m(\phi-\phi')) \left[(1-\mu_0)^2 \frac{\partial}{\partial\mu} P_{\eta_i}^{-m}(\mu_0) \frac{\partial}{\partial\eta} P_{\eta_i}^{-m}(\mu_0)\right]^{-1} \right\}, \tag{B.5}$$

where P_η^{-m} are associated Legendre functions, $\mu = \cos\theta$, $\mu_0 = \cos\alpha$ and η_i are the roots of the equation $P_\eta(\mu_0) = 0$ in ascending order. The Green function is somewhat simpler when the starting point of the polymer is along the symmetry axis of the cone, i.e., $\theta' = 0$. In this case the solution does not depend on the azimuthal angle ϕ'. Denoting $r' = h$, we get

$$G(h, r, \theta, N) = -\frac{1}{4\pi DN\sqrt{hr}} \exp\left(-\frac{r^2+h^2}{4DN}\right) \sum_{i=1}^{\infty} \frac{I_{\eta_i+1/2}\left(\frac{rh}{2DN}\right)(2\eta_i+1) P_{\eta_i}(\mu)}{(1-\mu_0^2)\frac{\partial}{\partial\mu} P_{\eta_i}(\mu_0) \frac{\partial}{\partial\eta} P_{\eta_i}(\mu_0)}. \tag{B.6}$$

The partition function can be found for any $\mathbf{r}'$ by integrating Eq. (B.5),

$$\begin{aligned} Z(r',\theta',N) &= \int r^2 \sin\theta G(r',\theta',\phi',r,\theta,\phi,N) dr d\theta d\phi \qquad \text{(B.7)} \\ &= e^{-\frac{r'^2}{4DN}} \sum_{i=1}^{\infty} \left\{ \Gamma\left(\frac{3+\eta_i}{2}\right) {}_1\tilde{F}_1\left(\frac{3+\eta_i}{2}, \frac{3}{2}+\eta_i, \frac{r'^2}{4DN}\right) P_{\eta_i}(\mu) \left(\frac{r'^2}{4DN}\right)^{\eta_i/2} \times \right. \\ &\quad \left. \frac{P_{\eta_i+1}(\mu_0) - P_{\eta_i-1}(\mu_0)}{(1-\mu_0)^2 \frac{\partial}{\partial\mu} P_{\eta_i}(\mu_0) \frac{\partial}{\partial\eta} P_{\eta_i}(\mu_0)} \right\}, \end{aligned}$$

where ${}_1\tilde{F}_1$ is the regularized confluent hypergeometric function [82]. Note that due to the cylindrical symmetry Z does not depend on the azimuthal angle ϕ'.

Bibliography

[1] K. C. Neuman, T. Lionnet, and J. F. Allemand. "Single-molecule micromanipulation techniques". *Annu. Rev. Mater. Res.* **37** (2007), p. 33.

[2] N. Clisby. "Efficient implementation of the pivot algorithm for self-avoiding walks". *J. Stat. Phys.* **140** (2010), p. 349.

[3] D. H. Napper. *Polymeric stabilization of colloidal dispersions*. New York: Academic Press, 1984.

[4] O. Azzaroni. "Polymer brushes here, there, and everywhere: Recent advances in their practical applications and emerging opportunities in multiple research fields". *J. Polym. Sci. Part A Polym. Chem.* **50** (2012), p. 3225.

[5] M. Krishnamoorthy, S. Hakobyan, M. Ramstedt, and J. E. Gautrot. "Surface-initiated polymer brushes in the biomedical field: applications in membrane science, biosensing, cell culture, regenerative medicine and antibacterial coatings." *Chem. Rev.* **114** (2014), p. 10976.

[6] A. A. Deniz, S. Mukhopadhyay, and E. A. Lemke. "Single-molecule biophysics: at the interface of biology, physics and chemistry." *J. R. Soc. Interface* **5** (2008), p. 15.

[7] J. T. Hyotyla and R. Y. H. Lim. "Atomic force microscopy". *Supramol. Chem.* Ed. by J. W. Steed and P. A. Gale. Chichester, UK: John Wiley & Sons, Ltd, 2012, p. 1.

[8] B. Cappella and G. Dietler. "Force-distance curves by atomic force microscopy". *Surf. Sci. Rep.* **34** (1999), p. 1.

[9] A. Kishino and T. Yanagida. "Force measurements by micromanipulation of a single actin filament by glass needles." *Nature* **334** (1988), p. 74.

[10] M. S. Z. Kellermayer. "Visualizing and manipulating individual protein molecules." *Physiol. Meas.* **26** (2005), R119.

[11] C. Gosse, V. Croquette, S. Gosse, and V. Croquette. "Magnetic tweezers: micromanipulation and force measurement at the molecular level". *Biophys. J.* **82** (2002), p. 3314.

[12] S. Hormeño and J. R. Arias-Gonzalez. "Exploring mechanochemical processes in the cell with optical tweezers". *Biol. Cell* **98** (2006), p. 679.

[13] R. Lipowsky. "Flexible membranes with anchored polymers". *Colloids Surfaces A Physicochem. Eng. Asp.* **128** (1997), p. 255.

[14] M. Breidenich, R. R. Netz, and R. Lipowsky. "The shape of polymer-decorated membranes". *Europhys. Lett.* **49** (2000), p. 431.

[15] J. Z. Y. Chen. "Model of a polymer chain adsorbed to a soft membrane surface". *Phys. Rev. E* **82** (2010), p. 060801.

[16] Z. Farkas, I. Derényi, and T. Vicsek. "DNA uptake into nuclei: numerical and analytical results". *Journal of Physics: Condensed Matter* **15** (2003), S1767.

[17] C. Bustamante, Z. Bryant, and S. B. Smith. "Ten years of tension: single-molecule DNA mechanics." *Nature* **421** (2003), p. 423.

[18] M. F. Maghrebi, Y. Kantor, and M. Kardar. "Entropic force of polymers on a cone tip". *EPL (Europhysics Lett.* **96** (2011), p. 66002.

[19] M. F. Maghrebi, Y. Kantor, and M. Kardar. "Polymer-mediated entropic forces between scale-free objects". *Phys. Rev. E* **86** (2012), p. 061801.

[20] M. Kardar. *Statistical physics of fields*. Cambridge: Cambridge University Press, 2007.

[21] L. P. Kadanoff. *Statistical physics: statics, dynamics and renormalization*. Singapore: World Scientific, 2000.

[22] P.-G. de Gennes. *Scaling concepts in polymer physics*. Ithaca, New York: Cornell University Press, 1979.

[23] N. Madras and G. Slade. *The self-svoiding walk*. Boston: Birkhauser, 1996.

[24] A. Karim, S. K. Satija, J. F. Douglas, J. F. Ankner, and L. J. Fetters. "Neutron reflectivity study of the density profile of a model end-grafted polymer brush: Influence of solvent quality." *Phys. Rev. Lett.* **73** (1994), p. 3407.

[25] S. Caracciolo, M. S. Causo, and A. Pelissetto. "High-precision determination of the critical exponent gamma for self-avoiding walks". *Phys. Rev. E* **57** (1998), R1215.

[26] N. Clisby. "Accurate estimate of the critical exponent ν for self-Avoiding walks via a fast implementation of the pivot algorithm". *Phys. Rev. Lett.* **104** (2010), p. 055702.

[27] K. Binder. "Critical behaviour at surfaces". *Phase Transitions Critical Phenomena, Vol. 8*. Ed. by C. Domb and J. L. Lebowitz. London: Academic Press, 1983, p. 2.

[28] J. M. Hammersley and S. G. Whittington. "Self-avoiding walks in wedges". *J. Phys. A. Math. Gen.* **18** (1985), p. 101.

[29] F. Spitzer. "Some theorems concerning 2-dimensional Brownian motion". *Trans. Am. Math. Soc.* **87** (1958), p. 187.

[30] S. F. Edwards. "Statistical mechanics with topological constraints: I". *Proc. Phys. Soc.* **91** (1967), p. 513.

[31] P. Messulam and M. Yor. "On D. Williams' "Pinching Method" and some applications". *J. London Math. Soc.* **s2-26** (1982), p. 348.

[32] M. E. Fisher, V. Privman, and S. Redner. "The winding angle of planar self-avoiding walks". *J. Phys. A. Math. Gen.* **17** (1984), p. L569.

[33] J. Rudnick and Y. Hu. "The winding angle distribution of an ordinary random walk". *J. Phys. A. Math. Gen.* **20** (1987), p. 4421.

[34] J. Rudnick and Y. Hu. "Winding angle of a self-avoiding random walk". *Phys. Rev. Lett.* **60** (1988), p. 712.

[35] C. Bélisle. "Windings of random walks". *Ann. Prob.* **17** (1989), p. 1377.

[36] C. Bélisle and J. Faraway. "Winding angle and maximum winding angle of the two-dimensional random walk". *J. Appl. Probab.* **28** (1991), pp. 717.

[37] H. Saleur. "Winding-angle distribution for Brownian and self-avoiding walks". *Phys. Rev. E* **50** (1994), p. 1123.

[38] B. Drossel and M. Kardar. "Winding angle distributions for random walks and flux lines". *Phys. Rev. E* **53** (1996), p. 5861.

[39] K. Samokhin. "Winding of a two-dimensional Brownian particle in a random environment". *J. Phys. A. Math. Gen.* **31** (1998), p. 9455.

[40] A. Grosberg and H. Frisch. "Winding angle distribution for planar random walk, polymer ring entangled with an obstacle, and all that: Spitzer–Edwards–Prager–Frisch model revisited". *J. Phys. A. Math. Gen.* **36** (2003), p. 8955.

[41] J.-C. Walter, G. T. Barkema, and E. Carlon. "The equilibrium winding angle of a polymer around a bar". *J. Stat. Mech. Theory Exp.* **2011** (2011), P10020.

[42] J.-C. Walter, M. Baiesi, G. T. Barkema, and E. Carlon. "Unwinding relaxation dynamics of polymers". *Phys. Rev. Lett.* **110** (2013), p. 068301.

[43] B. P. Belotserkovskii. "Relationships between the winding angle, the characteristic radius, and the torque for a long polymer chain wound around a cylinder: Implications for RNA winding around DNA during transcription". *Phys. Rev. E* **89** (2014), p. 022709.

[44] J.-C. Walter, M. Baiesi, E. Carlon, and H. Schiessel. "Unwinding dynamics of a helically wrapped polymer". *Macromolecules* **47** (2014), p. 4840.

[45] B. Duplantier and H. Saleur. "Winding-angle distributions of two-dimensional self-avoiding walks from conformal invariance". *Phys. Rev. Lett.* **60** (1988), p. 2343.

[46] Y. Hammer and Y. Kantor. "Ideal polymers near scale-free surfaces". *Phys. Rev. E* **89** (2014), p. 022601.

[47] F. W. Wiegel. *Introduction to path-integral methods in physics and Polymer Science*. Singapore: World Scientific, 1986.

[48] P. M. Morse and H. Feshbach. *Methods of theoretical physics*. Vol. 1. New York: McGraw-Hill, 1953.

[49] P. H. Moon and D. E. Spencer. *Field theory handbook*. Berlin: Springer, 1971.

[50] I. Chavel. *Eigenvalues in Riemannian geometry*. Vol. 115. Waltham, Massachusetts: Academic press, 1984.

[51] E. Ben-Naim and P. L. Krapivsky. "Kinetics of first passage in a cone". *J. Phys. A Math. Theor.* **43** (2010), p. 495007.

[52] J. Boersma and J. K. M. Jansen. *Electromagnetic field singularities at the tip of an elliptic cone*. Eindhoven University of Technology, 1990.

[53] N. Alfasi and Y. Kantor. "Diffusion in the presence of scale-free absorbing boundaries". *Phys. Rev. E* **91** (2015), p. 042126.

[54] T. Bickel, C. Jeppesen, and C. M. Marques. "Local entropic effects of polymers grafted to soft interfaces". *Eur. Phys. J. E* **4** (2001), p. 33.

[55] I. Jensen, W. G. Dantas, C. M. Marques, and J. F. Stilck. "Pressure exerted by a grafted polymer on the limiting line of a semi-infinite square lattice". *J. Phys. A Math. Theor.* **46** (2013), p. 115004.

[56] S. Chandrasekhar. "Stochastic problems in physics and astronomy". *Rev. Mod. Phys.* **15** (1943), p. 1.

[57] A. Y. Grosberg. "On pressure distribution over the surface of non-spherical globule". *Proc. Moscow State Univ., Physics Series* **1** (1972), p. 14.

[58] J. L. Doob. *Classical Potential Theory and its Probabilistic Counterpart*. Vol. 262. Berlin: Springer, 2001.

[59] J. D. Jackson. *Classical Electrodynamics*. Hoboken, New Jersey: Wiley, 3rd ed., 1998.

[60] A. Hanke, M. Krech, F. Schlesener, and S. Dietrich. "Critical adsorption near edges". *Phys. Rev. E* **60** (1999), p. 5163.

[61] Y. Hammer and Y. Kantor. "Entropic pressure in lattice models for polymers". *J. Chem. Phys.* **141** (2014), p. 204905.

[62] E. J. Janse van Rensburg. "Monte Carlo methods for the self-avoiding walk". *J. Phys. A Math. Theor.* **42** (2009), p. 323001.

[63] Morton E. Gurtin. *An introduction to continuum mechanics*. London: Academic Press, 1981.

[64] R. K. Pathria. *Statistical mechanics*. 2nd ed. Oxford: Butterworth-Heinmann, 1996.

[65] H. Heinz, W. Paul, and K. Binder. "Calculation of local pressure tensors in systems with many-body interactions". *Phys. Rev. E* **72** (2005), p. 066704.

[66] T. W. Lion and R. J. Allen. "Computing the local pressure in molecular dynamics simulations". *J. Phys.: Condens. Matter* **24** (2012), p. 284133.

[67] M. Doi and S. F. Edwards. *The theory of polymer dynamics*. Oxford: Clarendon Press, 1986.

[68] E. Eisenriegler. *Polymers near surfaces*. Singapore: World Scientific, 1993.

[69] K. Binder and M. Müller. "Polymer Models on the Lattice". *Simulation Models for Polymers*. Ed. by M. K. Telyanskii and D. N. Theodorou. New York: Marcel Dekker, 2004. Chap. 4.1, p. 125.

[70] R. Dickman. "New simulation method for the equation of state of lattice chains". *J. Chem. Phys.* **87** (1987), p. 2246.

[71] E. J. J. van Rensburg and T. Prellberg. "The pressure exerted by adsorbing directed lattice paths and staircase polygons". *J. Phys. A Math. Theor.* **46** (2013), p. 115202.

[72] F. Gassoumov and E. J. Janse van Rensburg. "The entropic pressure of a lattice polygon". *J. Stat. Mech. Theory Exp.* **2013** (2013), P10005.

[73] R. M. Brum and J. F. Stilck. "Pressure exerted by a grafted polymer: Bethe lattice solution". *J. Phys. A Math. Theor.* **48** (2015), p. 035002.

[74] Y. Wang, F. Y. Hansen, G. H. Peters, and O. Hassager. "Proof of the identity between the depletion layer thickness and half the average span for an arbitrary polymer chain." *J. Chem. Phys.* **129** (2008), p. 074904.

[75] Y. Wang, G. H. Peters, F. Y. Hansen, and O. Hassager. "Equilibrium partitioning of macromolecules in confining geometries: improved universality with a new molecular size parameter." *J. Chem. Phys.* **128** (2008), p. 124904.

[76] J. Cardy. *Scaling and Renormalization in Statistical Physics*. Cambridge University Press, 1996.

[77] J. L. Cardy and S. Redner. "Conformal invariance and self-avoiding walks in restricted geometries". *J. Phys. A. Math. Gen.* **17** (1984), p. L933.

[78] A. Milchev and K. Binder. "A polymer chain trapped between two parallel repulsive walls: A Monte-Carlo test of scaling behavior". *Eur. Phys. J. B* **3** (1998), p. 477.

[79] H.-P. Hsu and P. Grassberger. "Polymers confined between two parallel plane walls." *J. Chem. Phys.* **120** (2004), p. 2034.

[80] I. Teraoka, P. Cifra, and Y. Wang. "Polymer chains in good solvent facing impenetrable walls: what is the distance to the wall in lattice Monte Carlo simulations". *Colloids Surfaces A Physicochem. Eng. Asp.* **206** (2002), p. 299.

[81] D. I. Dimitrov, A. Milchev, K. Binder, L. I. Klushin, and A. M. Skvortsov. "Universal properties of a single polymer chain in slit: Scaling versus molecular dynamics simulations." *J. Chem. Phys.* **128** (2008), p. 234902.

[82] I. S. Gradshteyn and I. M. Ryzhik. *Table of integrals, series and products*. London: Academic Press, 2000.

[83] Y. Hammer and Y. Kantor. "Long polymers near wedges and cones". *Phys. Rev. E* **92** (2015), p. 062602.

[84] M. Lal. "Monte Carlo computer simulation of chain molecules. I". *Mol. Phys.* **17** (1969), p. 57.

[85] N. Madras and A. D. Sokal. "The pivot algorithm: A highly efficient Monte Carlo method for the self-avoiding walk". *J. Stat. Phys.* **50** (1988), p. 109.

[86] T. Kennedy. "A faster implementation of the pivot algorithm for self-avoiding walks". *J. Stat. Phys.* **106** (2002), p. 407.

[87] T. H. Cormen, C. E. Leiserson, R. L. Rivest, and C. Stein. *Introduction to algorithms*. 3rd. Cambridge: The MIT Press, 2009.

[88] N. Clisby, A. R. Conway, and A. J. Guttmann. "Three-dimensional terminally attached self-avoiding walks and bridges". *J. Phys. A Math. Theor.* **49** (2016), p. 015004.

[89] C. J. Geyer. "Introduction to Markov chain Monte Carlo". *Handbook of Markov chain Monte Carlo*. Ed. by S. Brooks, A. Gelman, G. L. Jones, and X.-L. Meng. Boca Raton: CRC Press, 2011, p. 1.

[90] N. Clisby. "Calculation of the connective constant for self-avoiding walks via the pivot algorithm". *J. Phys. A Math. Theor.* **46** (2013), p. 245001.

[91] S. Caracciolo, M. S. Causo, and A. Pelissetto. "Universality of subleading corrections for self-avoiding walks in the presence of one-dimensional defects". *J. Phys. A Math. Gen.* **30** (1997), p. 4939.

[92] S. Caracciolo, G. Ferraro, and A. Pelissetto. "Criticality of self-avoiding walks with an excluded infinite needle". *J. Phys. A Math. Gen.* **24** (1991), p. 3625.

[93] D Considine and S Redner. "Repulsion of random and self-avoiding walks from excluded points and lines". *J. Phys. A Math. Gen.* **22** (1989), p. 1621.

[94] J. F. Douglas and M. K. Kosmas. "Flexible polymer with excluded volume at an interacting penetrable surface of variable dimension: a multiple-.epsilon. perturbation theory". *Macromolecules* **22** (1989), p. 2412.

[95] C. Domb, J. Gillis, and G. Wilmers. "On the shape and configuration of polymer molecules". *Proc. Phys. Soc.* **85** (1965), p. 625.

[96] C. Domb, J. Gillis, and G. Wilmers. "On the shape and configuration of polymer molecules". *Proc. Phys. Soc.* **86** (1965), p. 426.

[97] D. S. McKenzie and M. A. Moore. "Shape of self-avoiding walk or polymer chain". *J. Phys. A Gen. Phys.* **4** (1971), p. L82.

[98] D. S. McKenzie. "The end-to-end length distribution of self-avoiding walks". *J. Phys. A Math. Nucl. Gen.* **6** (1973), p. 338.

[99] J. des Cloizeaux. "Lagrangian theory for a self-avoiding random chain". *Phys. Rev. A* **10** (1974), p. 1665.

[100] J. Dayantis and J.-F. Palierne. "Monte Carlo precise determination of the end-to-end distribution function of self-avoiding walks on the simple-cubic lattice". *J. Chem. Phys.* **95** (1991), p. 6088.

[101] R. Everaers, I. S. Graham, and M. J. Zuckermann. "End-to-end distance distributions and asymptotic behaviour of self-avoiding walks in two and three dimensions". *J. Phys. A. Math. Gen.* **28** (1995), p. 1271.

[102] S. Caracciolo, M. S. Causo, and A. Pelissetto. "End-to-end distribution function for dilute polymers". *J. Chem. Phys.* **112** (2000), p. 7693.

[103] M. Lax. "A direct enumeration study of self-avoiding walks terminally attached to a surface". *Macromolecules* **7** (1974), p. 660.

[104] A. T. Clark and M. Lal. "Effect of surface coverage on the configurational properties of adsorbed chains". *J. Chem. Soc. Faraday Trans. 2* **74** (1978), p. 1857.

[105] K. F. Freed. "Excluded volume effects in polymers attached to surfaces: Chain conformational renormalization group". *J. Chem. Phys.* **79** (1983), p. 3121.

[106] A. M. Nemirovsky and K. F. Freed. "Excluded volume effects for polymers in presence of interacting surfaces: Chain conformation renormalization group". *J. Chem. Phys.* **83** (1985), p. 4166.

[107] J. F. Douglas, A. M. Nemirovsky, and K. F. Freed. "Polymer-polymer and polymer-surface excluded volume effects in flexible polymers attached to an interface: comparison of renormalization group calculations with Monte Carlo and direct enumeration data". *Macromolecules* **19** (1986), p. 2041.

[108] J. F. Douglas, S. Q. Wang, and K. F. Freed. "Flexible polymers with excluded volume at a penetrable interacting surface". *Macromolecules* **20** (1987), p. 543.

[109] M. Daoud and J. P. Cotton. "Star shaped polymers : a model for the conformation and its concentration dependence". *J. Phys.* **43** (1982), p. 531.

[110] P. G. de Gennes. "Polymers at an interface; a simplified view". *Adv. Colloid Interface Sci.* **27** (1987), p. 189.

[111] Y. Hammer and Y. Kantor. "Winding angles of long lattice walks". *J. Chem. Phys.* **145** (2016), p. 014906.

[112] K. Rechendorff, G. Witz, J. Adamcik, and G. Dietler. "Persistence length and scaling properties of single-stranded DNA adsorbed on modified graphite". *J. Chem. Phys.* **131** (2009), p. 095103.

[113] H. S. Carslaw and J. C. Jaeger. *Conduction of heat in solids.* Oxford University Press, 2nd ed., 1959.